Georgia Institute of Technology

Daniel Guggenheim
School of Aerospace Engineering

CCL Report CCL-TR-2013-12-2

Dynamic Modeling of Plasma Effects during Multi-phase Detonations near a Surface and/or in a Magnetic Field

J. Schulz and S. Menon

Computational Combustion Laboratory
School of Aerospace Engineering
Georgia Institute of Technology
270 Ferst Drive
Atlanta, Georgia 30332-0150
http://www.ccl.gatech.edu

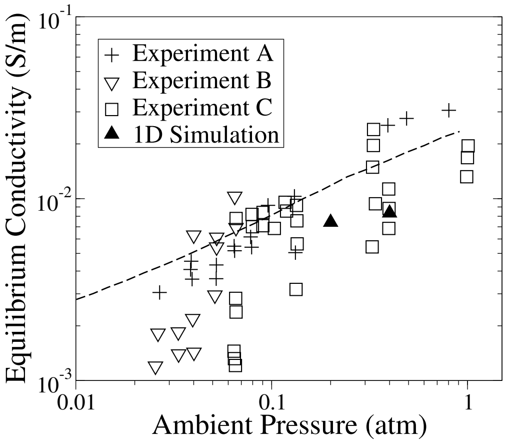

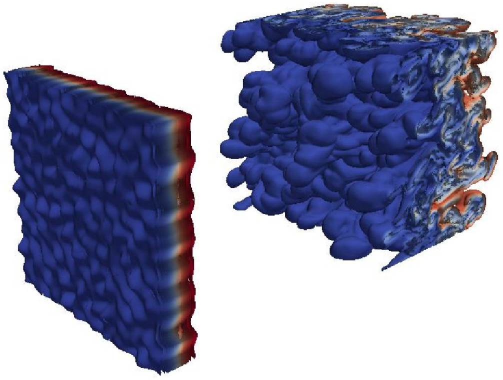

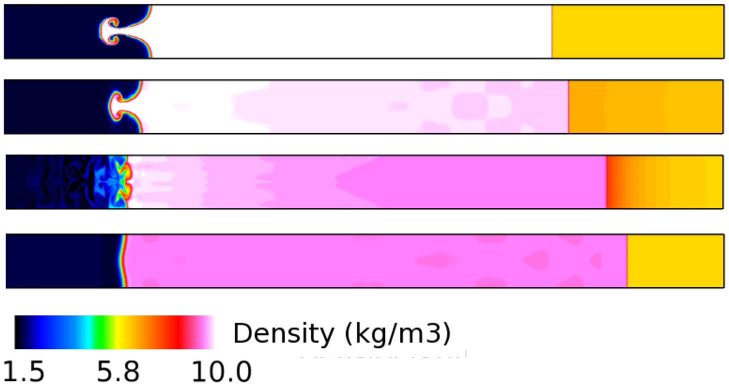

Sponsored by: *Defense Threat Reduction Agency*
Contract Number: *HDTRA1-09-1-0028*
Date: *December 31, 2013*

TABLE OF CONTENTS

LIST OF TABLES **iii**

LIST OF FIGURES **iv**

SUMMARY **vii**

I INTRODUCTION **1**

II ACCOMPLSHMENTS **4**

2.1 Technical Objectives 4

2.2 Accomplishments 4

III FORMULATION **6**

3.1 MHD Equations 6

3.1.1 Electrical Conductivity 9

3.1.2 Reaction and Ionization Mechanisms 10

3.1.3 Dispersed Phase 11

3.2 MHD Equations for Large-eddy Simulation 12

3.2.1 Turbulent closure model 14

3.3 Quasi-linear and Quasi-static MHD Equations 16

IV COMPUTATIONAL METHODS **19**

4.1 Numerical Integration 19

4.1.1 The $\nabla \cdot \mathbf{B} = 0$ constraint 20

4.1.2 Finite Volume Formulation 20

4.1.3 Flux Computation 21

4.2 Numerical Verification 22

4.2.1 One-dimensional Shock Tube 22

4.2.2 Orszag-Tang Vortex 23

4.2.3 Hartmann Channel 24

V ACCOMPLISHMENTS AND NEW FINDINGS 26

5.1 Gaseous Detonation 26

5.1.1 One-Dimensional Detonation 26

5.1.2 Potassium seeding in two-dimensional detonation simulations 30

5.1.3 Conclusions 32

5.2 Condensed-Phase Explosion 33

5.3 MHD Detonation 35

5.3.1 Effect of $B_{y,0}$ 38

5.3.2 Effect of $B_{x,0}$ 39

5.3.3 Conclusions 41

5.4 Richtmyer-Meshkov Instability 41

5.4.1 Verification and Validation 43

5.4.2 RMI in Dispersed Phase Flows 49

5.4.3 RMI in Conducting Flows 56

VI CONCLUSIONS 60

VII SIGNIFICANCE AND RELEVANCE TO THE DTRA MISSION 62

7.1 Personnel Supported 62

7.2 Publications 62

7.3 Related Publications 63

7.4 Interactions/Transitions 63

7.5 New Discoveries 63

7.6 Honors/Awards 63

VIII APPENDIX 64

8.1 Published Papers 75

LIST OF TABLES

5.1 A summary of parameter set for the simulations used in this study. To compute the non-dimensional parameters the following reference values were used: L=6 mm, $u = 1900$ m/s, ρ_0=0.17 kg/m^3 where L is the transverse channel dimension, $u \approx D$, and ρ is the ambient density. The MHD cases are distinguished by a X indicating the magnetic field is in the direction of the detonation propagation (x-direction), and a Y indicating the magnetic field is perpendicular to the direction of the detonation propagation (y-direction). These cases are compared against the hydrodynamic simulations of case NF (No-Field). 36

5.2 Test conditions and measurements of the re-shocked RMI experiments of Vetter and Sturtevant[1] where VS0-VI and VS0-VII correspond to experiments VI^b and VII^b. 44

5.3 Summary of the simulation configurations used in the re-shock validation experiment (VS) and the multi-mode (MM) and single-mode (SM) numerical simulations. The function $\mathcal{U}_r$ represents a uniform random variable chosen on the interval [0,1], $k_0 = 2\pi/L_y$, and Δx is the grid resolution used for each case. All dimensional values are given in units of centimeters. 46

5.4 Summary of the multi-phase initial conditions used in the numerical simulations. Simulations are referred to by the case name (i.e., SM, MM, etc.) defined in Table 5.3 and the case number defined below. For reference, this table additionally provides the RMI growth-rate data for the SM cases. . . . 48

8.1 Summary of the hydrogen-air combustion mechanism used in the present detonation simulations. For the three-body reactions, M includes H_2, O_2, H, O, OH, HO_2, H_2O_2, H_2O and N_2 where the collision efficiency is unity with the exceptions: M_a does not include O_2, H_2O, or N_2, and the collision efficiencies for H_2 and H_2O in M_b are 2.4 and 6.0, in M_c are 1.7 and 7.0, in M_d are 2.4 and 15.4, and in M_e are 0.73 and 3.65, respectively. For reactions $r11$ and $r14$, $k = k_a + k_b$, and for reaction $r12$, $k = k_{\text{inf}}[P_r/(1+P_r)]F$ with $P_r = k_0[\text{M}]/k_{\text{inf}}$ and F as defined in [2]. 65

8.2 Arrhenius rate coefficients for the dissociation reactions. All collision efficiencies are unity. M_f includes N_2, O_2, H_2, NO, OH, H_2O_2, HO_2, H_2O and all ions, and M_g includes N, O, H. In order not to repeat reactions included in the combustion chemistry, M_h only includes NO and all ions, and M_i includes NO, N and all ions. 66

LIST OF FIGURES

3.1 The equilibrium electrical conductivity is shown as a function of pressure and temperature for a stoichiometric H_2-air mixture. Seeding by potassium drastically increases the electrical conductivity. 10

3.2 Comparison of the numerically computed detonation velocity for a H_2-air mixture at an ambient pressure and temperature of 0.2 bar and 298 K, respectively. The results are compared to theoretical computations of the detonation velocity obtained from NASA's CEA code. 11

4.1 (a) Density and (b) magnetic field profiles at t=0.2 seconds for the Dai-Woodward MHD test case [3] for first and second order upwind scheme using the HLLD Riemann solver. 23

4.2 (a) Density and (b) magnetic field profiles at t=0.1 seconds for the Ryu-Jones MHD test case [4] for the second order upwind scheme using the HLLD Riemann solver. 23

4.3 Normalized temperature contours for the Orszag-Tang vortex problem at t=π seconds. 24

4.4 Normalized velocity profiles for laminar Hartman flow. Here, H_0 and U_0 denote the half-channel height and velocity averaged in the transverse direction, respectively. The lines indicate the analytical solution for the different Hartman numbers. 25

5.1 (a) One-dimensional profiles of temperature and species mass fraction directly behind the detonation-sustained shock wave. The results are shown for a stoichiometric H_2-air detonation in an ambient pressure and temperature of 0.2 bar and 298 K, respectively. 27

5.2 (a) One-dimensional profiles of pressure shown at two instances in time as the detonation propagates through the domain. The peak pressures oscillate indicating the detonation is in the oscillatory regime [5]. Both results are shown for a stoichiometric H_2-air detonation in an ambient pressure and temperature of 0.2 bar and 298 K, respectively. (b) One-dimensional profiles the species number density showing the important role of NO formation in the ionization process. 28

5.3 (a) One-dimensional profiles of the electrical conductivity computed for a stoichiometric H_2/O_2 mixture with 0.667% N_2 dilution at three different ambient pressures. (b) A comparison of the electrical conductivity at different N_2 dilutions. The peak post-detonation temperature for 0.667%, 30%, 50%, and 79% N_2 dilution is 3408, 3265, 3180, 2751 K respectively. 28

5.4 (a) A comparison of the electrical conductivity at different potassium seeding percentages. The reference case for detonation of a stoichiometric H_2-air mixture at ambient pressure and temperature of 0.2 bar and 298 K is shown for comparison. (b) At seeding percentages higher than 0.06%K the detonation wave decays into a propagating shock wave. 29

5.5 Contours of the $\ln(|\bigtriangledown\rho|+1)$ and of the mass fraction of H_2O_2 (in white) delineate the prominent features of gaseous detonations. The grid resolution is varied from (a) 5μm, (b) 10μm and (c) 20μm to determine the minimum grid resolution required. 30

5.6 Stoichiometric H_2-air detonation at an ambient temperature and pressure of 298 K and 0.2 atm. (a) Contours of temperature, and (b) the electrical conductivity. The length scale shown is in millimeters. 31

5.7 Stoichiometric H_2-air detonation at an ambient temperature and pressure of 298 K and 0.2 atm seeded with 1% K by weight. (a) Contours of temperature, and (b) the electrical conductivity. The length scale shown is in millimeters . 32

5.8 (a) Planar averaged mass fractions of the species involved in potassium ionization behind the detonation front with 1% K seeding. (b) Planar averaged profiles of the electrical conductivity for various potassium seeding percentages. 33

5.9 A time-history of the electrical conductivity for a condensed-phase explosion of a nitromethane change uniformly loaded with aluminum particles. The contributes do to gaseous ionization and particles are indicated on the plot. . 34

5.10 The averaged temperature profiles for case Y4 at different times: $t_{-1} = 0.104$ ms, $t_0 = 0.113$ ms, $t_1 = 0.127$ ms, $t_2 = 0.149$ ms and $t_3 = 0.157$ ms. 37

5.11 The profiles of mass fraction of HO_2 taken at the transverse location corresponding to the center of Mach stem for case Y4 at different times: $t_0 = 0.113$ ms, $t_1 = 0.127$ ms, $t_2 = 0.149$ ms and $t_3 = 0.157$ ms. 38

5.12 Plot of $\ln(|\nabla\rho|+1)$ for case Y4 showing the structure of the detonation front at $t_0 = 0.113$ ms, $t_2 = 0.149$ ms and $t_3 = 0.157$ ms. 38

5.13 The average location of the detonation front as a function of time for the cases given in Table 5.1 39

5.14 Profiles of the HO_2 mass fraction and temperature for cases NF, X2, X4, and X5 corresponding to the center of the Mach stem for each detonation front at approximately 0.175 ms. 40

5.15 Plot of $\ln(|\nabla\rho|+1)$ for cases NF, X2, X4, and X5 (top to bottom) shown in Table 5.1 showing the detonation front and the post-detonation flow structures at $t = 0.175$ ms. 42

5.16 Schematic of the simulation domain where M_s is the Mach number of the shock, L_x is the distance from the end wall to the contact, and L_s is the distance from the contact to the initial shock position. For the multi-phase simulations, L_p is the length of the initial particle cloud. 44

5.17 Mixing zone before (left) and after (right) re-shock for Case RMI1. 45

5.18 (a) Evolution of the mixing layer $\eta(t)$ at three different grid resolutions ($\Delta x_0 =$ 0.21 cm, $\Delta x_1 = 0.105$ cm, $\Delta x_2 = 0.07$ cm) with comparison to the experimental measurements summarized in Table 5.2. (b) Time history of the normalized mixing length in single-mode RMI at the same grid resolutions (Δx_1, Δx_2) with a comparison to the non-linear theory of Sadot *et al.* [6]. 47

5.19 Time evolution of (a) the mixing layer width, $\eta(t)$, and (b) the mixing fraction, $\Theta(t)$, for the multi-mode RMI in a dilute gas-particle mixture compared to the single-phase results of VS0-VI and MM0. 49

5.20 Contours of the species mass fraction, $Y_{SF_6} = Y_{Air} = 0.5$ for the single-phase cases SM0 and MM0 compared to representative multi-phase cases SM14 and MM14 colored by the velocity in the x-direction. 51

5.21 (a) Time evolution of the ratio of the particle cloud volume fraction, α, to the initial volume fraction, α_0. (b) x-t diagram of the time history of the shock location, x_s, the left interface of the particle cloud, x_p, and the left (spike) and right (bubble) interfaces of the mixing zone, $x_{\eta,L}$ and $x_{\eta,R}$, respectively. . 52

5.22 (a) Evolution of the mixing layer width, $\eta(t)$, at different α_0 and St. (b) The vorticity transport budget during the initial growth of the RMI for cases with the same r_p where $|\Pi_k(t)|$ and $|\beta_k(t)|$ are the magnitude of the vorticity production due to the particle acceleration term and the baroclinic torque volume-averaged over the mixing zone. 53

5.23 Time evolution of the mixing-layer growth, $\eta(t)$, after re-shock (b) Relationship between the velocity jump, ΔV_r, at re-shock and the re-shocked RMI growth-rate, $\dot{\eta}$, compared to the model given by Eq. 5.12. 55

5.24 Contours of the species mass fraction at $Y_{SF_6} = Y_{Air} = 0.5$ and particle locations colored by the magnitude of the particle velocity for case SM0 (top left), SM5 (bottom left), SM9 (top right) and SM14 (bottom right). 56

5.25 Density contours of RM instability for different values of the electrical conductivity. The electrical conductivity increases from top to bottom starting at zero. 59

5.26 The growth-rate of the RM instability before the tearing instability is initiated. 59

SUMMARY

A multi-physics model has been developed to simulate detonations and condensed-phase explosions in the presence of an external electromagnetic field. To simulate these effects, models for high-temperature gas physics, plasma-production, dispersed-phase mixing, and turbulence have been implemented within the framework of a numerical method capable of simulating magnetohydrodynamic (MHD) flows. This research has leveraged past work in MHD flows, detonations, and turbulence-chemistry interactions to study multi-scale detonation-plasma-field interactions, and has furthered the understanding of many key physical processes of these flows. This work targeted three main basic science objectives: the study of plasma-production by detonations and condensed-phase explosions, the study of MHD instabilities and turbulence relevant to post-detonation flows, and the study of how a detonation is affected by the presence of a magnetic field. Simulations indicate that gaseous detonation waves generate a weakly ionized plasma in the post-detonation region. The average electrical conductivity in the post-detonation flow, however, is of the order of 10^{-3} S/m, and practical engineering applications involving the use of MHD forces to manipulate the flow for generation of electrical power, propulsive thrust, etc., require higher levels of electrical conductivity. Simulations of mixtures seeded with particles of a low ionization potential show a substantial increase the flow's electrical conductivity. The presence of these particles can adversely affect the detonation propagation. The physics of how an electromagnetic field interacts with the conducting products of a detonation, and how that interaction might affect the stability and propagation of the detonation wave is systematically studied. The magnetic field applied in the direction of detonation propagation affects the detonation through a combined effect of Joule heating and Lorentz force, in some cases altering the cellular structure of the detonation completely by reducing the half-reaction zone thickness. Basic studies of the Richtmyer-Meshkov instability, an important mechanism for the transition to turbulence in explosions, are used to elucidate several salient features of these types of MHD flows. Namely, simulations show that the presence of a dispersed phase alters the mixing growth-rates of the instability, and furthermore, an applied magnetic field is shown to either suppress or enhance fluid mixing.

CHAPTER I

INTRODUCTION

Magnetohydrodynamics (MHD) is the study of electrically conducting fluids. A salient feature of MHD is the generation of induced currents by the relative motion of the conductive fluid against a magnetic field misaligned with the fluid velocity. These induced currents introduce a new and complex dynamic to the flow. Typically, the conductive fluid in question is an ionized gas or plasma, but the study of MHD is equally applicable to the liquid metal flows in a fast-breeder nuclear reactor or in the metallurgical mixing of molten steel; two of the few examples where electrically conducting fluids exist in terrestrial applications. There are other examples as well, such as the confined plasma of fusion reactor, or the plasma produced by inertial confinement fusion, or the propulsive flow of a magnetoplasmadynamic (MPD) thruster. In fact, since the late 1960's, there have been many engineering attempts to leverage the conductivity of a fluid for the generation of electrical power, propulsive thrust, drag reduction, etc. These conductive fluids, however, exist only under certain imposed conditions, which are often difficult to maintain in a laboratory or in some cases fall outside the traditional scope of MHD. As a result, the dynamics of these plasmas are often highly dependent upon the mechanisms generating the ionized gas. In contrast, it is said that 99% of all extraterrestrial matter is in the plasma state, making the governing equations of MHD de facto in the study of solar dynamics, star formation, supernovae explosions, and other astrophysical phenomenon. Yet, in both extraterrestrial and terrestrial applications, the plasma dynamics (and more exclusively those described by MHD), are not always the driving forces of the physical phenomenon. In astrophysics, gravitational forces can be extremely large, and in terrestrial applications, the electrical conductivity of the fluid is often so small the electromagnetic dynamics are linear and purely dissipative. Conversely, the generation of the Sun's magnetic field or the instabilities arising in a fusion reactor are governed by the complex, non-linear interaction of the magnetic field with the fluid. A quick survey of MHD underlies a single important fact in the study of electrically conducting fluids–the physical processes manifest dynamics occurring over an extremely large range of spatial and temporal scales. This complexity makes the study of MHD difficult, in terms of both numerical modeling and interpreting experimental data.

Experimental observation of turbulent MHD flows is further limited by the practical difficulties in obtaining measurements of realistic systems. Astrophysical measurements are often too complex to be to useful [7], and only within the last ten years has it been possible to experimentally observe turbulent dynamos in a laboratory, most notably in the recent on-going von Kármán sodium experiments [8]. Moreover, conducting liquids available in the laboratory are either corrosive, opaque, or very hot making them difficult to handle and control [9]. The general dearth of observational data has stressed the need for accurate theoretical and numerical models. Early studies of MHD focused on two main problems, magnetic confinement and solar dynamics. These efforts developed a deep understanding of magnetic instabilities and the turbulent dynamo problem, the later cumulating in the development of mean-field electrodynamics. Recent advances in numerical simulations of MHD, however, have introduced a wide variety of new questions and extended the scope of MHD. This study focuses on the importance of compressibility and finite electrical resistivity in turbulent MHD flows. Only recently within the last few years has the influence of compressibility been investigated in MHD flows, and the role of resistivity in plasmas is now viewed as critical parameter in the catastrophic events resulting from magnetic reconnection. One of the primary objectives of this work is the development and validation of a MHD numerical model capable of simulating compressible, resistive, multi-species ionized gases.

In regards to engineering (terrestrial) applications in MHD, two general research questions are identified–first, how is the ionized gas produced and sustained? And second, given this plasma, what are dynamics of the flow over the range of scales of interest? The goal of the current work is to answer these questions in regards to the production of plasma by detonations and explosions in multi-phase mediums. The first question is more straight-forward to answer than the second. Several experiments have measured the electrical conductivity in both condensed-phase explosions and gaseous detonations. While in condensed-phase explosions the ionization process is less clear, the high temperature environment produced by both gaseous detonations and condensed-phase explosions is the primary contributing factor. Experiments and numerical studies indicate that the inclusion of low-ionization particles, e.g., potassium carbonate, or metal additives such as aluminum, are required in order to increase the electrical conductivity to high enough values for the electromagnetic forces to be substantial enough for practical engineering use. This fact introduces additionally complexity, since it means the electrically conducting medium of such devices is now possibly a multi-phase flow. Regardless, measurements indicate that the plasma production can be substantial. It is should be mentioned now that it is important to distinguish between the study of plasma, for which MHD is relevant, and the study of flows where substantial charge non-equilibrium can occur such as in gas discharges and some electric propulsion devices. While these topics are important in a wide variety of engineering applications, such as plasma-assisted combustion or shock-to-detonation enhancement by strong electromagnetic fields [10], these problems can not be analyzed within the framework of MHD. From this perspective, more attention is spent on assuring that a plasma is indeed produced by detonation and explosion, and then determining how such a plasma may be used or influenced by a magnetic field.

What effect, if any, an electromagnetic field might have on the propagation of either a gaseous or heterogenous detonation is still an open question. Experimental observation is both conflicting and inconclusive. Recent experiments investigating the effects of an applied electric or magnetic field on a heterogenous detonation show only modest effects when an electric field is applied and no effects when a magnetic field is applied [11]. This is in contrast to older observations by Cook et al. [12, 13, 14] who have observed significant magnetic field effects. Currently, no numerical simulations are available in the published literature. This is largely because such full-scale simulations are expensive or in many ways not yet possible. Even in this work, the problem is simplified to the study of three separate problems in order to make the understanding of the physics more tractable. First, the plasma-production processes in gaseous detonations and condensed-phase explosions is investigated. This study focuses primarily on seeded hydrogen-air gaseous detonations. A finite-rate detailed kinetic mechanism (26 species and 65 reactions) for the combustion and ionization of H_2-air mixtures with and without potassium seeding is employed and validated through comparison to theory. The effects of ambient pressure, N_2 dilution, and potassium seeding on the electrical conductivity of the flow are investigated. These results reveal trends similar to those observed in the experimental work discussed previously but also suggest new physics that may limit the electrical conductivity from what is attainable theoretically. Such simulations are important in addressing the potential for the proposal of MHD applications for post-detonation flows.

Second, a detailed study of the mixing and instability dynamics occurring in the post-detonation flow is conducted. The Richtmyer-Meshkov (RMI) and Rayliegh-Taylor (RTI) instabilities are important mechanisms in both blast waves and detonation since they trigger the transition to fully-developed turbulence, which is important in after-burn. In conducting flows, a magnetic field has been shown to impact the dynamics significantly and in some cases stabilize the fluid entirely. Moreover, since many engineering conducting flows contain a dispersed phase, the effects of particles on mixing is also investigated. Furthermore, additional tearing instabilities as a result of magnetic reconnection could be initiated depending on the electrical conductivity of the gas. Such events could drastically alter the dynamics of flow.

Lastly, to investigate the effect of a magnetic field on the propagation of a detonation, numerical simulations are conducted for a range of non-dimensional MHD parameters. This study relies on the previous numerical simulations of stoichiometric hydrogen-air detonations for estimates of the electrical conductivity in the post-detonation flow. As such, a finite-rate kinetic mechanism for the ionization processes is not included in the numerical simulation, and the electrical conductivity is simply assumed to be spatially uniform and constant. The external field is applied in either perpendicular or parallel to the direction of the propagation of the detonation. Results, both in two- and three-dimensions, show that the post-detonation flow features become highly anisotropic and the strength of the transverse waves is weakened resulting in a transformation in the structure of detonation front. After some time, the propagation of the detonation is adversely affected. Flow parameters, along with the reaction zone widths, are analyzed to quantify the effect of the applied field on the detonation.

While the intended application of this work is the study of high-energy explosions (the plasma generation process and its subsequent interaction with a magnetic field), the fundamental physical processes involved are applicable to wide variety of problems. The investigation of these topics has led the development of a multi-physics MHD solver capable of modeling multi-species, reacting, compressible, visco-resistive, turbulent flows. This tool has allowed the investigation of new areas of research relevant to both the engineering and scientific communities of MHD. The following report summarizes this work and the contributions made.

CHAPTER II

ACCOMPLSHMENTS

We summarize (for completeness) the original proposed objectives and then list the accomplishments made.

2.1 Technical Objectives

The five technical objectives were chosen to isolate the sub-features of the problem and to provide a step-by-step approach to an in-depth understanding of the various physical processes and scales of interactions. To achieve these objectives integration of independently developed physical models was required. As progress was made, it was discovered that some of the objectives required more fundamental research. Therefore as a part of understanding how a magnetic field affects detonation and explosion, a more detailed study of the magnetic field effects on fundamental fluid instabilities such as the Richtmyer-Meshkov instability was undertaken. Such fluid instabilities are important in after-burning as they play a key role in the transition to turbulence. To summarize, the overall technical objectives are:

1. Investigate the plasma production and quantify the electrical conductivity of gaseous detonations and condensed-phase explosions.
2. Fundamentally analyze how an external magnetic field affects turbulence and flow instabilities.
3. Investigate detonation/shock-plasma interaction with external magnetic field.
4. Study the interactions with surfaces and provide a scaling analysis of the plasma effects.
5. Critical evaluation and validation of the methodologies.

2.2 Accomplishments

The following research findings were accomplished during this funding. These findings were published in two peer-reviewed papers and two more have been submitted for review. See Section 7.2 for a list of these publications.

1. A multi-physics model capable of simulating MHD flows relevant to study of plasma-producing gaseous detonations and condensed-phase explosions was developed. The numerical model was validated and verified both quantitatively against several standard MHD test cases, theoretical predictions, and experimental measurements as well as qualitatively in the simulation of several canonical MHD flows.

2. The electrical conductivity was numerically computed in the post-detonation flow of a H_2-air mixture. The observed electrical conductivities in an unseeded detonation was found to be too low for MHD devices to be efficient. Thus seeding the mixture with low ionization potential alkali salts is necessary. While seeding does increase the electrical conductivity, simulations in both one and two dimensions show that the detonation is sensitive to the amount of seeding material injected into the flow. Too high of a seeding percentage adversely affects the detonation propagation.

3. A simple model for computing the electrical conductivity in dispersed-phase mixtures was proposed. More work, however, is necessary in validating this model to determine its applicability. A summary of the current efforts in this work is provided.

4. The Richtmyer-Meshkov instability, which drives the transition to turbulence in post-detonation flows, is studied in detail in dispersed-phase mixtures and in conducting flows under that application of a magnetic field. The presence of a dispersed-phase was shown to impact the mixing-rate dramatically underlining the impact any seeding particles may have on the basic physical processes. A magnetic field was shown to dramatically alter the behavior of the instability.

5. The MHD tearing instability was shown to occur during the development of the Richtmyer-Meshkov instability for certain magnetic diffusivities. This was not known until this research, and currently this is being investigated carefully for publication.

6. A magnetic field was shown to drastically alter the dynamics of a detonation in ways that were not previously known. This has important implications for detonations in the presence of strong magnetic fields, particularly when the applied field is normal to the detonation propagation.

CHAPTER III

FORMULATION

3.1 MHD Equations

The governing equations of MHD describe the dynamics of an electrically conducting fluid or plasma. Formally, a plasma is defined as a *quasi–neutral* gas of charged and neutral particles exhibiting *collective behavior* by means of long-range electromagnetic forces [15]. This definition constrains the study of MHD to the macroscopic phenomenon occurring at the spatial and temporal time scales larger than those intrinsic to the ionized gas, such as the Debye length or the Larmor radii of the charged particles [16]. A consequence of quasi-neutrality is the absence of charge separation, and thus over length scales considered, there can be no space charges. For the same reason, Maxwell's correction to include the effects of the charge displacement current is also negligible. Thus, the dynamics of the electromagnetic field are determined by the following pre-Maxwell equations,

$$\frac{\partial E_i}{\partial x_i} = 0, \tag{3.1}$$

$$\epsilon_{ijk}\frac{\partial E_k}{\partial x_j} = -\frac{\partial B_i}{\partial t}, \tag{3.2}$$

$$\epsilon_{ijk}\frac{\partial B_k}{\partial x_j} = \mu_0 J_i, \tag{3.3}$$

$$\frac{\partial B_i}{\partial x_i} = 0, \tag{3.4}$$

which describe the laws of Gauss, Faraday, and Ampere, as well as the requirement of no magnetic monopoles for a plasma. The current density vector, magnetic field vector, electric field vector are given by J_i, B_i, and E_i, respectively, and the symbol ϵ_{ijk} is the permutation operator, which is 0 when all indices are equal, +1 when the indices are in cyclic order, and −1 when the indices are in reverse cyclic order. The constant μ_0 is the permeability of free space. In addition to these equations, the governing equations for the flow can be derived using simple heuristic arguments about the balance of momentum and energy of a fluid element. In MHD, the electric and magnetic field exert a force on the conductive fluid, but since there can be no charge separation if quasi-neutrality is to be maintained, the electrostatic body force is negligible–the electric field merely maintains the current. Only a magnetic component of the Lorentz force contributes,

$$F_i = \epsilon_{ijk} J_j B_k. \tag{3.5}$$

Using Ampére's law, Eq. 3.3, the Lorentz force can be re-written as the divergence of a stress tensor,

$$F_i = \epsilon_{ijk} J_j B_k = -\frac{\partial T_{ij}}{\partial x_j}, \tag{3.6}$$

where the magnetic stress tensor, T_{ij}, is

$$T_{ij} = \left(\frac{B_i B_j}{\mu_0} - \frac{B_k B_k}{2\mu_0} \delta_{ij} \right) \tag{3.7}$$

The second term in T_{ij} acts as an isotropic pressure. The ratio of this term, referred to as the magnetic pressure, to the thermodynamic pressure, p, is an important parameter, which is often used to characterize the strength of the magnetic field.

$$\beta = \frac{p}{B_k B_k / 2\mu_0} = \frac{2\mu_0 p}{B^2} \tag{3.8}$$

There are two additional source terms in the total energy equation: a work term due to the Maxwell stress, $T_{ij} u_j$, and a source term resulting from the electrical power dissipation per unit volume, $J_i E_i$. Here u_i is the velocity vector, and E_i is the electric field in the laboratory frame of reference and is related to electric field vector in the moving frame of reference E_i' through a Galilean transformation,

$$E_i' = E_i + \epsilon_{ijk} u_j B_k. \tag{3.9}$$

The electric field E_i' is determined by Ohm's law, which states that $E_i' = J_i/\sigma$ with σ being the scalar electrical conductivity of the plasma. The electrical power dissipation term, $J_i E_i$, can be re-written using Faraday's law and Ampére's law in terms of B_i and J_i as

$$\begin{aligned} J_i E_i &= - \left[\frac{\partial}{\partial t} \left(\frac{B_i B_i}{2\mu_0} \right) + \frac{\partial}{\partial x_i} \left(\frac{\epsilon_{ijk} E_j' B_k}{\mu_0} \right) \right] && (3.10) \\ &= - \frac{\partial}{\partial t} \left(\frac{B_i B_i}{2\mu_0} \right) + \frac{\partial}{\partial x_i} \left(\eta \epsilon_{ijk} B_j J_k \right) && (3.11) \end{aligned}$$

where η is the magnetic diffusivity ($= 1/\mu_0 \sigma$). The term $B_i B_i / 2\mu_0$ is the magnetic energy, and thus, if the total energy, E, is defined as the sum of the internal energy, e, the specific kinetic energy $u_i u_i/2$, and the specific magnetic energy, $B_i B_i / 2\rho\mu_0$, the first term in above equation can be absorbed into the time rate of charge of the total energy, and the conservative form of the energy conservation equation is retained. The conservation equation for mass and species are not affected by the presence of the electromagnetic field.

While Eqs. 3.1-3.4 govern the dynamics of the electromagnetic field, these equations can be combined and simplified to obtain a single transport equation for the magnetic field. Starting from Faraday's law and substituting E_i using Ohm's law, the following equation is obtained,

$$\begin{aligned} \frac{\partial B_i}{\partial t} = - \epsilon_{ijk} \frac{\partial E_k}{\partial x_j} = - \epsilon_{ijk} \frac{\partial (J_k/\sigma - \epsilon_{klm} u_l B_m)}{\partial x_j} && (3.12) \\ \frac{\partial B_i}{\partial t} - \epsilon_{ijk} \frac{\partial \left(\epsilon_{klm} u_l B_m \right)}{\partial x_j} + \epsilon_{ijk} \frac{\partial \left(J_k/\sigma \right)}{\partial x_j} = 0. && (3.13) \end{aligned}$$

After some manipulation, the second term on the left-hand side of the above equation can be simplified, and Ampere's law can be used to replace the current density such that the magnetic induction equation is only a function of the electrical conductivity, the magnetic field vector, and the velocity vector. This equation is then simplified as

$$\frac{\partial B_i}{\partial t} + \frac{\partial}{\partial x_j}\Big(u_j B_i - u_i B_j\Big) + \epsilon_{ijk}\frac{\partial}{\partial x_j}\left(\eta\epsilon_{klm}\frac{\partial B_m}{\partial x_l}\right) = 0, \tag{3.14}$$

$$\frac{\partial B_i}{\partial t} + \frac{\partial}{\partial x_j}\left[u_j B_i - u_i B_j + \eta\left(\frac{\partial B_i}{\partial x_j} - \frac{\partial B_j}{\partial x_i}\right)\right] = 0. \tag{3.15}$$

In the above expressions, the magnetic resistivity is given by $\eta = 1/(\mu_0\sigma)$, and if η is constant, than the magnetic induction equation can be further simplified to the following expression

$$\frac{\partial B_i}{\partial t} + \frac{\partial}{\partial x_j}\Big(u_j B_i - u_i B_j\Big) + \eta\frac{\partial^2 B_i}{\partial x_j^2} = 0. \tag{3.16}$$

This equation expresses the mutual interaction between the magnetic field and the velocity field and is one of the most striking features of MHD. Simplistically, this dynamic and non-linear process can be arbitrarily divided into three parts [17]. First, according to Faraday's law of induction, an electromotive force (emf) is created as a result of the relative movement of a plasma within a magnetic field. The emf is of order $|\epsilon_{ijk}u_jB_k|$ and induces a current density, j_i, of order $\sigma|\epsilon_{ijk}u_jB_k|$ where σ again is the electrical conductivity of the plasma. Second, Ampére's law states that currents induce magnetic fields. The induced current caused by the emf therefore generates an induced magnetic field adding to the already existing imposed magnetic field. The net result is that the magnetic field lines seem to be dragged along by the plasma. Lastly, the total magnetic field couples with the induced current density resulting in a Lorentz force, $\epsilon_{ijk}J_jB_k$. The entire process tends to reduce the relative movement of the fluid and the field. This ability for the fluid to drag a magnetic field and for a magnetic field to pull a plasma results in a "freezing together" of the plasma and the magnetic field [17].

Combining all of the equations, the conservative form of the MHD equations for a compressible, multi-species, reacting flow are given by:

$$\frac{\partial \rho}{\partial t} + \frac{\partial \rho u_i}{\partial x_i} = 0, \tag{3.17}$$

$$\frac{\partial \rho u_i}{\partial t} + \frac{\partial}{\partial x_j}\Big(\rho u_i u_j + p\delta_{ij} - \tau_{ij} - T_{ij}\Big) = 0, \tag{3.18}$$

$$\frac{\partial \rho E}{\partial t} + \frac{\partial}{\partial x_i}\Big[\left(\rho E + p\right)u_i + q_i - u_j\tau_{ij} - u_jT_{ij} - \eta\epsilon_{ijk}B_jJ_k\Big] = 0, \tag{3.19}$$

$$\frac{\partial \rho Y_{(k)}}{\partial t} + \frac{\partial}{\partial x_i}\Big[\rho Y_{(k)}\left(u_i + V_{i,(k)}\right)\Big] = \dot{\omega}_{(k)}, \tag{3.20}$$

$$\frac{\partial B_i}{\partial t} + \frac{\partial}{\partial x_j}\left[u_j B_i - u_i B_j + \eta\left(\frac{\partial B_i}{\partial x_j} - \frac{\partial B_j}{\partial x_i}\right)\right] = 0, \tag{3.21}$$

$$\frac{\partial B_i}{\partial x_i} = 0, \tag{3.22}$$

In the above equations, ρ is the gas density, u_i is the velocity vector, E is the total specify energy, and $Y_{(k)}$ is the kth species mass fractions. The thermodynamic pressure, p, is computed using the perfect gas equation of state, $p = \rho RT$, where T is the temperature of the gas phase, and R is the mixture-averaged gas constant, and the current density, J_i, is computed from Ampere's law, Eq. 3.3. The viscous terms, τ_{ij}, q_i, and $V_{i,(k)}$, are the shear-stress tensor, the rate of heat transfer, and the kth species diffusion flux, respectively. They are given as

$$\tau_{ij} = \mu \left(\frac{\partial u_i}{\partial x_j} + \frac{\partial u_j}{\partial x_i} \right) + \delta_{ij} \lambda \frac{\partial u_m}{\partial x_m}, \tag{3.23}$$

$$q_i = -\kappa \frac{\partial T}{\partial x_i} + \rho \sum_{k=1}^{N_s} h_{(k)} Y_{(k)} V_{i,k}, \tag{3.24}$$

$$V_{i,(k)} = -\frac{D_{(k)}}{Y_{(k)}} \frac{W_{(k)}}{\overline{W}} \left(\frac{\partial X_{(k)}}{\partial x_i} \right), \tag{3.25}$$

where μ is the mixture-averaged viscosity, δ_{ij} is the Kronecker delta function, λ $(= -2/3\mu)$ is the bulk viscosity, κ is the mixture-averaged thermal conductivity of the gas phase, $\overline{W}$ is the mixture-average molecular weight, and $h_{(k)}$, $X_{(k)}$, and $D_{(k)}$ are respectively the specific enthalpy, the mole fraction, and the mixture-averaged diffusion coefficient of the k-th species. The transport properties for each species are computed using curve-fits as a function of the gas temperature [18, 19]. The net rate of change of the kth species, $\dot{\omega}_{(k)}$, is determined from a reduced set of reaction rates composing the particular chemical mechanism chosen. More information about the chemical mechanism used in ionizing gases is given later.

In MHD, it often assumed that the perfect gas equation of state, $p = \rho RT$, is still applicable and that the fluid is Newtonian. This assumption, however, is not strictly valid since a strong magnetic field can make the fluid behave anisotropic. In such a case, separate transport properties would be required for the directions perpendicular and parallel to the magnetic field making all the transport coefficients tensors and not scalars. Furthermore, Ohm's law is valid only under the assumption that the current density and the electric field are linearly related by the electrical conductivity. Thus, Ohm's law is akin to Fourier's law and Newton's law of viscosity meaning in the most general sense, η is also a tensor. More importantly, it should be remembered that the assumptions of Ohm's law are implicit in the derivation of the magnetic induction equation. Extensions to such general expressions are not treated in this work since for the pressures and magnetic field strengths considered in this work this assumptions are valid.

3.1.1 Electrical Conductivity

There are several models available to compute the electrical conductivity of an ionized gas. Most simplistically, Lin [20] proposed that the electrical conductivity is given by $\sigma^{-1} = \sigma_{en}^{-1} + \sigma_{ei}^{-1}$, where σ_{en} is the electrical conductivity due to the electron-neutral collisions and σ_{ei} is due to the electron-ion collisions. The Saha equation can be used to determine the electron number density which then can be used to determine σ_{en} and theoretical equations exist for σ_{ei}. Other models are reviewed elsewhere [21].

In this work, a more detailed mixture-averaged electrical conductivity is computed from first-order approximations to the Champan-Enskog equations. Such calculations rely on the computation of the modified collision integral, $\Delta_{jk}^{(1)}$, between species j and species k. The electrical conductivity is then computed as:

$$\sigma = \frac{e^2}{kT} \frac{n_e}{\sum_{k \neq e} n_k \Delta_{ek}^{(1)}} \tag{3.26}$$

where e is the electrical charge, k is Boltzmann's constant and $\Delta_{jk}^{(1)}$ is given by:

$$\Delta_{jk}^{(1)} = \frac{8}{3} \left[\frac{2W_j W_k}{\pi \hat{R} T (W_j + W_k)} \right]^{1/2} \pi \Omega_{jk}^{(1,1)} \tag{3.27}$$

where $\pi\Omega_{jk}^{(1,1)}$ is the collision integral of the momentum transfer between species j and species k. The number density is defined by $n_k = \rho Y_k \hat{N} / W_k$, where $\hat{N}$ is Avogadro's number and W_k is the kth-species molecular weight. Values of the collision integral between electrons and neutrals are determined either from experimental or theoretical data [22, 23, 24]. For electron-ion collisions, theoretical expressions are used [25].

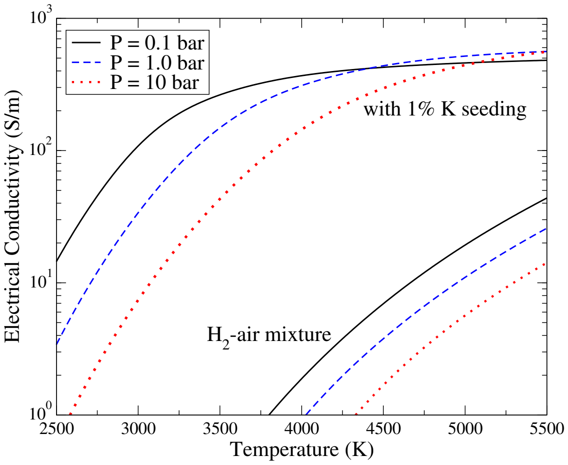

Figure 3.1: The equilibrium electrical conductivity is shown as a function of pressure and temperature for a stoichiometric H_2-air mixture. Seeding by potassium drastically increases the electrical conductivity.

3.1.2 Reaction and Ionization Mechanisms

Throughout this work, only reacting mixtures with hydrogen as the fuel are considered. Extension to other fuel-oxidizer mixtures is trivial, but for reacting mixtures with many species, the ionization mechanisms can become complex. For this reason, hydrogen-air mixtures are primarily studied. A combustion model developed by Petersen and Hanson [2] is used to determine H_2/O_2-N_2 reaction rates. The full hydrogen-oxygen chemistry is reduced to 18 elementary reactions and 8 primary species (H_2, O_2, OH, H, O, H_2O, HO_2, H_2O_2) and an inert species such as N_2 or Ar. The mechanism has been previously used in high-speed, high-pressure simulations of ram-accelerators and for simulating gaseous detonation of hydrogen-air mixtures [2, 26]. Table 8.1 lists the reactions and their Arrhenius coefficients.

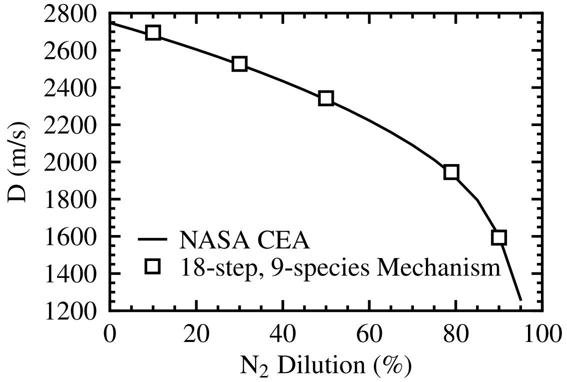

Figure 3.2: Comparison of the numerically computed detonation velocity for a H_2-air mixture at an ambient pressure and temperature of 0.2 bar and 298 K, respectively. The results are compared to theoretical computations of the detonation velocity obtained from NASA's CEA code.

This hydrogen-oxygen combustion model is combined with an independent kinetic mechanism to model the ionization of the post-detonation mixtures. These reactions include electron-impact ionization, electron-impact dissociation, associative ionization and charge-exchange reactions. Ionization of the secondary radical species HO_2 and H_2O_2 is neglected. The reaction coefficients for the Arrhenius rates of these elementary reactions are listed for each reaction in Table 8.2, along with the reference from which the data were obtained.

For studies of seeded mixtures, the reactions of potassium in a hydrogen-oxygen mixture are modeled using a reduced mechanism of 4 species (KO_2, KOH, KO, K) and 5 elementary reactions is included. The model has been used previously to analyze the affect of alkali salts in hydrocarbon flames [27]. The ionization of potassium is modeled through a single-step reaction, $M + K = M + e^- + K^+$, where M is any third-body species [28]. This combined reaction mechanism, consisting of 26 species and 65 reactions, is then used to compute the species mass fractions of the ionized gas. The electrical conductivity can then be computed from the species mass fractions and the thermodynamic state.

3.1.3 Dispersed Phase

Lagrangian tracking is used to compute the particle position, $x_{p,i}$, the particle velocity, $u_{p,i}$, and the particle temperature, T_p. In scenarios where the number of particles is too large for Lagrangian tracking to be computationally feasible, the parcel method [29, 30] can be used. A parcel is a group of one or more particles that all have the same position, velocity, and temperature. The approach reduces the computational cost since only the parcel is tracked. The number of particles per parcel needs to be judiciously chosen to ensure accuracy [31]. If there is no inter-phase mass transfer (inert particles), the solid-phase governing equations are given as

$$\frac{dx_{p,i}}{dt} = u_{p,i}, \tag{3.28}$$

$$m\frac{du_{p,i}}{dt} = \frac{\pi}{2}r_p^2 C_D \rho |\bar{u}_i - u_{p,i}|(\bar{u}_i - u_{p,i}), \tag{3.29}$$

$$mC_p\frac{dT_p}{dt} = 2\pi r_p \kappa_g \mathrm{Nu}(T - T_p), \tag{3.30}$$

where $\bar{u}_i$ is the local velocity of the gas, Nu is the gas-phase Nusselt number, r_p is the particle radius, and m is the particle mass, which is obtained as $(4/3)\pi r_p^3 \rho_p$ where ρ_p is the particle density. For this study, the model assumes that the pressure gradient term, the Basset term, the Saffman lift, the Magnus lift, and the inter-particle interaction term are all second-order affects [32, 30]. They are neglected in this study. The drag coefficient, C_D, is based on the following empirical relationship validated for shock-particle interactions [33]:

$$C_D = \left[0.38 + \frac{24}{\mathrm{Re}_p} + \frac{4}{\mathrm{Re}_p^{0.5}}\right]\left[1 + \exp\left(-\frac{0.43}{\mathrm{M}_p^{4.467}}\right)\right]. \tag{3.31}$$

In this expression, the drag is a function of the particle Reynolds number, $\mathrm{Re}_p{=}2r_p|u_{p,i} - u_i|\rho/\mu$, and the particle Mach number, $\mathrm{M}_p = |u_{p,i} - \bar{u}_i|/a_s$, where a_s is the speed of sound in the gas. Following previous studies [30], convection is assumed to be the dominant heat transfer mechanism between the two phases. The Nusselt number, Nu, used in Eq. 3.30, is computed as a function of Re_p and the Prandtl number, Pr, from the following relationship[34]: $\mathrm{Nu} = 2.0 + 0.459\mathrm{Pr}^{0.33}\mathrm{Re}_p^{0.55}$.

The governing equations for the solid-phase are integrated in time using a fourth-order Runge-Kutta scheme, and the inter-phase coupling terms in Eqs. 3.18 and 3.19 are the volumetrically-averaged quantities given as

$$\dot{F}_{p,i} = \frac{1}{\mathcal{V}}\sum_{n=1}^{N_p}\left[\frac{\pi}{2}r_{p,n}^2 C_{D,n}\rho_n|u_{p,i,n} - u_{i,n}|(u_{p,i,n} - u_{i,n})\right], \tag{3.32}$$

$$\dot{Q}_p = \frac{1}{\mathcal{V}}\sum_{n=1}^{N_p}\left[2\pi r_{p,n}\kappa_g \mathrm{Nu}_n(T_n - T_{p,n})\right], \tag{3.33}$$

$$\dot{W}_p = \frac{1}{\mathcal{V}}\sum_{n=1}^{N_p}\left[\frac{\pi}{2}r_{p,n}^2 C_{D,n}\rho_n|u_{p,i,n} - \bar{u}_{i,n}|(u_{p,i,n} - \bar{u}_{i,n})u_{p,i,n}\right], \tag{3.34}$$

where $\mathcal{V}$ is the volume of the computational cell, and the subscript n indicates a quantity of the nth parcel in the summation over the total number of particles in $\mathcal{V}$.

3.2 MHD Equations for Large-eddy Simulation

For turbulent flows of a sufficiently large Reynolds number, a separation of physical scales between the large, geometry-dependent scales and the small, universal scales occurs based on Kolmogorov's theory of turbulence. Large-eddy simulation (LES) methods rely on this assumption. By spatially filtering the governing equations of the flow, turbulent closure models can be developed to model the small, universal scalar and vector fluctuations, while the grid-resolved large-scale features are accurately computed. For compressible flows, Favre-filtering is typically used since the resulting LES equations are somewhat simpler. A Favre-filtered variable is defined by $\widetilde{f} = \overline{\rho f}/\overline{\rho}$. In the current work, a box filter with a width of $\overline{\Delta}$ is used, where $\overline{\Delta}$ is the average size of the computational cell. The LES-MHD equations are

$$\frac{\partial \bar{\rho}}{\partial t} + \frac{\partial \bar{\rho}\widetilde{u}_i}{\partial x_i} = 0, \tag{3.35}$$

$$\frac{\partial \bar{\rho}\tilde{u}_i}{\partial t} + \frac{\partial}{\partial x_j}\left(\bar{\rho}\tilde{u}_i\tilde{u}_j + \overline{p}\delta_{ij} - \overline{\tau}_{ij} - \overline{T}_{ij} + \tau_{ij}^{sgs} + T_{ij}^{sgs}\right) = 0, \tag{3.36}$$

$$\frac{\partial \bar{\rho}\widetilde{E}}{\partial t} + \frac{\partial}{\partial x_i}\Big[\left(\bar{\rho}\widetilde{E} + \overline{p}\right)\tilde{u}_i + \bar{q}_i - \tilde{u}_j\overline{\tau}_{ij} - \tilde{u}_j\overline{T}_{ij} - \overline{\eta}\epsilon_{ijk}\overline{B}_j\overline{J}_k \tag{3.37}$$

$$+ H_i^{sgs} + \sigma_i^{sgs} + \Sigma_i^{sgs} + P_i^{sgs}\Big] = 0, \tag{3.38}$$

$$\frac{\partial \bar{\rho}\widetilde{Y}_{(k)}}{\partial t} + \frac{\partial}{\partial x_i}\left[\bar{\rho}\widetilde{Y}_{(k)}\left(\tilde{u}_i + \widetilde{V}_{i,(k)}\right) + Y_{i,(k)}^{sgs} + \theta_{i,(k)}^{sgs}\right] = \dot{\bar{\omega}}_{(k)}, \tag{3.39}$$

$$\frac{\partial \overline{B}_i}{\partial t} + \frac{\partial}{\partial x_j}\left(\tilde{u}_j\overline{B}_i - \overline{B}_j\tilde{u}_i - \bar{\eta}\left(\frac{\partial \overline{B}_i}{\partial x_j} - \frac{\partial \overline{B}_j}{\partial x_i}\right) + \mathcal{E}_{ij}^{sgs} - d_{ij}^{sgs}\right) = 0. \tag{3.40}$$

All terms with superscript "sgs" indicate sub-grid scale terms requiring closure. Lastly, filtering the perfect gas equation of state results in,

$$\overline{P} = \bar{\rho}\widetilde{R}\widetilde{T} + \bar{\rho}\mathcal{R}_u T^{sgs}. \tag{3.41}$$

The total Favre-filtered conserved energy per unit volume becomes

$$\widetilde{E} = \tilde{e} + \frac{1}{2}\tilde{u}_i\tilde{u}_i + \frac{\overline{B}_i\overline{B}_i}{2\bar{\rho}\mu_0} + k^{sgs} + E_m^{sgs} \tag{3.42}$$

where $k^{sgs} = \frac{1}{2}[\widetilde{u_k u_k} - \tilde{u}_k\tilde{u}_k]$ is defined as the sub-grid kinetic energy, and $E_m^{sgs} = \frac{1}{2\bar{\rho}\mu_0}(\overline{B_i B_i} - \overline{B}_i\overline{B}_i)$ is defined as the sub-grid magnetic energy. The sub-grid scale terms requiring closure are defined explicitly as:

$$\tau_{ij}^{sgs} = \overline{\rho} \left(\widetilde{u_i u_j} - \widetilde{u}_i \widetilde{u}_j \right), \tag{3.43}$$

$$T_{ij}^{sgs} = \frac{\overline{B_i B_j} - \overline{B}_i \overline{B}_j}{\mu_0} - \left(\frac{\overline{B_k B_k} - \overline{B}_k \overline{B}_k}{2\mu_0} \right) \delta_{ij}, \tag{3.44}$$

$$H_i^{sgs} = \overline{\rho} \left(\widetilde{E u_i} - \widetilde{E} \widetilde{u}_i \right) + \left(\overline{u_i p} - \widetilde{u}_i \overline{p} \right), \tag{3.45}$$

$$\sigma_i^{sgs} = \left(\overline{u_j \tau_{ij}} - \tilde{u}_j \overline{\tau_{ij}} \right), \tag{3.46}$$

$$\Sigma_i^{sgs} = \left(\overline{u_j T_{ij}} - \tilde{u}_j \overline{T_{ij}} \right), \tag{3.47}$$

$$P_i^{sgs} = \overline{\eta \epsilon_{ijk} B_j J_k} - \overline{\eta} \epsilon_{ijk} \overline{B}_j \overline{J}_k, \tag{3.48}$$

$$Y_{i,(k)}^{sgs} = \overline{\rho} \left(\widetilde{u_i Y_{(k)}} - \widetilde{u}_i \widetilde{Y}_{(k)} \right), \tag{3.49}$$

$$\theta_{i,(k)}^{sgs} = \overline{\rho} \left(\widetilde{V_{i,(k)} Y_{(k)}} - \widetilde{V}_{i,(k)} \widetilde{Y}_{(k)} \right), \tag{3.50}$$

$$q_{i,(k)}^{sgs} = \overline{\rho} \left(h_{(k)} \widetilde{Y_{(k)} V_{i,(k)}} - \widetilde{h}_{(k)} \widetilde{Y}_{(k)} \widetilde{V}_{i,(k)} \right), \tag{3.51}$$

$$\mathcal{E}_{ij}^{sgs} = \left(\overline{u_j B_i} - \overline{u_i B_j} \right) - \left(\widetilde{u}_j \overline{B}_i - \widetilde{u}_i \overline{B}_j \right), \tag{3.52}$$

$$d_{ij}^{sgs} = \overline{\eta \frac{\partial B_i}{\partial x_j}} - \overline{\eta} \frac{\partial \overline{B}_i}{\partial x_j}, \tag{3.53}$$

$$T^{sgs} = \sum_{k=1}^{N_s} \frac{\widetilde{Y_{(k)} T} - \widetilde{Y}_{(k)} \widetilde{T}}{W_{(k)}}. \tag{3.54}$$

3.2.1 Turbulent closure model

The sub-grid terms are modeled based on a characteristic length scale taken as the local grid-width $\overline{\Delta}$ and a characteristic velocity obtained from sub-grid energy. Based on this scaling analysis, an eddy-viscosity and a magnetic eddy-viscosity can be defined as $\nu_t = c_{\nu_t} \overline{\Delta} \sqrt{k^{sgs}}$ and $\nu_T = c_{\nu,m} \sqrt{E_m^{sgs}/\mu_0} \overline{\Delta}$ respectively, such that the unclosed terms in the momentum equation can be closed as:

$$\tau_{ij}^{sgs} = -2\bar{\rho}\nu_t \left(\widetilde{S}_{ij} - \frac{1}{3} \widetilde{S}_{kk} \delta_{ij} \right) + \frac{2}{3} k^{sgs} \delta_{ij} \tag{3.55}$$

$$T_{ij}^{sgs} = -2\bar{\rho}\nu_T \left(\overline{M}_{ij} - \frac{1}{3} \overline{M}_{kk} \delta_{ij} \right) - \frac{1}{3} E_m^{sgs} \delta_{ij} \tag{3.56}$$

where $\widetilde{S}_{ij}$ and $\overline{M}_{ij}$ are the resolved rate of strain tensors defined as:

$$\widetilde{S}_{ij} = \frac{1}{2} \left(\frac{\partial \tilde{u}_i}{\partial x_j} + \frac{\partial \tilde{u}_j}{\partial x_i} \right) \qquad \text{and} \qquad \overline{M}_{ij} = \frac{1}{2} \left(\frac{\partial \overline{B}_i}{\partial x_j} + \frac{\partial \overline{B}_j}{\partial x_i} \right) \tag{3.57}$$

The three unclosed terms, H_i^{sgs}, σ_i^{sgs} and $\sigma_i^{sgs,m}$, in the conservation of energy equation are all modeled together as:

$$H_i^{sgs} + \sigma_i^{sgs} + \Sigma_i^{sgs} = (\bar{\rho}\nu_t + \mu) \left(\frac{\partial k^{sgs}}{\partial x_i} + \frac{\partial E_m^{sgs}}{\partial x_i} \right) - \frac{\bar{\rho}\nu_t c_p}{\mathrm{Pr_t}} \frac{\partial \widetilde{T}}{\partial x_i} + \tilde{u}_j \left(\tau_{ij}^{sgs} + T_{ij}^{sgs} \right) \tag{3.58}$$

where Pr_t is the turbulent Prandtl number. At present, the sub-grid Poynting flux, P_i^{sgs} is neglected. The sub-grid diffusion of species mass fractions, $Y_{i,(k)}^{sgs}$, is also modeled using an eddy-diffusivity assumption as:

$$Y_{i,(k)}^{sgs} = -\frac{\bar{\rho}\nu_t}{\mathrm{Sc_t}}\frac{\partial \widetilde{Y}_{(k)}}{\partial x_i} \tag{3.59}$$

where Sc_t is the turbulent Schmidt number. The diffusions due to sub-grid fluctuations in species diffusion velocity, $\theta_{i,(k)}^{sgs}$ and $q_{i,(k)}^{sgs}$, are neglected in the present study.

The sub-grid electromotive force tensor, $\mathcal{E}_{ij}^{sgs}$, is closed by approximating the turbulent electromotive force. From mean-field theory it can be shown that the electromotive force is a linear function of the mean magnetic field and its spatial derivatives, however, this theory assumes that the fluctuating velocity is statistically independent of the mean magnetic field. To include the velocity-magnetic field self-alignment effects an additional term is included. The turbulent electromotive force, $\mathcal{E}_{T,i}$, is then approximated as:

$$\mathcal{E}_{T,i} = \alpha\overline{B}_i - \beta\overline{J}_i + \gamma\widetilde{\Omega}_i \tag{3.60}$$

where

$$\beta = \frac{5}{7}\left(\nu_t\,\mu_0\right) \qquad \text{and} \qquad \gamma = \frac{5}{7}\left(\nu_T\,\mu_0\right) \tag{3.61}$$

where Ω_i is the Favre-filtered vorticity. Instead of using the kinetic helicity, H_v, to directly close the α term, non-local and history effects are incorporated using the sub-grid kinetic energy. The term is then modeled modeled as:

$$\alpha = c_\alpha\sqrt{k^{sgs}} \tag{3.62}$$

where the coefficient c_α is dynamically calculated, similar to the coefficients, $C_{\nu,v}$ and $C_{\nu,b}$ in the eddy viscosity and magnetic eddy diffusivity. As was expected, $\mathcal{E}_{T,i}$ is dependent on $\overline{B}_i$ and the mean current $\overline{J}_i$ $[= (1/\mu_0)\epsilon_{ijk}\partial\overline{B}_k/\partial x_j]$ through two coefficients α and β. The α term is related to the kinetic helicity, and the β term acts as a hyper-resistivity. This can be understood by noticing that $\beta\overline{J}_i$ can be merged into the diffusion term. Thus, β enhances the magnetic diffusivity $[\lambda \to \lambda + \beta]$. This is sometimes referred to as anomalous resistivity effect (β-effect) and is most important in magnetic confinement.

The last term, showing the dependency on the mean vorticity $\tilde{\Omega}_i$ $[= \epsilon_{ijk}\partial\tilde{u}_k/\partial x_j]$, however, is new. The coefficient, γ, is related to the cross-helicity and the self-alignment between the velocity and the magnetic field. This includes the non-linearity of the Alfvén effect into the turbulent electromotive force which is not typically included in mean-field theories.

The sub-grid magnetic diffusive flux, d_{ij}^{sgs}, is incorporated into the closure of the turbulent electromotive force, since it is likely that the β term in the expression of $\mathcal{E}_{T,i}$, which acts as an added turbulent dissipation term, would mask the effect of increased turbulent diffusion by d_{ij}^{sgs}. By solving a transport model for the sub-grid kinetic energy k^{sgs} and sub-grid magnetic energy E_m^{sgs}, the local values of the sub-grid kinetic and magnetic energies, k_v^{sgs} and k_b^{sgs}, can be used to evaluate the eddy-viscosity, the magnetic eddy-viscosity and α coefficient. These transport equations are given as:

$$\frac{\partial \bar{\rho} k^{sgs}}{\partial t} + \frac{\partial}{\partial x_j}\left(\bar{\rho}\tilde{u}_j k^{sgs}\right) = \frac{\partial}{\partial x_j}\left(\bar{\rho}\frac{\nu_t}{Pr_t}\frac{\partial k^{sgs}}{\partial x_j}\right) - \frac{\bar{\rho} C_\epsilon}{\bar{\triangle}}\left(k^{sgs}\right)^{\frac{3}{2}} - \tau_{ij}^{sgs}\frac{\partial \tilde{u}_j}{\partial x_i} - T_{ij}^{sgs}\frac{\partial \tilde{u}_j}{\partial x_i}$$
$$- \frac{C_{p,b}}{\bar{\triangle}}\sqrt{k^{sgs}} E_m^{sgs} \quad (3.63)$$

$$\frac{\partial E_m^{sgs}}{\partial t} + \frac{\partial}{\partial x_j}\left(\tilde{u}_j E_m^{sgs}\right) = \frac{\partial}{\partial x_j}\left(\bar{\eta}\frac{\partial E_m^{sgs}}{\partial x_j}\right) - \frac{C_{\epsilon,b} E_m^{sgs}\sqrt{E_m^{sgs}/\bar{\rho}}}{\bar{\triangle}}$$
$$- \frac{1}{\mu_0} T_{ij}^{sgs}\frac{\partial \bar{B}_i}{\partial x_j} - E_m^{sgs}\frac{\partial \tilde{u}_j}{\partial x_j} \quad (3.64)$$

3.3 Quasi-linear and Quasi-static MHD Equations

The MHD equations can exhibit complex, non-linear dynamics, but for many problems this set of governing equations can be greatly simplified. Specifically, it is often possible to linearize or even eliminate the coupling between the magnetic and velocity fields. Using dimensional analysis, the second-order terms in Eqs. 3.17-3.22 can easily be deduced and neglected. In MHD, there are four fundamental dimensional scales, i.e., length (m), mass (kg), time (sec), and electric current (A). If only the momentum and magnetic flux conservation equations are considered, there four independent non-dimensional parameters: the magnetic Prandtl number, Pr_m, the magnetic Reynolds number, Re_m, the Lundquist number, S, and the interaction parameter or Stuart number N.

The magnetic Prandtl number is the ratio of the kinematic and magnetic diffusivities,

$$Pr_m = \mu_0 \sigma \nu, \quad (3.65)$$

where ν is the kinematic viscosity (μ/ρ) and $(\mu_0\sigma)^{-1}$ is the magnetic diffusivity (η). In the majority computational studies of MHD turbulence, the magnetic Prandtl number is often assumed to be unity. There are several instances where this is a poor assumption. In experimental studies of the turbulent dynamo, liquid metals are often used because of their high conductivities, however, Pr_m for these liquids is extremely small. The magnetic Prandtl number is related to two other non-dimensional parameters, the Reynolds number, $Re = uL/\nu$, and the magnetic Reynolds, given as

$$Re_m = \mu\sigma u L = Re Pr_m. \quad (3.66)$$

Thus, the assumption of $Pr_m = 1$ is equivalent to assuming $Re = Re_m$. The significance of the magnetic Reynolds number as a non-dimensional measure of conductivity has already been discussed. Another non-dimensional parameter is the Lundquist number:

$$S = \sqrt{\frac{\mu}{\rho}}\sigma B L = \mu\sigma V_a L \quad (3.67)$$

where $V_a = B/\sqrt{\mu\rho}$ is the Alfvén velocity. Thus, the Lundquist number is essentially a magnetic Reynolds number based on the Alfvén velocity. This expression is used often in studies of magnetic plasma confinement. As a side note, the magnetic field is often expressed in Alfvén units, where the magnetic field is modified, ($B'_k = B_k/\sqrt{\rho\mu_0}$), to have the same units as the velocity. The Elassässer variables, $z_i = u_i \mp B'_i$ can then be used to simplify the incompressible MHD equations. In these cases, the Lundquist number is more natural than the magnetic Reynolds number. Such simplifications are not possible, however, in compressible flows. Lastly, the interaction parameter, N, is important in MHD turbulence of low magnetic Reynolds number.

$$N = \frac{\sigma B^2 L}{\rho u} \tag{3.68}$$

When $Re_m << 1$, the induced magnetic fields diffuse quickly and can be neglected relative to the imposed magnetic field, B_0. The induced currents, however, play a dominant role in the conversion of the Lorentz force into heat via the process of ohmic dissipation, which occurs at a time-scale of τ_η. This process is highly anisotropic. Fluids motions misaligned with the magnetic field are preferentially dissipated at a rate which is proportional to $\cos\theta^2$ where θ is the angle between B_0 and the wavenumber vector k. As a result, an elongation of vortical structures along the direction of B_0 is observed. These effects are counteracted, however, by the natural development of the non-linear flow. The magnetic interaction parameter or Stuart number, N, is a measure of the balance of the inertial and Lorentz forces. For example, in the simplistic scenario of a decaying isotropic turbulent flow, vortex flux tubes, aligned in direction of the magnetic field, begin to form with the complete transition to a two-dimensional turbulent state independent of B_0 at very large N [35].

In these situations, the magnetic induction equation, Eq. 3.21, can be linearized by expanding the magnetic field about a constant external magnetic field component as, $B_i = B_{ex,i} + b_i$, where b_i represents the induced (or fluctuating) component. This results in

$$\frac{\partial B_{ex,i}}{\partial t} + \frac{\partial b_i}{\partial t} - \frac{\partial}{\partial x_i}\left(u_j B_{ex,i} - u_i B_{ex,j}\right) - \frac{\partial}{\partial x_i}\left(u_j b_i - u_i b_j\right) - \eta\frac{\partial^2 B_{ex,i}}{\partial x_i^2} - \eta\frac{\partial^2 b_i}{\partial x_i^2} = 0 \tag{3.69}$$

Assuming that the external field component is stationary and homogenous, this equation can be simplified to

$$\frac{\partial b_i}{\partial t} - \frac{\partial}{\partial x_i}\left(u_j B_{ex,i} - u_i B_{ex,j}\right) - \frac{\partial}{\partial x_i}\left(u_j b_i - u_i b_j\right) - \eta\frac{\partial^2 b_i}{\partial x_i^2} = 0 \tag{3.70}$$

The order of magnitude of each term is determined by non-dimensionalizing the above equation using the following scales

$$x_i^\star \longleftrightarrow \frac{x_i}{L} \tag{3.71}$$

$$u_i^\star \longleftrightarrow \frac{u_i}{V} \tag{3.72}$$

$$b_i^\star \longleftrightarrow \frac{b_i}{B} \tag{3.73}$$

$$B_{ex,i}^\star \longleftrightarrow \frac{B_{ex,i}}{B_0} \tag{3.74}$$

$$t_u^\star \longleftrightarrow \frac{t}{L/V} \tag{3.75}$$

$$t_d^\star \longleftrightarrow \frac{t}{\eta/L^2} \tag{3.76}$$

where there are two important time scales, a characteristic fluid time scale, L/V, and a magnetic diffusion time scale, η/L^2. Non-dimensionalizing by the fluid time scale the following expression can be derived:

$$\frac{VB}{L}\frac{\partial b_i}{\partial t} - \frac{VB_0}{L}\frac{\partial}{\partial x_i}\left(u_j B_{ex,i} - u_i B_{ex,j}\right) - \frac{VB}{L}\frac{\partial}{\partial x_i}\left(u_j b_i - u_i b_j\right) - \frac{\eta B}{L^2}\frac{\partial^2 b_i}{\partial x_i^2} = 0 \tag{3.77}$$

Simplifying this expression, results in the following expression,

$$Re_m\frac{\partial b_i}{\partial t} - \left[Re_m\frac{B_0}{B}\right]\frac{\partial}{\partial x_i}\left(u_j B_{ex,i} - u_i B_{ex,j}\right) - Re_m\frac{\partial}{\partial x_i}\left(u_j b_i - u_i b_j\right) - \frac{\partial^2 b_i}{\partial x_i^2} = 0 \tag{3.78}$$

If $Re_m << 1$, then all the terms of the order of the magnetic Reynolds number can be neglected. The quantity B_0/B is of order of N/Re_m where N is interaction parameter, and is indicative of the fact that for large interaction parameters, large currents are induced in the flow. Assuming that the interaction parameter is at least of order unity, then the quasi-static form of the magnetic induction equation is obtained,

$$\frac{\partial^2 b_i}{\partial x_i^2} = -\left[Re_m\frac{B_0}{B}\right]\frac{\partial}{\partial x_i}\left(u_j B_{ex,i} - u_i B_{ex,j}\right) \tag{3.79}$$

Using Ohm's law and including the non-dimensional, incompressible momentum conservation equation for reference, the quasi-static MHD equations are

$$\begin{gathered}\frac{\partial u_i}{\partial t} + \frac{\partial}{\partial x_j}\Big(\rho u_i u_j + p\delta_{ij}\Big) = S^2\epsilon_{ijk}j_j B_{ex,k} + Pr_m\frac{\partial \tau_{ij}}{\partial x_j} \\ j_i = \epsilon_{ijk}u_j B_{ex,k}\end{gathered} \tag{3.80}$$

The quasi-linear approximation can be obtained by non-dimensionalizing the magnetic diffusion time-scale. This retains the time-dependence of the induced magnetic field, and the following set of equations are obtained

$$\begin{gathered}\frac{\partial u_i}{\partial t} + \frac{\partial}{\partial x_j}\Big(\rho u_i u_j + p\delta_{ij}\Big) = \frac{S^2}{Re_m^2}\epsilon_{ijk}j_j B_{ex,k} + \frac{Pr_m}{Re_m}\frac{\partial \tau_{ij}}{\partial x_j} \\ \frac{\partial b_i}{\partial t} = \frac{\partial}{\partial x_j}\Big(u_j B_{ex,i} - B_{ex,j}u_i\Big) + \frac{1}{Re_m}\frac{\partial b_i}{\partial x_j^2}\end{gathered} \tag{3.81}$$

CHAPTER IV

COMPUTATIONAL METHODS

In the recent decade, there has been a substantial maturity in the application of a wide variety of numerical methods to the equations of MHD, particularly in the development of shock-capturing methods for the study of discontinuous compressible flows. Much of this development has been directed in the field of astrophysics where several open-source MHD codes are currently available, e.g. ZEUS-MP, ATHENA, AMRVAC, Pencil, Nirvana, RAMSES, PLUTO, and FLASH, where most commonly, the MHD equations are typically solved in the conservative, finite-volume (or finite-difference) form with some higher-order Godunov-type method used for shock-capturing. Yet, in general, any numerical method can be used, and there are equally as many examples of the use of discontinuous Galerkin methods, pseudo-spectral methods, finite-element methods, etc., in the study of MHD. Unique to the numerical methods of MHD, however, is the requirement of maintaining a zero-divergent magnetic field. This constraint requires careful consideration and often increases the complexity of the numerical formulation in comparison to the more typical hydrodynamic methods. A wide variety of techniques exist to enforce this condition. These methods are reviewed later in more detail.

The numerical formulation presented in the current work is unique in its treatment of the MHD-LES equations and its ability to switch between a shock-capturing scheme and a high-order, low dissipation central scheme. This hybrid scheme is ideal for simulations of turbulence involving flow discontinuities. Central schemes, being dispersive, create numerical oscillations around steep gradients resulting in unphysical values. High-order Godunov-type methods, however, while dissipative in nature are able to numerically resolve strong gradients in the flow resulting formation of shocks and rarefactions typical of any non-linear hyperbolic system. In MHD, the dispersion relation emanates a richer variety of characteristics than in more familiar hydrodynamic relationship. In general, there are four characteristic waves: fast magneto-acoustic waves, slow magneto-acoustic waves Alfvén waves, and contact discontinuities. Thus, the Godunov-type methods in MHD are more diverse and complicated. More explanation of both the central and upwind schemes used in this study is presented in the subsequent discussion, but many of the details on the algorithmic implementation are discussed in greater depth elsewhere [36].

4.1 Numerical Integration

By defining vectors of the conserved and primitive variables as $\mathbf{Q} = [\rho, \rho u_x \rho u_y, \rho u_z, E, B_x, B_y, B_z]$ and $\mathbf{W} = [\rho, u_x, u_y, u_z, p, B_x, B_y, B_z]$, respectively, the MHD equations in a Cartesian coordinate system can be expressed more simply as:

$$\frac{\partial \mathbf{Q}}{\partial t} + \frac{\partial \mathbf{F}}{\partial x} + \frac{\partial \mathbf{G}}{\partial y} + \frac{\partial \mathbf{H}}{\partial z} = 0, \tag{4.1}$$

where **F**, **G** and **H** are the flux vectors in the $x-$, $y-$, and $z-$directions, respectively, which for an inviscid, ideal MHD flow are given by the following relationships:

$$\mathbf{F}=\begin{bmatrix}\rho u_x\\ \rho u_x^2+p+B^2/2-B_x^2\\ \rho u_x u_y-B_xB_y\\ \rho u_x u_z-B_xB_z\\ (\rho E+p)u_x-(\mathbf{B}\cdot\mathbf{u})B_x\\ 0\\ B_yu_x-B_xu_y\\ B_zu_x-B_xu_z\end{bmatrix},\quad \mathbf{G}=\begin{bmatrix}\rho u_y\\ \rho u_y u_x-B_yB_x\\ \rho u_y^2+p+B^2/2-B_y^2\\ \rho u_y u_z-B_yB_z\\ (\rho E+p)u_y-(\mathbf{B}\cdot\mathbf{u})B_y\\ B_xu_y-B_yu_x\\ 0\\ B_zu_y-B_yu_z\end{bmatrix},\quad \mathbf{H}=\begin{bmatrix}\rho u_z\\ \rho u_z u_x-B_zB_x\\ \rho u_z u_y-B_zB_y\\ \rho u_z^2+p+B^2/2-B_z^2\\ (\rho E+p)u_z-(\mathbf{B}\cdot\mathbf{u})B_z\\ B_xu_z-B_zu_x\\ B_yu_z-B_zu_y\\ 0\end{bmatrix} \tag{4.2}$$

Extending the above system of equations to a multi-species, viscous, and resistive MHD flow is trivial. Also, in general, this system of equations are solved in curvilinear coordinates, which requires modifying these vectors by the appropriate metrics. It is important to mention that while the last three components of these vectors represent the magnetic induction fluxes, the actual fluxes used in time-evolving the magnetic field are typically different in implementation depending on the numerical method used to enforce the magnetic divergence to zero.

4.1.1 The $\nabla\cdot\mathbf{B}=0$ constraint

During the numerical integration of the MHD equations, numerical errors can propagate and build-up such that the solenoidal condition on the magnetic field, $\partial B_k/\partial x_k = 0$, becomes violated. Ideally, this problem would be solved by increasing the grid resolution since $\partial B_i/\partial x_i$ converges to zero as the grid resolution Δx and Δt approach zero. Unfortunately, this negates the purpose of LES and increases computational time unnecessarily. Thus, a numerical scheme is necessary to force $\partial B_i/\partial x_i \approx 0$ at each time-step. A comprehensive discussion is given by Tóth [37]. Two schemes are used. The *projection scheme* [38] , which enforces the constraint in some discretization by the projection of the magnetic field, and the *constrained transport scheme* [39] which conserves $\partial B_i/\partial x_i$ to machine accuracy during the flux computation. In the current implementation, when a magnetic field with some non-zero values of $\partial B_k/\partial x_k$ is initially introduced, the *projection scheme* is used to eliminate any errors. During the simulation, *constrained transport scheme* [40] is used to avoid accumulation of the truncation error.

4.1.2 Finite Volume Formulation

The finite-volume form of the conservation equations is obtained by integrating Eq. 4.1 over the volume of the computational cell, V, and using Green's theorem to express the volume integral as a surface integral over the face area of the computational cell, Σ. This results in the following expression

$$\frac{\partial\mathbf{Q}}{\partial t}+\frac{1}{V}\oint_{\Sigma}\left(\mathbf{F}n_x+\mathbf{G}n_y+\mathbf{H}n_z\right)d\Sigma=\mathbf{S}. \tag{4.3}$$

where the source-term vector **S** has also be included for generality. The primitive variables, **W**, are now explicitly defined as cell-centered quantities averaged over the volume of the computational cell. Similarly, the flux vectors **F**, **G**, and **H** are defined at the interfaces between neighboring computational cells and represent quantities averaged over the area of each face. In the structured grid framework adopted throughout this study, the computational cell with the coordinates (i, j, k) has six interfaces $\sigma_{l=1\ldots6}$ located at $(i \pm 1/2, j, k)$,$(i, j \pm 1/2, k)$,$(i, j, k \pm 1/2)$. If the fluxes normal to the surfaces of any computational cell are denoted as $F_l = F_x n_x + F_y n_y + F_z n_z$, the cell-centered variables Q are incremented in a dimensionally-split manner by:

$$dQ = -\frac{dt}{V} \sum_{l=1,\ldots,6} (F_l \sigma_l) + S dt \tag{4.4}$$

where dt is the discrete time interval over which the conservation equations are evolved. Time integration is then performed using a two-stage Runge-Kutta method. This first stage is referred to as the *predictor* step, and the second as the *corrector* step. The flux evaluation in the McCormack method differs during each stage of the time-integration. Mathematically, this is illustrated as:

$$\begin{aligned} \text{Predictor:} \qquad & Q^{(*)} = Q^{(n)} + dQ^{(n)} \\ \text{Corrector:} \qquad & Q^{(n=1)} = \frac{1}{2}\left[Q^{(n)} + Q^{(*)} + dQ^{(*)}\right] \end{aligned} \tag{4.5}$$

where $dQ^{(*)}$ and $dQ^{(n)}$ are obtained from Eq. 4.4. This time integration is second order accurate in time and the spatial accuracy of the scheme is determined by the evaluation of the fluxes at the cell interfaces. In the hybrid formulation, these fluxes are either evaluated using a second or fourth order central-differencing scheme or a first or second order upwind shock-capturing scheme. Details about these schemes are given elsewhere.

4.1.3 Flux Computation

There has been a considerable amount of research in the development of high-order Godunov-type methods for MHD flows. These methods rely on accurate solutions to the MHD Riemann problem. Exact solutions are computationally expensive, thus any practical scheme must use approximate solutions to the MHD Riemann problem. Brio and Wu [41], proposed the first approximate MHD Riemann based on a Roe-type linearized Riemann solver [42]. Since then, there have been many other approximate MHD Riemann solvers proposed [43, 44, 45, 40]. To mention a few, an extension of the piecewise-parabolic method (PPM) [46] to MHD has been proposed by Dai and Woodward [47], and Powell [48] has proposed a unique variant of the MHD Riemann problem that ensures the magnetic field remains solenoidal. Most Godunov-type schemes for MHD are known to not preserve a divergent-free magnetic field since the eight characteristic corresponding to $\nabla \cdot \vec{B}$ is not included.

A family of approximate Riemann solvers called HLL, named for the developers Harten, Lax, and van Leer [49], can be easily adapted to MHD flows because of its generality. In the HLL formulation, N characteristic waves are assumed to sub-divide each cell interface into N+1 constant-property regions. Closed-form expressions for each of the N+1 states and their corresponding fluxes can be derived by applying the Rankine-Hugoniot jump relations across each wave and calculating (or approximating) each of N characteristic wave-speeds. Harten et al. [49] carried out a full derivation for a two-wave problem, but did not specify an procedure for the evaluation of the the characteristic wave-speed. Since then, many variants of the HLL-type Riemann solver have been developed, including the HLLD Riemann solver derived by Miyoshi for MHD flows [50]. Since a three-wave HLL Riemann solver, HLLC, has previously been implemented for hydrodynamic flows, the HLLD was natural choice for extending the capability to MHD flows. The HLLD Riemann solver has also been demonstrated to preform relatively well compared to other Riemann solvers [50].

In order to permit the simulations of turbulent flows in supersonic and/or explosive environments, a hybrid methodology has been developed. The shock-capturing is used in regions of strong discontinuities, whereas the central scheme, adapted to the resolution of turbulent, reacting flows, is used everywhere else. The integration of this method in the hybrid formulation requires sensing strong discontinuity regions from a smoothness sensor. The switch used in this study is similar to that presented in [51] and applied to practical turbulent problems in [36]. A smoothness parameter S_i is formulated based on variables curvatures [52]:

$$S_i = \frac{|Q_{i+1} - 2Q_i + Q_{i-1}|}{|Q_{i+1} - Q_i| + |Q_i - Q_{i-1}|}, \tag{4.6}$$

where Q can be any variable of interest. Both pressure and density are used to sense the smoothness of the flow. To prevent switching on numerical noise, a threshold value for the denominator is defined. The smoothness S_i is set to 0 if either the numerator or the denominator is less than $0.06Q_i$. The cell is identified as $non-smooth$ if the smoothness parameter exceeds a threshold value of 0.5. In multi-dimensional problems, the transverse fluxes to that cell are also tagged as non-smooth, and all fluxes are evaluated with the shock-capturing scheme. In all other cases, the smooth spatial discretization is used.

4.2 Numerical Verification

4.2.1 One-dimensional Shock Tube

The ability of the shock-capturing methodology to resolve flow discontinuities is evaluated using a series of well-known one-dimensional shock tube tests, which are commonly used in the literature for testing MHD schemes[3, 37, 50]. In all of the tests conducted, the computational domain extending from 0 to 1 meter is discretized by 800 grid points. A calorically perfect equation of state is used, and the ratio of specific heats, γ, is assumed to be constant ($\gamma = 5/3$). With a gas constant of unity, the equation of state simplifies to $p = (\gamma - 1)(E - (1/2)u^2 - (1/2\mu_0)B^2)$ where E is the total energy.

In the first test, the results shown in Fig. 4.1, all the ordinary MHD waves are present: two fast shocks (M=1.22 and 1.28), two slow shocks (M=1.09 and 1.07), two rotational discontinuities (θ=12° and 9°) and a contact discontinuity. The numerical results using the implemented HLLD scheme are plotted at t=0.2 sec and are compared to the exact solution of the Riemann problem [3] for both the first-order and second-order upwind numerical schemes. A second test by Ryu and Jones [4] show a slow-compound shock followed by a rarefaction wave. This solution, shown in Fig. 4.2, is unique to numerical implementations of approximate Riemann solvers [50, 37].

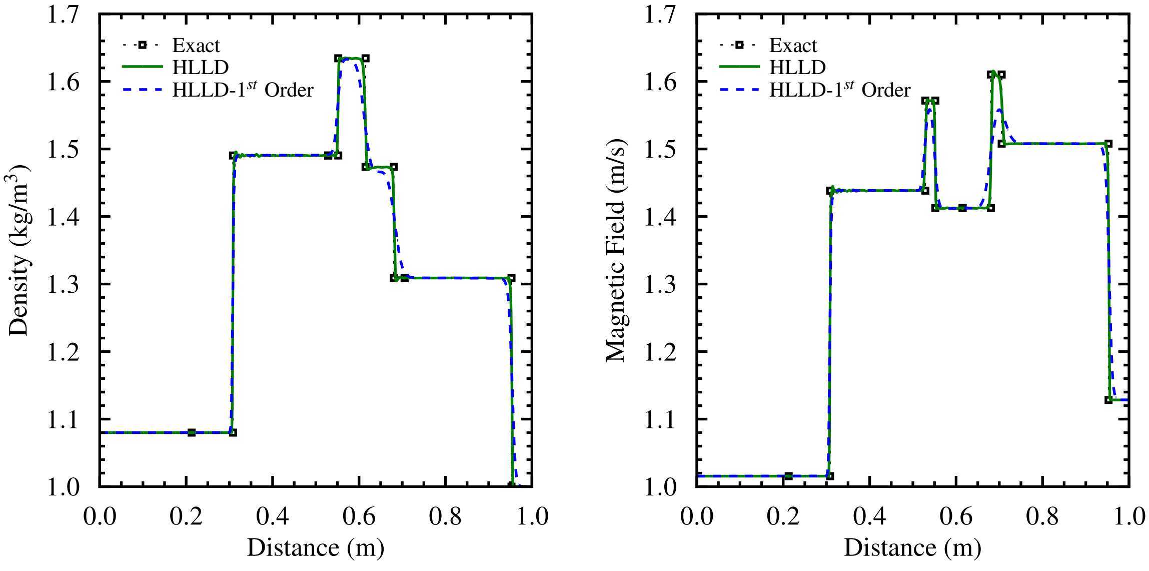

(a) (b)

Figure 4.1: (a) Density and (b) magnetic field profiles at t=0.2 seconds for the Dai-Woodward MHD test case [3] for first and second order upwind scheme using the HLLD Riemann solver.

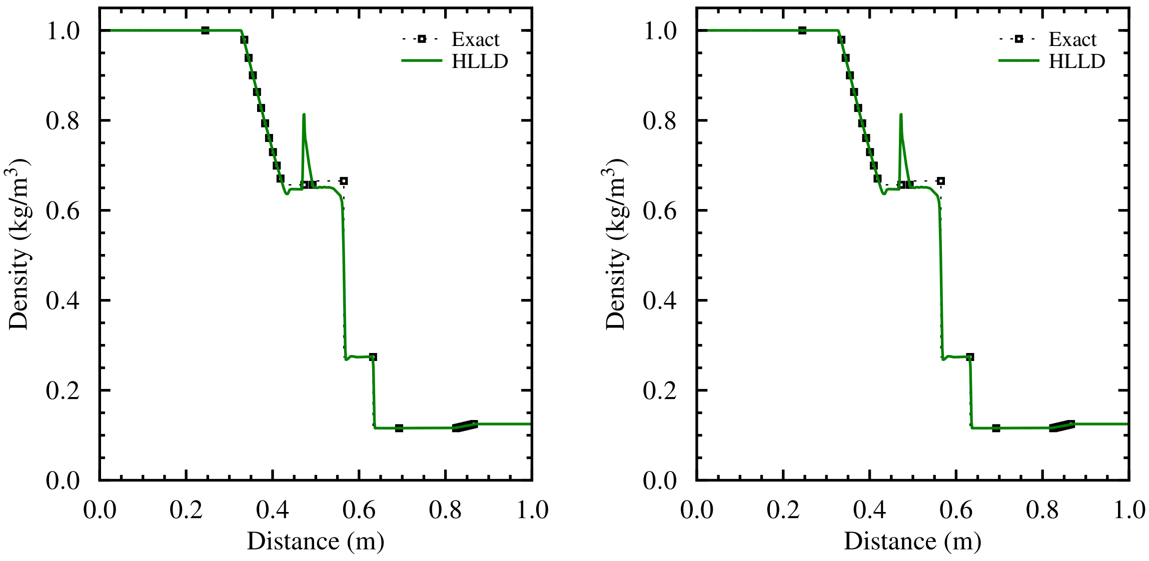

(a) (b)

Figure 4.2: (a) Density and (b) magnetic field profiles at t=0.1 seconds for the Ryu-Jones MHD test case [4] for the second order upwind scheme using the HLLD Riemann solver.

4.2.2 Orszag-Tang Vortex

Extension of the one-dimensional upwind-type MHD solver to multiple dimensions is not straight-forward because of the solenoidal constraint on the magnetic field. Several methods have been proposed to remove the numerical divergence errors, however, in this work,

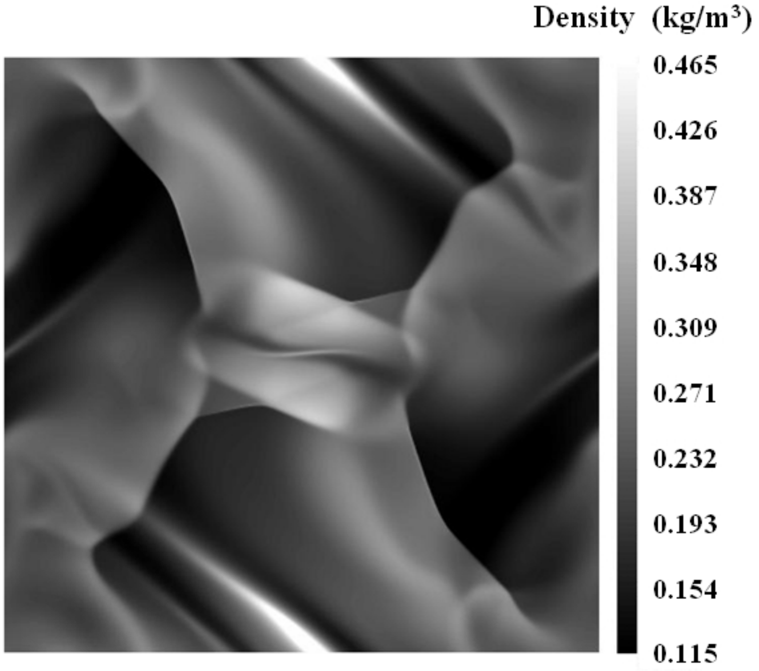

Figure 4.3: Normalized temperature contours for the Orszag-Tang vortex problem at t=π seconds.

the constrained transport method has been integrated into the HLLD solver. The Orszag-Tang vortex problem [53] is commonly used as a two-dimensional test for MHD schemes. In the evolution of the vortex several types of MHD shocks interact. The complexity of the problem has thus made it a successful test for the robustness of multi-dimensional MHD schemes. The problem is defined by the initial conditions $(\rho, p, u, v, w, B_x, B_y, B_z) = (\gamma^2, \gamma, -\sin y, \sin x, 0, -\sin y, \sin 2x)$ in a square $2\pi\times 2\pi$ domain. The vortex is fully-developed at t=π seconds. A resolution of 400×400 is used with a CFL number of 0.4.

The temperature contours for the Orszag-Tang vortex is shown in Fig. 4.2.2. The flow structures are qualitatively similar to simulations done by others [37, 50]. The centerline temperature values are compared to a solution computed by Miyoshi using the HLLD solver. Keep in mind a gas constant of 1 has been used, so the temperature values have in reality been normalized. The are some discrepancies between the the values even though both use the HLLD Riemann solver.

4.2.3 Hartmann Channel

For a laminar Hartmann channel flow, analytical solutions exist. The flow is assumed to be fully-developed and uniformly electrically conducting (σ is constant) with mutually perpendicular electric and magnetic fields. The magnetic field is applied externally in the y-direction, and an external electric field is applied in the z-direction. The velocity, $\vec{u} = (u_x, 0, 0)$, interacts with the electromagnetic fields resulting in a Lorentz force that opposes the motion of the fluid.

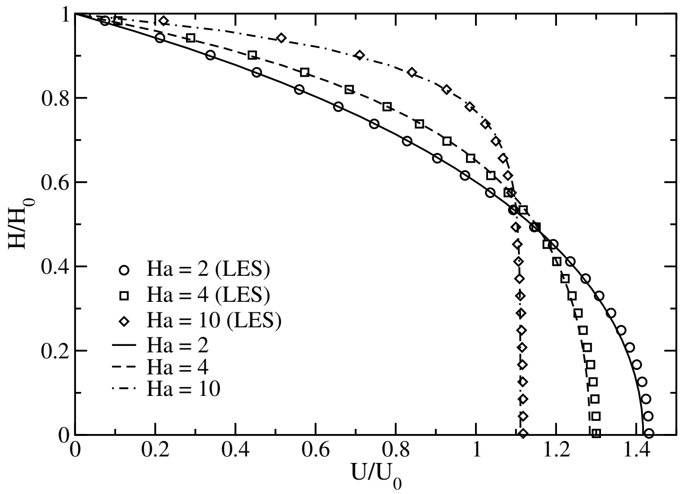

Figure 4.4: Normalized velocity profiles for laminar Hartman flow. Here, H_0 and U_0 denote the half-channel height and velocity averaged in the transverse direction, respectively. The lines indicate the analytical solution for the different Hartman numbers.

$$F_x = -\sigma B_{ex,y}^2 u_x \tag{4.7}$$

The presence of this force significantly modifies the boundary layer thickness since the Lorentz force must be balanced by the pressure gradient and the viscous stresses. As the magnetic field strength is increased, the boundary layer thickness is reduced. An analytical solution for the velocity profile in a fully-developed Hartmann flow is given as:

$$u_x(y) = u_o \left[1 - \frac{cosh(Ha)y/h_{1/2}}{cosh(Ha)} \right] \tag{4.8}$$

where $h_{1/2}$ is the half hight of the channel, and Ha is the Hartman number, defined as:

$$Ha = B_{y,ex} h_{1/2} \sqrt{\frac{\sigma}{\rho\nu}} \tag{4.9}$$

The quasi-static MHD equations, Eq. 3.80, are solved numerically and compared to the analytical solution. The results are shown in Fig. 4.4.

CHAPTER V

ACCOMPLISHMENTS AND NEW FINDINGS

5.1 Gaseous Detonation

Previous research into the plasma production by detonation and explosion have relied on equilibrium point calculations. A more in depth understanding of the time-dependent and spatial processes involved in the ionization of post-detonation flows can be obtained by numerical simulation. Such simulations are a first step in deducing accurate models for conductivity in detonating mixtures, and form a basis for the more complicated analysis of investigating the effects of external electromagnetic fields. A finite-rate detailed kinetic mechanism for the ionization and detonation of H_2/O_2-N_2 mixtures is proposed and validated. The focus of the current effort is a study of the spatial and time-dependent characteristics of the electrical conductivity in post-detonation gases, and the effects of varying ambient pressure and N_2 dilution. The observed equilibrium conductivities are typically in the range of 10^{-2}-10^{-1} $(\Omega\ \text{m})^{-1}$, which are similar to the experimental observations [54, 55].

For this study, the full MHD equations presented above, Eqs. 3.17–3.22, are not required since no electric or magnetic field is present. Here the unsteady, compressible Euler equations for a reacting, calorically perfect gas are solved. Thus the magnetic and viscous terms are set to zero in Eqs. 3.17–3.22 and Eq. 3.21 is not necessary.

5.1.1 One-Dimensional Detonation

A detonation wave forms when a strong shock wave dynamically couples to a reaction-wave in such a way that a balance occurs between the release of chemical energy and the energy required to sustain the shock wave. In the simplest of models, a detonation wave is described as an one-dimensional discontinuity propagating through the mixture at the Chapman-Jouget (CJ) velocity. The theory is surprisingly well-supported. Experimental measurements are within 1-2% of the theoretical CJ velocity [56]. As a result one-dimensional simulations can be useful in understanding the affects of N_2 dilution, pressure and seeding on the ionization of the post-detonation mixture.

The computational domain is discretized with a uniform resolution of 10 μm. This resolution is shown to be sufficient in Section 5.1.2. The left boundary is treated as a slip wall and at right boundary all variables are extrapolated. A direct initiation is numerically modeled by initializing a region of high pressure and temperature at the left boundary and allowing the detonation to develop naturally as the gas expands through the unburned mixture. This approach is similar to other studies reported [57]. The initiation is setup to result in a detonation with an overdrive factor close to unity where the overdrive factor, f, is defined as $(D/D_{CJ})^2$ where D is the velocity of the detonation wave and D_{CJ} is the Chapman-Jouget or CJ detonation speed. Once the detonation is initiated with the correct propagation velocity, the remainder of the simulation is then carried out in the frame of

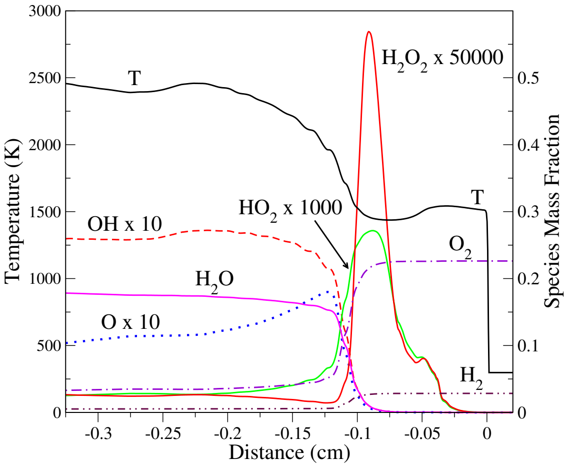

Figure 5.1: (a) One-dimensional profiles of temperature and species mass fraction directly behind the detonation-sustained shock wave. The results are shown for a stoichiometric H_2-air detonation in an ambient pressure and temperature of 0.2 bar and 298 K, respectively.

reference of the moving detonation.

The boundary conditions are then changed accordingly to supersonic inflow and outflow boundaries. In the following discussion, the baseline results for a stoichiometric detonation of H_2-air at an ambient pressure of 0.2 bar and temperature of 298 K are first presented followed by parametric studies where the pressure, dilution and seeding percentage are varied with respect to the baseline.

Figure 5.1 shows profiles of temperature and mass fractions of a few species just downstream of the detonation front. The initial sharp rise in the temperature is a result of the propagating shock wave ($M_s = 4.76$). The temperature ratio across the shock is 5.17 and compares reasonably well to the theoretical value of 5.32. The difference is attributed to the instability of the detonation, which is illustrated in Fig. 5.2a. The average peak pressure is only slightly over-predicted. Following the shock wave, radicals are formed in the induction zone as the reactants, H_2 and O_2, begin to break-down. The sharp increase in the radicals H_2O_2 and HO_2 marks the beginning of heat release. As the temperature increases downstream (with N_2/O_2 and ionization chemistry), N_2 begins to break down, and the presence of N atoms prompts the Zel'dovich reactions and the beginning of NO formation.

Since NO has a low ionization potential, the electrical conductivity is directly dependent on the formation of NO ions [55]. This is demonstrated by computing the species number densities, which are shown in Fig. 5.2b. Since the ionized mixture is assumed to be quasi-neutral, the electron number density, n_e, must be equal to the positive ion number density. Here n_e=3.052×10^{17} m^{-3} and n_{NO^+}=2.956×10^{17} m^{-3}. From Eq. 3.26, the electrical conductivity is seen to be directly proportional to n_e. Thus the formation of NO ions is critical to increasing the electrical conductivity of the mixture. Even though both OH and NO are easily ionizable, the production of NO ions dominates. This is because the concentration of OH is depleted downstream due to formation of H_2O resulting in a negligible contribution to the n_e by OH ion production ($n_{OH^+} = 21.33$ m^{-3}). Non-stoichiometric H_2/O_2 detonations

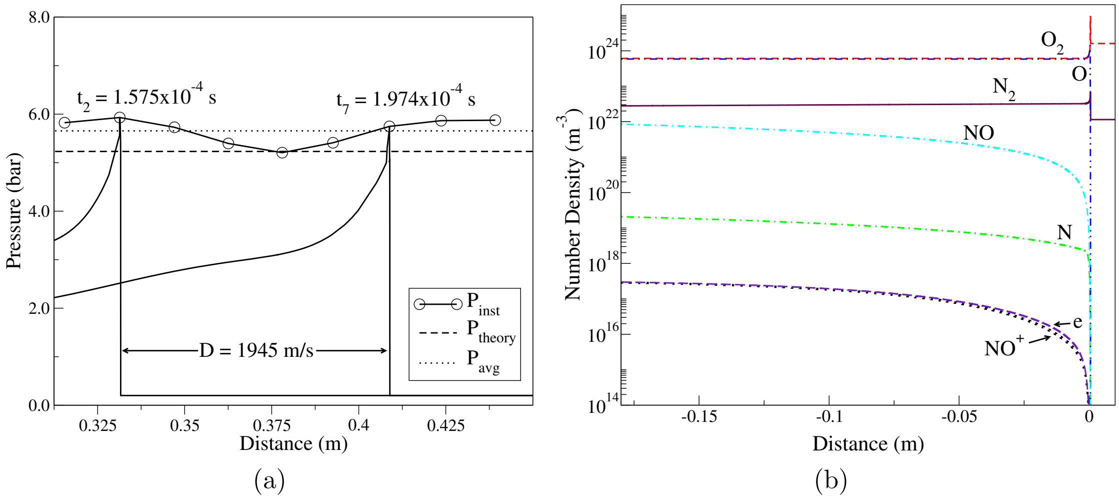

(a) (b)

Figure 5.2: (a) One-dimensional profiles of pressure shown at two instances in time as the detonation propagates through the domain. The peak pressures oscillate indicating the detonation is in the oscillatory regime [5]. Both results are shown for a stoichiometric H_2-air detonation in an ambient pressure and temperature of 0.2 bar and 298 K, respectively. (b) One-dimensional profiles the species number density showing the important role of NO formation in the ionization process.

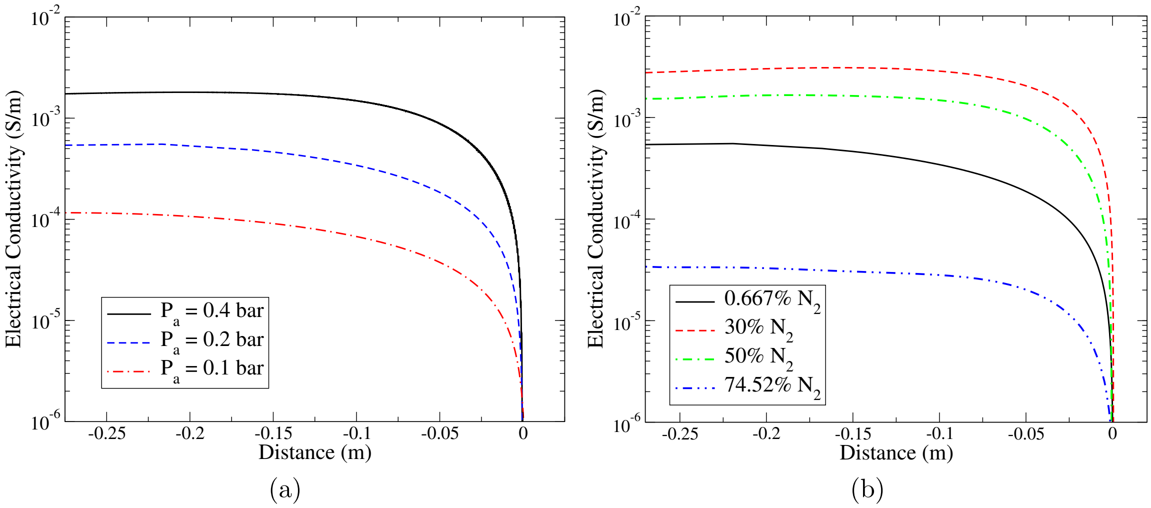

(a) (b)

Figure 5.3: (a) One-dimensional profiles of the electrical conductivity computed for a stoichiometric H_2/O_2 mixture with 0.667% N_2 dilution at three different ambient pressures. (b) A comparison of the electrical conductivity at different N_2 dilutions. The peak post-detonation temperature for 0.667%, 30%, 50%, and 79% N_2 dilution is 3408, 3265, 3180, 2751 K respectively.

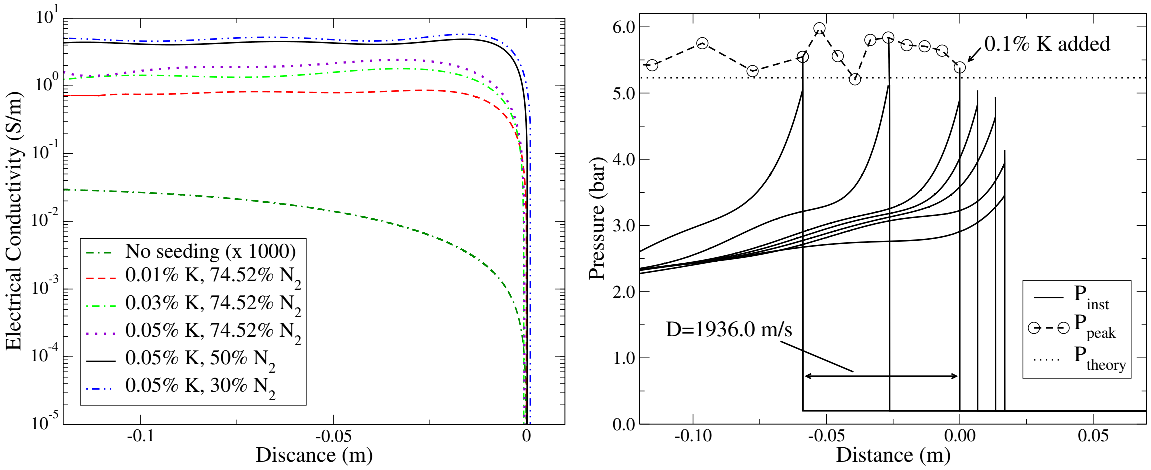

(a) (b)

Figure 5.4: (a) A comparison of the electrical conductivity at different potassium seeding percentages. The reference case for detonation of a stoichiometric H_2-air mixture at ambient pressure and temperature of 0.2 bar and 298 K is shown for comparison. (b) At seeding percentages higher than 0.06%K the detonation wave decays into a propagating shock wave.

could possibly reveal OH ionization to be of more significance.

As the ambient pressure increases, the formation of NO occurs earlier and its equilibrium value increases slightly. This in turn increases the electrical conductivity. The trend is easily observable in the profiles of the electrical conductivity shown in Fig. 5.3a. Similarly, as the dilution of the N_2 is reduced, the electrical conductivity also increases as shown in Fig. 5.3b. Both affects are largely a result of the change in the post-detonation temperature. As the ambient pressure is increased from 0.1 bar to 0.4 bar, the detonation velocity increases roughly 2.75 percent with a corresponding 6.7 percent rise in temperature. This increases the reaction rates in the post-detonation mixture and thus increases NO formation. Also as the temperature is increased, N_2 is more easily dissociated. Similar logic applies to why the electrical conductivity increases at lower N_2 concentrations. The reduction of N_2 reduces the heat capacity of the mixture and thus increases the detonation velocity and post-detonation temperature. However, as observed in Fig. 5.3b, the trend reverses at low concentrations regardless of the higher post-detonation temperatures since the reduction of N_2 limits NO production because of the lack of available nitrogen.

As mentioned previously, detonations in H_2-air mixtures produce ionized mixtures with low electrical conductivities of order 10^{-3} S·m^{-1}. In order to increase these values potassium can be used to seed the gas with easily ionizable particles. In experiments, potassium is typically injected into the flow as atomized salt particles such as potassium carbonate. These particles quickly decompose and undergo phase change [27]. However to simplify the current study the phase change process is not modeled and gaseous KOH is injected uniformly at the inflow plane instead. The injected KOH then convects until it reacts at the detonation front due to the elevated temperatures and pressures as well as the presence of H and OH radicals. Gaseous potassium quickly forms which ionizes and increases the electron number density of the mixture. Figure 5.4a shows the electrical conductivity for potassium seedings of 0.01,

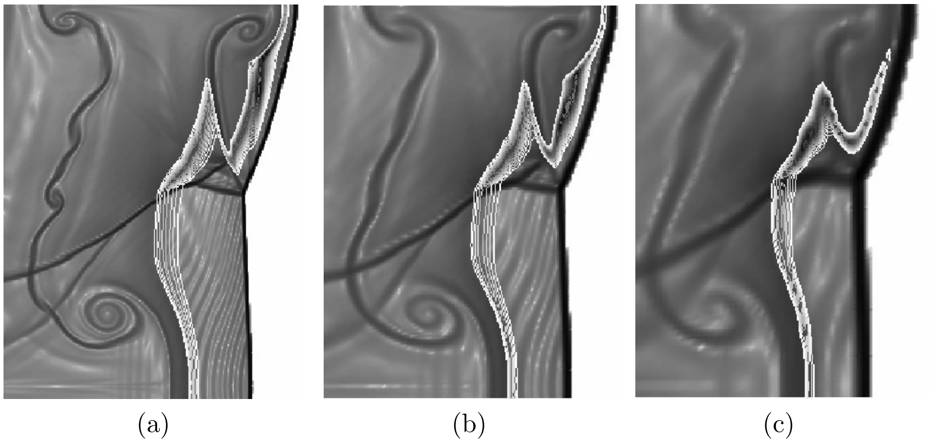

(a) (b) (c)

Figure 5.5: Contours of the $\ln(|\bigtriangledown\rho| + 1)$ and of the mass fraction of H_2O_2 (in white) delineate the prominent features of gaseous detonations. The grid resolution is varied from (a) 5μm, (b) 10μm and (c) 20μm to determine the minimum grid resolution required.

0.03 and 0.05 percent by weight. The electrical conductivity not only increases at a faster rate but is 4 orders of magnitude larger than the electrical conductivity of the unseeded detonation.

In the one-dimensional studies conducted, a potassium seeding of larger than 0.06% was observed to kill the detonation as demonstrated in Fig. 5.4b. This is a result of the potassium chemistry competing for the O and H radicals necessary for combustion. This disruption increases the induction time for combustion which subsequently causes the heat release zone to decouple from the shock wave triggering a reduction in the the heat release such that the propagating shock can no longer be sustained. This process is observable in the pressure profiles shown in Fig. 5.4b. The detonation profiles following the addition of the seed are shown approximately every 20 μs. The peak pressures as well as the CJ peak pressure are shown prior to the seeding as reference.

This result is in some contradiction to experiments which use higher seeding percentages [58, 21]. Yet this is expected since in one-dimension the detonation lacks the structure necessary for self-propagation and therefore is more sensitive to the disruptions caused by seeding. This does not, however, invalidate the conclusions drawn from these simulations. While in two and three dimensions the detonation may be more impervious to potassium seeding, a critical point most likely exists where too much seeding results in a failure of the detonation. This is investigated in the next section.

5.1.2 Potassium seeding in two-dimensional detonation simulations

A two-dimensional stoichiometric hydrogen-air detonation is simulated by initializing the domain with a one-dimensional solution. As in the one-dimensional simulations, the detonation is simulated in the frame of reference moving with the detonation wave. The boundaries in the y-direction are taken as periodic, and a simulation domain of 18 mm × 3 mm is used. From a grid-resolution study, a 10 μm resolution is determined to be sufficient to resolve the Mach stem, incident shock and transverse wave interactions at the detonation front. This interaction, shown in Fig. 5.1.1 for three different grid resolutions, is critical in sustaining the detonation as it creates local zones of high pressure and temperature causing the detonation front to pulsate in the direction of propagation. This introduces fluid mixing time-scales which impact the electrical conductivity in the post-detonation mixture.

In order to ascertain the minimum required resolution, a grid-independent study is performed. The criteria for grid-independence is based on the resolution of the triple-point interaction between the Mach stem, incident shock and transverse way [59]. This structure is critical in sustaining the detonation as it creates a zone of high pressure and temperature that causes the gas to expand as chemical energy is released. Figure 5.1.1 shows the triple-point structure of the detonation for half of the channel at three different resolutions: 5, 10 and 20 μm. At the highest resolution, the incident shock, Mach stem and the transverse shock are clearly defined as well as are the slip-lines. Overlaid on these figures in white are the contour lines of the mass fraction of the H_2O_2 radical, which indicates the region of heat release. In comparison to Fig. 5.5a and Fig. 5.5b, the detonation features in Fig. 5.5c are not clear, indicating that a resolution of 20 μm is inadequate. In Fig. 5.5b, the features are reasonably resolved, especially the secondary triple point due to the strong transverse wave, hence a uniform resolution of 10 μm is used in the remainder of the studies. Though the results are shown for the H_2/O_2 combustion chemistry, the results are no different with the combined mechanism thus the results are shown for brevity.

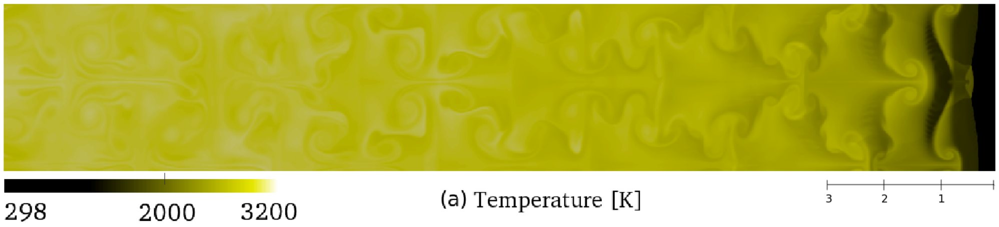

(a) Temperature [K]

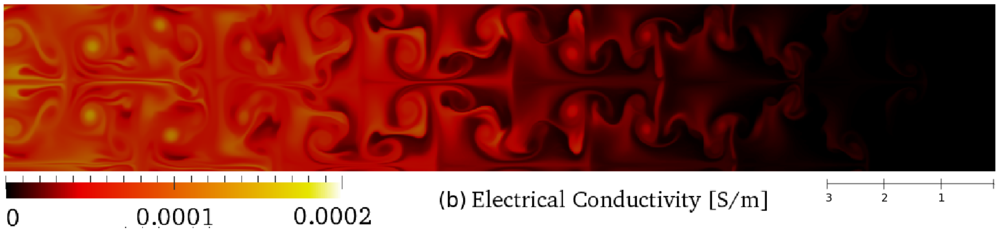

(b) Electrical Conductivity [S/m]

Figure 5.6: Stoichiometric H_2-air detonation at an ambient temperature and pressure of 298 K and 0.2 atm. (a) Contours of temperature, and (b) the electrical conductivity. The length scale shown is in millimeters.

Since the location of the transverse wave, incident shock and Mach stem interaction oscillates perpendicularly to the detonation front a series of vortical structures separated by slip lines are propagated downstream creating a non-uniform distribution of temperature and species mass fraction as illustrated in Fig. 5.1.2. Only in the regions of high temperature does significant dissociation of N_2 and NO formation occur. As the vortices interact and merge, the high temperature regions become less distinct and the ion density becomes more uniform. As a result, the distance between the weakly-ionized plasma and the detonation front is both a result of the mixing rate of the vortices and the chemical non-equilibrium of the explosion

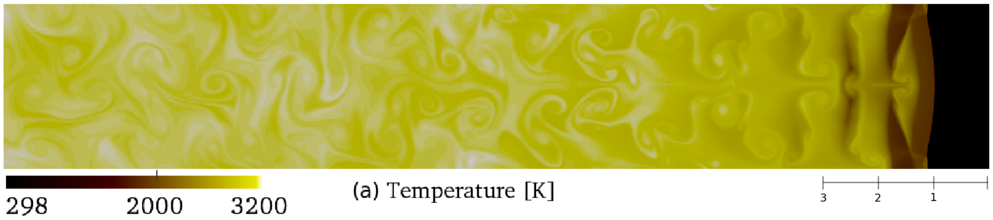

(a) Temperature [K]

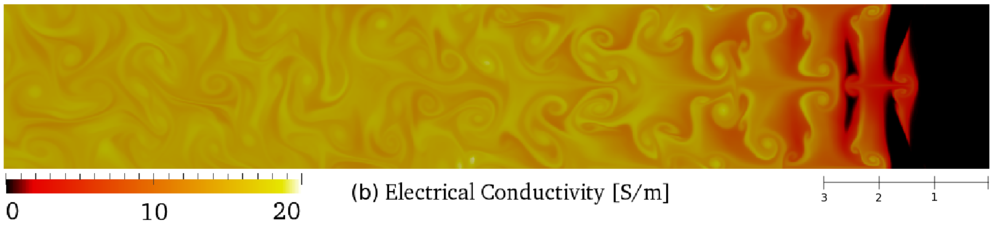

(b) Electrical Conductivity [S/m]

Figure 5.7: Stoichiometric H_2-air detonation at an ambient temperature and pressure of 298 K and 0.2 atm seeded with 1% K by weight. (a) Contours of temperature, and (b) the electrical conductivity. The length scale shown is in millimeters

.

products. This creates a non-uniform distribution of the electrical conductivity with peak values of order 10^{-3} S·m^{-1}, which are similar to those observed in the one-dimensional simulations.

When KOH is injected into the inflow, the ionization mechanism becomes dominated by the potassium chemistry. The ionization is now prompt, occurring at the detonation front, and is no longer rate-limited by the slow formation of NO. This could have important consequences in applications where an external magnetic field is present since a combination of a high electrical conductivity at the detonation front and a strong magnetic field could alter the way the transverse waves interact at the detonation front. Figure 5.7 shows contours of the electrical conductivity and the electron number density.

The main difference from the one-dimensional and two-dimensional simulations is that the strong interaction between the Mach stem, incident shock and transverse waves at the detonation front creates local regions of high temperature and pressure. These regions of heat release allow for the two-dimensional detonation to sustain higher mass fractions of potassium seeding. Yet above a seeding of 1.25 percent by weight of K, the detonation becomes unstable and decays into a propagating shock wave. This indicates that the ionization fraction of the gas mixture that can be achieved through detonation is limited. This constraint is imposed along with the additional problems of uniform mixing and burning of the seed particles. Extending these conclusions to three dimensions, some increase in the seeding limit could be hypothesized since in three dimensions the nature of the shock-wave interactions will result in higher peak pressures and temperatures [30].

5.1.3 Conclusions

The electrical conductivity of a plasma produced by a hydrogen-air detonation is computed. The proposed detailed chemistry is able to model both hydrogen-oxygen combustion and

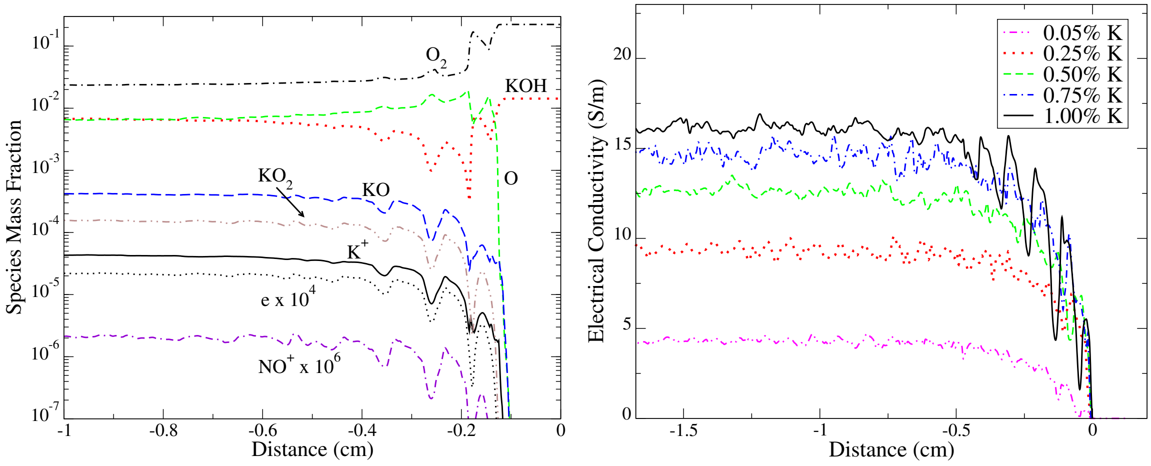

(a) (b)

Figure 5.8: (a) Planar averaged mass fractions of the species involved in potassium ionization behind the detonation front with 1% K seeding. (b) Planar averaged profiles of the electrical conductivity for various potassium seeding percentages.

ionization in hydrogen-air mixtures. Basic detonation properties, such as D_{CJ}, are reproducible at various pressures and N_2 dilutions indicating that the numerical approach is both robust and accurate. For unseeded detonations, ionization is slower as a result of the relatively slow formation of NO. At higher ambient pressures, the post-detonation temperature is increased resulting in an increase in the electrical conductivity. Reducing the N_2 dilution also increases the post-detonation temperature and the electrical conductivity until the reduction of nitrogen in the mixture begins to limit NO production. Since the observed electrical conductivities in unseeded detonations are too low for MHD devices to be efficient, seeding the mixture with low ionization potential alkali salts is necessary. While seeding does increase the electrical conductivity, simulations in both one and two dimensions show that the detonation is sensitive to the amount of seeding material injected into the flow. Too high of a seeding percentage can adversely affect the detonation propagation, however, even at lower seeding percentages (less than 1.25%) a four to five order of magnitude increase in the electrical conductivity is observed.

5.2 Condensed-Phase Explosion

It was previously observed that gaseous detonation without seeding produces a plasma with a relatively low conductivity when compared to measured conductivities of $1300 S \cdot m^{-1}$ that have been observed for condensed-phase explosions. We now consider a nitromethane charge of $5.9 cm$ uniformly filled with aluminum particles. The condensed-phase explosion is simulated on a 45 degree sector grid with a maximum radius of 2.4 m. The Euler equations must now be coupled with the Lagrangian equations for the particles. For brevity, the details are not included here. The development of this modeling capability is apart of a separate DTRA thrust area. The simulation methodology has been previously validated and used extensively in the analysis of effect of initial particle loading on blast-wave physics

[60]. Here we are interested in how the particles contribute to the electrical conductivity of mixture. The electrical conductivity of the gas can be computed using the method presented previously for gaseous detonation. The particle conductivity is assumed to be constant and a property of its composition only. Using two-phase mixture rules, a theoretical formula for the effective electrical conductivity can be calculated. One such mixture rule is the Rayleigh-Maxwell relation, given as:

$$\frac{\sigma_{eff}}{\sigma_{gas}} = 1 + \frac{3\alpha}{\left(\frac{\sigma_{particle}-2\sigma_{gas}}{\sigma_{particle}-\sigma_{gas}}\right) - \alpha} \tag{5.1}$$

where α is the volume fraction. Figure 5.9 shows the time history of the electrical conductivity for nitromethane charge uniformly loaded with aluminum particles. As indicated on the plot, the initial peak in electrical conductivity is a result of gaseous ionization in the high temperature and pressure region of the outward propagating shock wave. As the shock wave dissipates the temperature and pressure drops reducing the contribution of gaseous ionization to the electrical conductivity. At long times it is the particles that maintain the electrical conductivity of the products. The computation of the electrical conductivity in such mixtures is significantly more complicated, and is a area of work requiring the development of more sophisticated computational models.

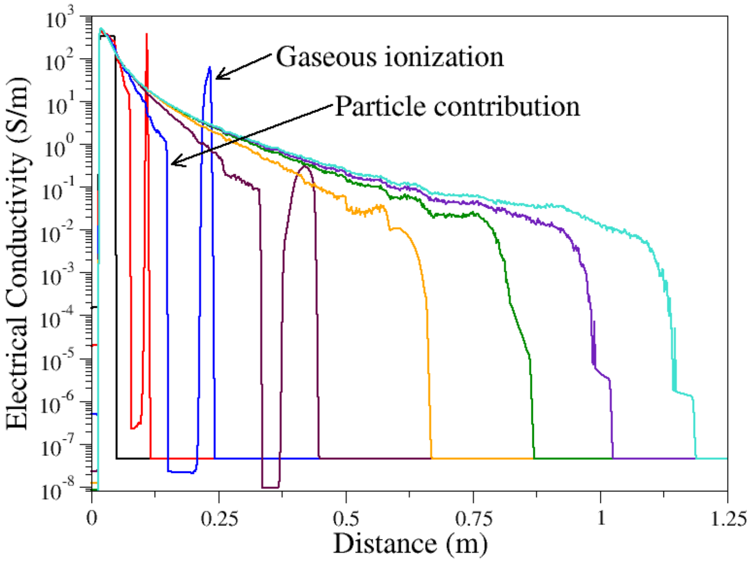

Figure 5.9: A time-history of the electrical conductivity for a condensed-phase explosion of a nitromethane change uniformly loaded with aluminum particles. The contributes do to gaseous ionization and particles are indicated on the plot.

5.3 MHD Detonation

Experiments and simulations presented in the previous section indicate that gaseous detonation waves generate a weakly ionized plasma in the post-detonation region [58, 19]. Depending on the composition of the mixture, the ionization processes can vary widely, but for stoichiometric hydrogen-air mixtures, computational simulations using detailed combustion and ionization kinetics seem to indicate that the production of NO ions is the most prominent pathway in the generation of a weakly-ionized plasma [19, 61]. Given such mixtures, the average electrical conductivity in the post-detonation is of the order of 10^{-3} S/m. Practical engineering applications involving the use of magnetohydrodynamic (MHD) forces to manipulate the flow for generation of electrical power, propulsive thrust, etc., however, require higher levels of electrical conductivity, and thus the mixture must be seeded with particles of a low ionization potential to increase the flow's electrical conductivity [21]. The numerical studies of potassium-seeded detonations presented in the previous section indicate that a substantial increase in the electrical conductivity is possible, but that the amount of seeding added is limited since much of the available heat release from combustion is diverted to the ionization process rather than to sustaining the detonation wave [19]. Given these prior studies, a range of electrical conductivities can be identified as feasible in practical engineering applications involving gaseous detonations. The physics of how an electromagnetic field interacts with the conducting products of a detonation and how that interaction might affect the stability and the propagation of the detonation wave is now systematically addressed.

A distinctive feature of MHD flows is the generation of induced currents resulting from the relative motion of a conductive fluid in an external magnetic field not aligned with the flow velocity. These currents introduce an additional mechanism for the dissipation of energy within the flow, which is characterized by the magnetic diffusivity, $\eta = 1/\mu\sigma$, where μ is the permeability of free space, and σ is the electrical conductivity. Most importantly, however, is the ratio of the time scale of magnetic diffusion ($\tau_\eta = \eta^2/L$) to the flow time scale ($\tau_u = u/L$), where u and L are the characteristic velocity and length scales. This ratio is defined as the magnetic Reynolds number, $Re_m = \tau_\eta/\tau_u = u/L = \mu\sigma uL$. For a typical ionizing hydrogen-air detonation, Re_m is estimated to be of the order of 10^{-3}. For MHD flows, when $Re_m << 1$, the induced magnetic fields diffuse quickly and can be neglected relative to the imposed magnetic field, B_0. The induced currents, however, play a dominant role in the conversion of the Lorentz force into heat via the process of ohmic dissipation, which occurs at a time-scale of τ_η. This process is highly anisotropic. Fluids motions misaligned with the magnetic field are preferentially dissipated at a rate which is proportional to $\cos\theta^2$ where θ is the angle between B_0 and the wavenumber vector k. As a result, an elongation of vortical structures along the direction of B_0 is observed. These effects are counteracted, however, by the natural development of the non-linear flow. The magnetic interaction parameter or Stuart number, N, is a measure of the balance of the inertial and Lorentz forces and is given by $N = \sigma B_0^2 L/\rho u$, where ρ is the density of the gas. For example, in the simplistic scenario of a decaying isotropic turbulent flow, vortex flux tubes, aligned in direction of the magnetic field, begin to form with the complete transition to a two-dimensional turbulent state independent of B_0 at very large N [35]. For detonations, the dynamics of the flow are complicated by the persistent energy release and generation of large-scale fluid structures at

Table 5.1: A summary of parameter set for the simulations used in this study. To compute the non-dimensional parameters the following reference values were used: L=6 mm, $u = 1900$ m/s, ρ_0=0.17 kg/m^3 where L is the transverse channel dimension, $u \approx D$, and ρ is the ambient density. The MHD cases are distinguished by a X indicating the magnetic field is in the direction of the detonation propagation (x-direction), and a Y indicating the magnetic field is perpendicular to the direction of the detonation propagation (y-direction). These cases are compared against the hydrodynamic simulations of case NF (No-Field).

Case	σ (S/m)	Re_m	N
NF	0.0	0.0	0.0
X1,Y1	0.001	1.43×10^{-8}	0.0186
X2	0.01	1.43×10^{-7}	0.186
X3	0.001	1.43×10^{-8}	1.86
X4,Y4	0.01	1.43×10^{-7}	18.6
X5	0.01	1.43×10^{-7}	74.3
X6	0.01	1.43×10^{-7}	186.0
X7	0.01	1.43×10^{-7}	464.0
X8	0.01	1.43×10^{-7}	1860.0

the detonation front.

To investigate the effect of a magnetic field on the propagation of a detonation, numerical simulations are conducted for various magnetic Reynolds numbers and interaction parameters under the assumption of $Re_m << 1$. The external field is applied in either perpendicular or parallel to the direction of the propagation of the detonation. This study relies on previous numerical simulations [19] of stoichiometric hydrogen-air detonations for estimates of the electrical conductivity in the post-detonation flow. As such, only a finite-rate kinetic mechanism for the combustion process is included in the numerical simulation, and the electrical conductivity is assumed to be spatially uniform and constant in the post-detonation region. Flow parameters, along with the reaction zone widths, are analyzed to quantify the effect of the applied field on the detonation.

To initialize the detonation simulation, a direct initiation is first numerically modeled to obtain the correct detonation profiles with an overdrive factor close to unity. The overdrive factor, f, is defined as $(D/D_{CJ})^2$ where D is the velocity of the detonation wave and D_{CJ} is the Chapman-Jouget or CJ detonation speed. This detonation profile, shown in Fig. 5.19, is then used to initialize the two-dimensional simulations, which are performed in the frame of reference of the moving detonation. The boundary conditions in the direction of the detonation propagation are modeled as non-reflecting supersonic inflow and outflow boundaries. In the transverse directions, the boundaries are set to be periodic [30]. Although, the current formulation has been validated for a wide range of ambient pressures and diluent concentrations [19], for all cases here, the ambient pressure and temperature are 0.2 bar and 298 K, respectively.

Numerical simulations are conducted for different Re_m, N, and magnetic field orientations i.e., parallel ($B_{0,x}$) and transverse ($B_{0,y}$) to the detonation propagation. Table 5.1 summarizes

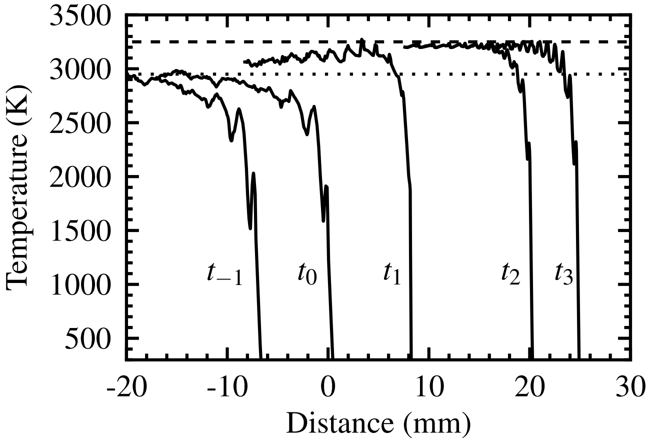

Figure 5.10: The averaged temperature profiles for case Y4 at different times: $t_{-1} = 0.104$ ms, $t_0 = 0.113$ ms, $t_1 = 0.127$ ms, $t_2 = 0.149$ ms and $t_3 = 0.157$ ms.

the parameters studied in this work. Since $Re_m << 1$, the non-dimensional parameter Re_m, however, is of less importance, and N and the magnetic field orientation govern the dynamics of the detonation. The value of Re_m is recorded to ensure the validity of the quasi-static assumption. At $t_0 = 0.113$ ms of case NF (no-field), the magnetic field is switched on. The magnetic field is always taken as positive, since in two dimensions, the components of the Lorentz force do not change (only the orientation of the current density changes), and thus the detonation dynamics are unchanged.

The computational domain is discretized using an uniform resolution (Δx). The value of Δx is chosen in order to spatially resolve the half-reaction length ($L_{1/2}$) and the evolution of species mass fractions [30]. For the ambient conditions and the gaseous mixture considered here, $\Delta x = 10$ μm is sufficient to resolve the detonation front (see Fig. 5.1.1) i.e. the interaction between the Mach stem (M), incident shock (I), and transverse wave (T). At this resolution, the grid resolution provides 80 points per theoretical $L_{1/2}$. Thus, for the current investigations, $\Delta x = 10$ μm is considered adequate.

A detonation propagating in a reactive gaseous mixture can be described as a shock wave sustained by the energy release from the shock-induced reaction. Thus, any mechanism affecting the shock strength and altering either the post-shock conditions and/or the chemical reaction rates can affect the propagation and stability characteristics of the detonation. For example, the inclusion of chemically inert particles in a gas mixture can been used to control the detonation propagation, and in some situations, such methods can be used to achieve detonation quenching [30]. Another possible method for detonation control could be achieved by application of an external magnetic field. This interaction is discussed in the following sections. Results are compared to simulations of no applied magnetic field, and for all cases simulated here, the transformed MHD detonation returns to the hydrodynamic detonation structure, i.e., detonation velocity, cell-width, etc., after some time of the field being switched off.

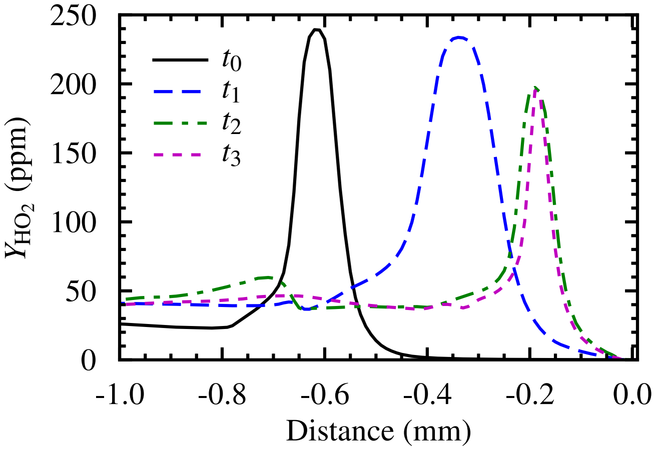

Figure 5.11: The profiles of mass fraction of HO_2 taken at the transverse location corresponding to the center of Mach stem for case Y4 at different times: $t_0 = 0.113$ ms, $t_1 = 0.127$ ms, $t_2 = 0.149$ ms and $t_3 = 0.157$ ms.

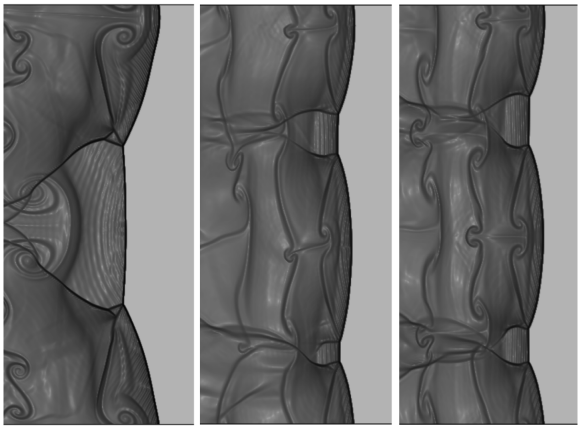

Figure 5.12: Plot of $\ln(|\nabla\rho| + 1)$ for case Y4 showing the structure of the detonation front at $t_0 = 0.113$ ms, $t_2 = 0.149$ ms and $t_3 = 0.157$ ms.

5.3.1 Effect of $B_{y,0}$

When the magnetic field is applied, the electromagnetic energy generated by action of the Lorentz force in the post-detonation flow is quickly converted into heat via joule dissipation. In particular, since the induced currents are largest at the detonation front, a significant amount of electromagnetic energy is deposited directly in the induction zone of the detonation. For case Y4, the post-detonation temperature increases by nearly 450 K after the magnetic field is turned on. Moreover, the Joule dissipation does not decrease in time as in decaying problems due to the continual formation of new scales from combustion at the detonation front. As the temperature gradually increases, see Fig. 5.10, the reaction zone length reduces, and the distance to the peak HO_2 mass fraction reduces to 0.2 mm from 0.7

mm as in the case NF (see Fig. 5.11). A characteristic of propagating detonations is the formation of cellular structures whose cell widths in transverse direction are dependent on $L_{1/2}$ [62]. These structures create characteristic large-scale structures in the post-detonation flow. In case Y4, smaller cellular structures are formed in comparison to NF. Interestingly, the cell width is reduced to nearly 3 mm at $t = 0.15$ ms as shown in Fig. 5.12. At lower N, such as in case Y1, this does not occur. Although joule dissipation continues to occur, the detonation front adjusts to a steady value as the kinetics become rate-limited by radical production. Thus, at $t = 0.16$ ms the cell width remains at approximately 3 mm. Since the magnetic field modifies the observed detonation cell-width, and this change is related through N, estimation of the electrical conductivity of the gaseous mixture is possible from observations of the cellular structure in a give magnetic field.

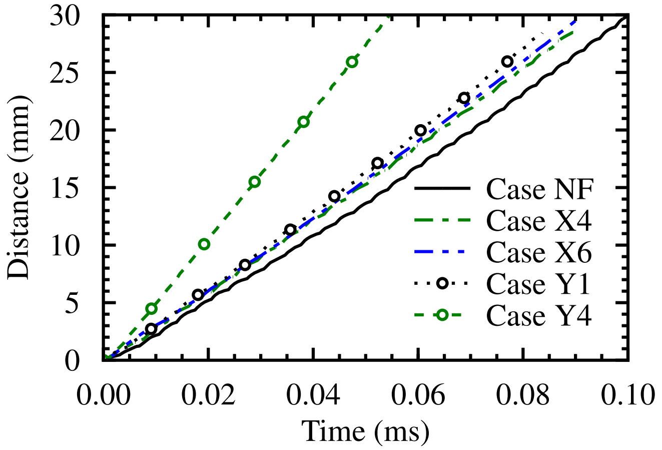

Figure 5.13: The average location of the detonation front as a function of time for the cases given in Table 5.1

The heat addition by the magnetic field also affects the detonation velocity. Since the Joule dissipation is proportional to B_0^2, and thus N, the effect of heating on detonation is more profound in case Y4 than in case Y1. Thus, the deviation in the detonation velocity (see Fig. 5.13) increases with N. Even in case Y1, the detonation velocity is marginally augmented in comparision to case NF. Note that,for both case Y1 and Y4, the Lorentz force is in the direction opposite of the detonation propagation. The momentum deficit, however, is negligible in comparison to the subsequent expansion occurring from heat addition. This is due to the application of the field in the direction perpendicular to the direction of the dominant velocity component (in x-direction).

5.3.2 Effect of $B_{x,0}$

When the magnetic field is applied in the x-direction, the detonation velocity increases slightly, but this increase is independent of N as shown in Fig. 5.13. The current density, and likewise the electromotive force, is proportional to the component of the velocity perpendicular to the magnetic field, in this case, the transverse velocity. Similar to case Y1 and Y4, Joule dissipation results in reduction of $L_{1/2}$ at lower N as shown in Fig. 5.14.

For simulations with an applied $B_{x,0}$, however, the Lorentz force counters the movement of transverse waves in the post-detonation flow since their motion is perpendicular to $B_{x,0}$. This introduces new dynamics. At higher values of N, the transverse waves are actively suppressed. This suppression reduces the strength of the transverse wave interaction with the Mach stem and incident shock at the detonation front, and over time the front becomes relatively flat. The formation of the characteristic cellular structures are thus eliminated (see Fig. 5.15). This results in a reduction in the $L_{1/2}$ in the cases Y4-Y8. The combined effect of heat addition via Joule dissipation and transverse wave suppression, which disables the high temperature triple point formation [30], results in only a marginal increase in the detonation velocity for any given N. For the times simulated here, and for the values of N investigated, the reaction front does not decouple from the shock wave. This was determined by switching off the magnetic field after some time. For any given N, the typical cellular structures are regenerated by turning off the applied field.

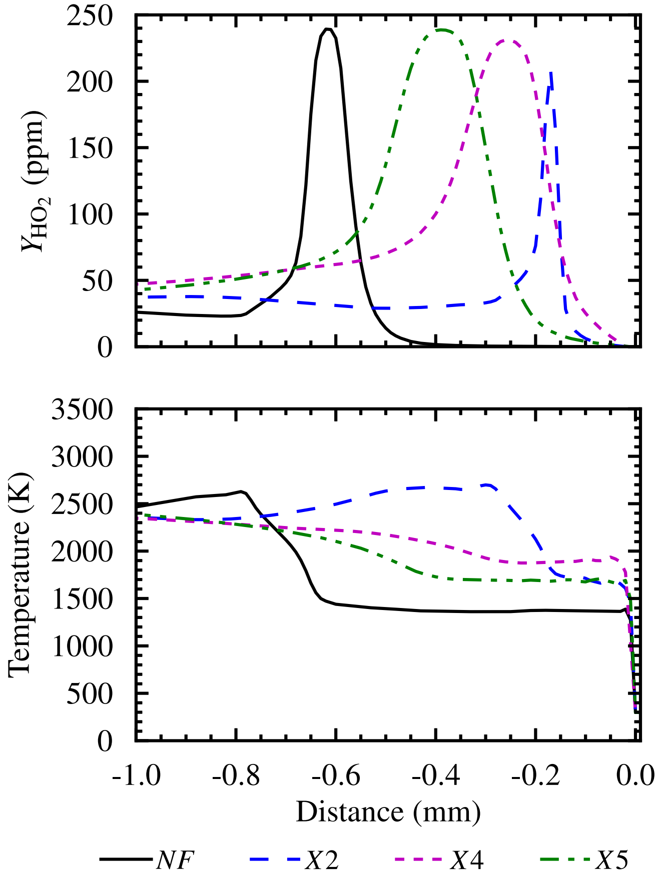

Figure 5.14: Profiles of the HO_2 mass fraction and temperature for cases NF, X2, X4, and X5 corresponding to the center of the Mach stem for each detonation front at approximately 0.175 ms.

To summarize, the magnetic field applied in the direction of detonation propagation affects the detonation through a combined effect of Joule heating and Lorentz force. While the Lorentz force acts to eliminate transverse waves and cellular structure, the heating effect resulted in temperature increase and sustained coupling of reaction zone with the shock propagation. Thus, for any given N, the change in detonation velocity is marginal. Due to the difference in the magnitude of velocity components in x- and y -directions, $B_{0,x}$ affected the detonation both by momentum and energy coupling where as the dominant effect of $B_{0,y}$ is Joule dissipation.

5.3.3 Conclusions

Using numerical simulations, the propagation of a detonation wave in the presence of an applied magnetic field is investigated. From experimental measurements and previous numerical studies of ionizing detonations using detailed kinetics, a range of electrical conductivities are estimated and used in this study. These measurements indicate that the magnetic Reynolds number of a typical gaseous detonation are much less than one. Leveraging this knowledge, simulations are performed using the quasi-static assumption. In the limit of small magnetic Reynolds number, the interaction parameter becomes the governing non-dimensional number. In this study, the interaction parameter is varied as well as the magnetic field orientation in order to investigate how the field may affect the propagation and stability of the detonation. For transverse fields of large N, the cellular structure of the detonation is affected resulting in cell-widths half the size of those observed in detonations with no applied magnetic field. The reduction in the half-reaction distance consequently results in an increase in the detonation velocity. For magnetic fields in the direction of the detonation propagation, an increase in detonation velocity is also observed, but at high N, the transverse waves are adversely affected. The suppression of the transverse waves results in the elimination of the detonation structure. Turning off the magnetic field results in the regeneration of cellular structures.

5.4 Richtmyer-Meshkov Instability

The Richtmyer-Meshkov instability (RMI) develops when a shock wave accelerates an initially perturbed interface between two fluids of different properties. During shock refraction, a misalignment between the density and pressure gradients causes vorticity generation by baroclinic torque along the interface. This unstable vortex sheet drives the amplification of the initial perturbations which can be characterized either by a sinusoidal function of a given wavelength and amplitude (i.e., single-mode RMI) or a superposition of these perturbations (i.e., multi-mode RMI) [63]. Additional instabilities, such as the Kelvin-Helmholtz instability, result in vortex roll-up and an increase in the growth of the mixing layer. Furthermore, possible secondary shocks impacting the evolving mixing layer can substantially amplify the mixing processes [64] and quicken the transition of the layer to a fully turbulent mixing zone.

RMI is a fundamental fluid instability ubiquitous in both nature and engineering. Thus it is the topic of much experimental, analytical, and computational study [63]. The first of such analysis was by Richtmyer [65], who treated the RMI as the impulsive limit of the Rayleigh-Taylor instability and was able to show that the interface amplitude grows linearly in time. Experiments [66, 67, 68] show good agreement with the impulsive formulation; however, as the interface amplitude increases to roughly a tenth of the perturbation wavelength [63],

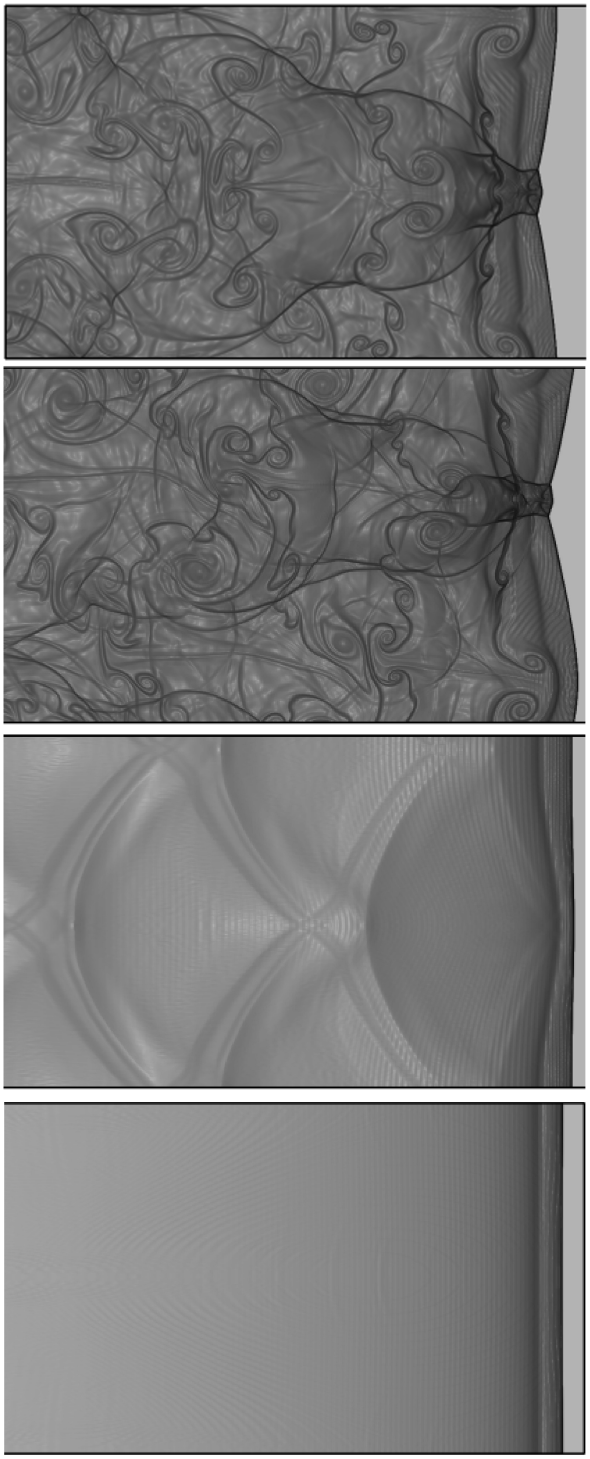

Figure 5.15: Plot of $\ln(|\nabla\rho| + 1)$ for cases NF, X2, X4, and X5 (top to bottom) shown in Table 5.1 showing the detonation front and the post-detonation flow structures at $t = 0.175$ ms.

the RMI transitions to non-linear growth, and the linear theory is no longer valid. This phase of the instability is often described as having "bubbles" rising into the heavier fluid and "spikes" falling into the lighter fluid. Several non-linear models have been developed to predict the bubble/spike velocities and the subsequent reduction in growth of the interface width from mode saturation [69, 6, 70]. Such models show good agreement to two- and three-dimensional numerical simulations [64].

In realistic applications, however, the initial interface is more accurately quantified as a superposition of perturbations spanning a large range of amplitudes and wavelengths. In this case, the RMI quickly transitions to non-linear growth following a self-similar power-law dependence with time, $h \approx t^{\theta}$, where h is the peak-to-valley amplitude with values of θ ranging from 0.2 to 1.0. The exact value of θ is an on-going topic of discussion [63, 71, 72]. Assuming the just-saturated mode dominates the mixing dynamics, Dimonte *et al.* [73] determine the overall growth of the mixing layer to have a growth exponential of $\theta \approx 0.5$. Modifications to include the effects of initial conditions, however, show that the growth from mode-coupling alone results in $\theta = 0.24$, concluding that any measured growth-rate larger than that must be dependent on the initial conditions [74]. Recent experiments [75, 76, 77] and other analytical models [78, 79, 80] show similar discrepancies complicating the understanding of the driving factors in the RMI growth-rate. In addition, several computational studies have attempted to better understand how the RMI growth-rate depends on a number of factors including the initial multi-mode perturbations [74], the impulse strength [67, 81, 82], and the fluid composition [83].

Re-shock RMI occurs when a second shock perturbs the already evolving interface. All experiments indicate that this second impulse results in a significant increase in the mixing layer growth-rate [84, 85, 1, 72]. Yet, once again there is some discrepancy in determining functional relationship of the re-shocked RMI growth-rate. In the experiments by Leinov *et al.* [85] and Vetter and Sturtevant [1], the re-shock growth is observed to be linear in time ($\theta = 1$) and is proportional to the velocity jump at the re-shock interface. This is consistent with theoretical predictions [86, 72, 87], numerical parametric studies [64], and several computational studies [88, 89, 90] of the experiments by Vetter and Sturtevant[1], all of which show a linear growth-rate after re-shock. Only at very late times is there an indication of mode saturation and non-linear growth. Yet, experiments by Houas and Chemouni [91] show a growth exponential somewhere between $\theta = 2/3$ and $\theta = 1.0$, and in the gas-curtain experiments of Balakumar *et al.* [84] and the corresponding computational simulations of Gowardhan and Grinstein [92], the re-shock growth is much more non-linear. Thornber *et al.* [93] have proposed to reconcile these differences by modifying the linear model of Mikaelian[94] to depend on the molecular mixing fraction. An extension of this model to two-phase flows is discussed in this work.

5.4.1 Verification and Validation

Since many past numerical simulations [88, 89, 90] show a reasonably good comparison to data measured in the air / SF_6 (single-phase) re-shock RMI experiments of Vetter and Strutevant [1], a similar configuration is adopted here to act as a reference point for the two-phase studies. The experiments were conducted in a shock-tube with cross-sectional dimensions of $L_y \times L_z$, and a variable longitudinal length of L_x. The air / SF_6 mixture is initially separated

Table 5.2: Test conditions and measurements of the re-shocked RMI experiments of Vetter and Sturtevant[1] where VS0-VI and VS0-VII correspond to experiments VI^b and VII^b.

	VS0-VI	VS0-VII
Incident Mach number:	1.5	1.98
Pressure (kPa):	23.0	8.0
Distance from interface to wall, L_x (m):	0.62	0.49
Instantaneous velocity, ΔV (m/s):	150.0	287.0
Shocked growth-rate (m/s):	4.2	7.5
Re-shocked observation time (m/s):	37.2	74.4
Shocked observation time (ms):	2.2–3.2	1.7–2.5
Re-shocked observation time (ms):	4.0–5.5	1.7–2.5

by a thin membrane supported by a wire mesh of 1 cm spacing. As the initial shock speed is varied from Mach 1.18 to 1.98, the length of the test section is adjusted from 61 cm to 122 cm to ensure the re-shocked mixing zone is within the observational test-section. High resolution spark-Schlieren images and high-speed cameras were used to obtain data about the mixing zone flow features and growth-rates. For the validation study, two experimental configurations are simulated, denoted as VS0-VI and VS0-VII, which correspond to case VI^b and case VII^b of Vetter and Sturtevant [1]. Only the gas-phase initialization of case VS0-VI is used for the multi-phase studies presented later. The reference conditions for these cases are summarized in Table 5.2, and a schematic of the simulation domain is given in Fig. 5.16.

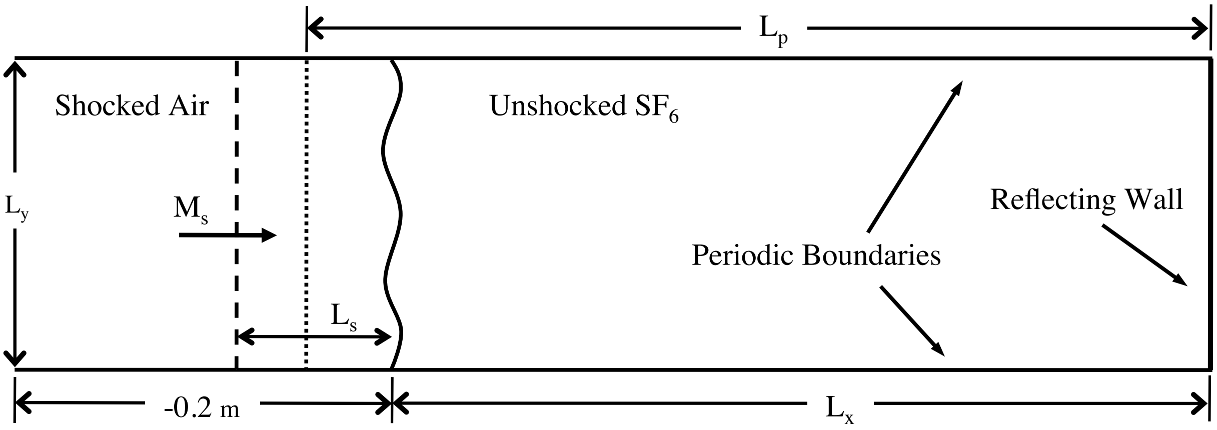

Figure 5.16: Schematic of the simulation domain where M_s is the Mach number of the shock, L_x is the distance from the end wall to the contact, and L_s is the distance from the contact to the initial shock position. For the multi-phase simulations, L_p is the length of the initial particle cloud.

The experiments were designed to avoid boundary layer interaction with the mixing layer. Thus, the side-walls of the shock tube (in y- and z-direction) can safely be treated numerically

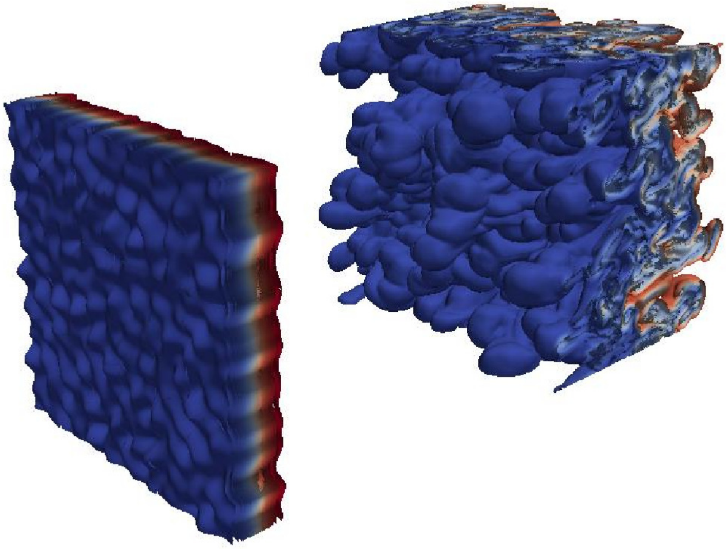

Figure 5.17: Mixing zone before (left) and after (right) re-shock for Case RMI1.

as periodic boundaries, an assumption also made in prior numerical studies [88, 89, 90]. The end wall ($x = L_x$) is modeled as a no-slip boundary, and the inflow boundary at x = -0.2 m is initially modeled as a supersonic inflow boundary, but to allow the exit of the reflected and transmitted waves later in the simulation, the boundary is changed to a non-reflecting characteristic outflow boundary later in the simulation. This prohibits the non-physical reflection of waves from the boundary, which could corrupt the mixing-layer growth at late times.

The development of the RMI is highly sensitive to the initial structure of the interface separating the light (air) and heavy (SF_6) species [90]. In the current study, the interface is formed by specifying the SF_6 mass fraction, $\mathrm{Y}_{\mathrm{SF}_6}$, with an initial hyperbolic tangent profile [83] centered at $x = 0.0$ m and a characteristic thickness of δ given by

$$Y_{\mathrm{SF}_6}(x, y, z; 0) = \frac{1}{2} - \frac{1}{2}\tanh\left(\frac{x - \eta_I(y, z)}{\delta}\right), \tag{5.2}$$

where $\eta_I(y, z)$ is the interface perturbation. Following previous numerical simulations [88, 89, 90], an "egg-carton" sinusoidal perturbation for $\eta_I(y, z)$ is used to model the wire-meshed membrane separating the air and SF_6 gases in the experiments and is described by the expression

$$\eta_I(y, z) = a_0|\sin(k_0 y)\sin(k_0 z)| + a_1\cos(k_1 y)\cos(k_1 z) + a_2\Psi(y, z), \tag{5.3}$$

where the first term represents the small-scale perturbations resulting from the wire-mesh, and the second term represents the scales associated with the transverse dimensions of the shock tube. The last term includes random perturbations, which are used to account for small-scale irregularities and to break the symmetry of the initial conditions and accelerate

Table 5.3: Summary of the simulation configurations used in the re-shock validation experiment (VS) and the multi-mode (MM) and single-mode (SM) numerical simulations. The function $\mathcal{U}_r$ represents a uniform random variable chosen on the interval [0,1], $k_0 = 2\pi/L_y$, and Δx is the grid resolution used for each case. All dimensional values are given in units of centimeters.

Case Name	$\eta_I(y,z)$	$\Psi(y,z)$	a_0	a_1	a_2	$k_0\eta_0$	L_y, L_z	L_p	L_s	Δx
VS	Eq. 5.3	Eq. 5.4	0.25	0.125	0.125	0.00926	27.0	–	5.0	0.105
MM	Eq. 5.3	Eq. 5.4	0.25	0.125	0.125	0.0185	13.5	65.0	5.0	0.105
SM	Eq. 5.6	–	0.25	0.0	0.0	0.0185	13.5	65.0	5.0	0.105
SMR	Eq. 5.6	$\mathcal{U}_r$	0.25	0.0	0.2	0.0185	13.5	65.0	5.0	0.105
SMN	Eq. 5.6	–	2.5	0.0	0.0	0.185	13.5	65.0	5.0	0.105

the transition of the RMI to non-linear growth. The values of the coefficients used in the current study are $a_0 = a_1 = 1.25 \times 10^{-3}$ m and $a_2 = 2.5 \times 10^{-4}$ m with the random initial small-scale perturbations, $\Psi(y,z)$, prescribed by an adapted von Karman power spectrum [90],

$$E_\Psi(k) = k^{-2}\left[\frac{kL}{\sqrt{(kL)^2 + B}}\right]^4, \tag{5.4}$$

where $L = 0.95$ cm, $B = 5\sqrt{2}$ and $k = \sqrt{k_y^2 + k_z^2}$ where $k_y = 2\pi/L_y$ and $k_z = 2\pi/L_z$. The random fluctuations, $\Psi(y,z)$, were normalized such that they have a root-mean-square amplitude of one with the amplitude is set by a_2. These values as well as the simulation configuration parameters are summarized in Table 5.3.

Figure 5.18a shows the time evolution of the mixing length, $\eta(t)$, compared to the experimental growth-rate data for the two re-shock configurations defined in Table 5.2. In practice, there are many ways to define the width of the mixing zone. In this study, an integral definition is adopted where the mixing length is given by

$$\eta(t) = 4\int_{-0.2}^{L_x} \langle Y_{\mathrm{SF}_6}\rangle \left(1.0 - \langle Y_{\mathrm{SF}_6}\rangle\right) \mathrm{d}x. \tag{5.5}$$

The quantity $\langle\cdot\rangle$ represents a volumetric average in the transverse directions over the distances L_y and L_z, and is a function of only the time, t, and x, the longitudinal direction.

For a single-mode initial perturbation, the mixing length growth is approximately linear following the theoretical estimation given by Richtmyer's impulsive model [65], $\dot{\eta} = v_0 = k_0\eta_0 A^+ \Delta V$. In this equation, η_0 is the initial amplitude [$= a_0$], A^+ is the post-shock Atwood number [$= (\rho_{\mathrm{SF}_6} - \rho_{\mathrm{Air}})/(\rho_{\mathrm{SF}_6} + \rho_{\mathrm{Air}})$], and ΔV is the velocity jump at the contact discontinuity. The initial perturbation is given by

$$\eta_I(y,z) = \frac{a_0}{2}\Big(\sin(k_0 y) + \sin(k_0 z)\Big) + a_2\Psi(y,z), \tag{5.6}$$

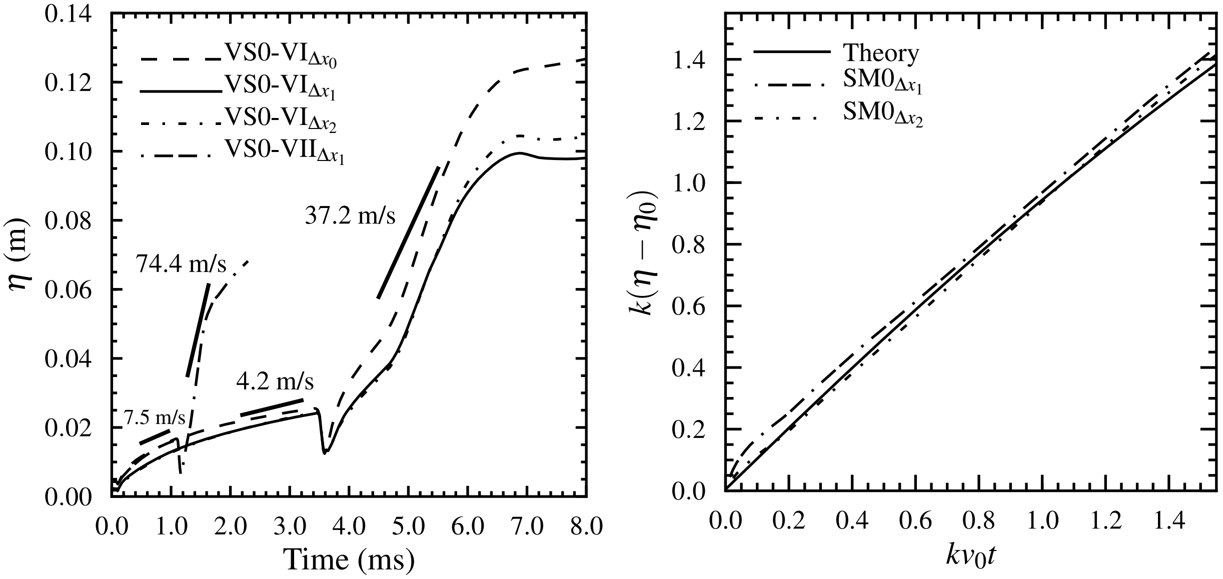

(a) (b)

Figure 5.18: (a) Evolution of the mixing layer $\eta(t)$ at three different grid resolutions (Δx_0 = 0.21 cm, Δx_1 = 0.105 cm, Δx_2 = 0.07 cm) with comparison to the experimental measurements summarized in Table 5.2. (b) Time history of the normalized mixing length in single-mode RMI at the same grid resolutions (Δx_1, Δx_2) with a comparison to the non-linear theory of Sadot *et al.* [6].

with the values of a_0 and a_2 given in Table 5.3 and the configuration summarized in Table 5.4. The evolution of the normalized mixing length for the single-mode (SM) RMI is shown in Fig. 5.18b. Even under these conditions, however, the RMI transitions to non-linearity and is more appropriately described by the model of Sadot *et al.* [6] also shown in Fig. 5.18b.

For case VS0-VI at $t = 3.46$ ms, re-shock occurs. This results in a compression of the mixing zone, noticeable by the reduction in the mixing length, followed by a subsequent increase in the mixing length as the reflected shock further amplifies the perturbations in developing mixing zone. This tends to hasten the production of small-scale structures prompting the development of an inertial sub-range [81, 84].

The results in Fig. 5.18 are given for three different grid resolutions: $\Delta x_0 = 0.21$ cm, $\Delta x_1 = 0.105$ cm, and $\Delta x_2 = 0.07$ cm. For the two highest resolutions, the RMI growth-rates are indistinguishable with only small differences in the final saturated mixing length and thus serving as a reasonable demonstration of grid convergence. A grid resolution of $\Delta x = \Delta x_1 = 0.105$ cm, which was used in previous studies [89], is chosen for the rest of the studies resulting in a computational grid of 780 × 256 × 256. The numerical results show good agreement to the experimental measurements of the RMI growth-rates before and after re-shock, and in the case of the single-mode simulations, to the analytical models of the RMI growth-rate prior to re-shock. These results lend confidence to the numerical methodology, simulation configuration, and initialization used in this study.

Table 5.4: Summary of the multi-phase initial conditions used in the numerical simulations. Simulations are referred to by the case name (i.e., SM, MM, etc.) defined in Table 5.3 and the case number defined below. For reference, this table additionally provides the RMI growth-rate data for the SM cases.

Case No.	α_0	r_p (μm)	N_0	$\mathcal{P}$	SM St	SM ΔV (m/s)	SM A$^+$	SM A$_m^+$
0	0.0	–	–	–	–	147.9	0.781	–
1	2.0×10^{-5}	30	2094876	3	1.11	146.4	0.725	0.689
2	2.0×10^{-5}	60	261859	1	3.21	146.5	0.725	0.689
3	2.0×10^{-5}	120	32732	1	9.98	146.3	0.725	0.689
4	4.0×10^{-5}	5	904986837	1300	0.09	135.7	0.709	0.641
5	4.0×10^{-5}	10	113123354	170	0.23	137.6	0.717	0.649
6	4.0×10^{-5}	30	4189753	6	1.11	142.7	0.724	0.656
7	4.0×10^{-5}	60	523719	1	3.22	145.5	0.725	0.657
8	4.0×10^{-5}	120	65464	1	9.98	146.2	0.725	0.657
9	1.0×10^{-4}	30	10474384	15	1.11	142.2	0.719	0.572
10	1.0×10^{-4}	60	1309298	2	3.21	142.7	0.724	0.576
11	1.0×10^{-4}	120	163662	1	9.98	143.7	0.724	0.576
12	2.0×10^{-4}	30	20948769	30	1.11	141.6	0.716	0.470
13	2.0×10^{-4}	60	2618596	4	3.21	142.5	0.720	0.475
14	2.0×10^{-4}	120	327324	1	9.98	142.9	0.724	0.478

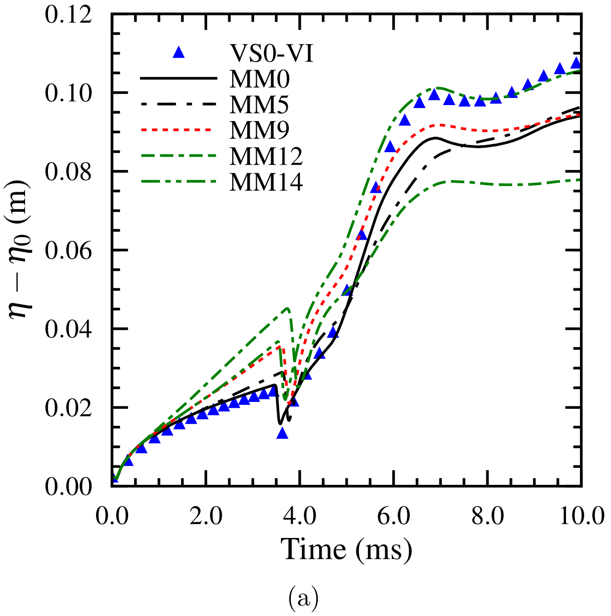

Figure 5.19: Time evolution of (a) the mixing layer width, $\eta(t)$, and (b) the mixing fraction, $\Theta(t)$, for the multi-mode RMI in a dilute gas-particle mixture compared to the single-phase results of VS0-VI and MM0.

5.4.2 RMI in Dispersed Phase Flows

As summarized above, much of the focus on RMI has been on the development of the instability in single-phase media within the parameter space encompassing three parameters: the scales and type of initial perturbations, the impulse strength, and the fluid composition. In many applications, such as in chemical explosions with burning metal particles [95] or in astrophysical dusty plasmas [96], the instability develops in a highly complex multi-phase environment. Earlier studies [32, 97] have addressed some of these aspects using numerical simulations. For example, Balakrishnan and Menon[97] have proposed a multi-phase buoyancy-drag model for both the RMI and the RTI by extending the work of Srebro[98] to dilute gas-particle mixtures. Using this model, the authors calculate the RMI growth-rate for both single-mode and multi-mode initial perturbations and show a reduction in the RMI growth for increases in the mass loading. The model has certain limitations, however, such as the assumption that the particles are always in equilibrium with the gas. Thus, the momentum and energy coupling between the two phases is neglected. This assumption is relaxed in this study.

Also in a previous study, Ukai *et al.* [32] derive a linear impulsive model for the growth-rate of the single-mode RMI in a dilute gas under the assumption of small Stokes number, St, which is defined as the ratio of the time scale of the flow (τ) to that of the particle field (τ_p). In the range of the model's validity, the model compares reasonably well to two-dimensional numerical simulations showing a similar dependence on mass loading as predicted by the buoyancy-drag model of Balakrishnan and Menon [97]. For St > 0.01, however, the model is less accurate in comparison with the numerical simulations where the simulation results seem to indicate a reversal in trend, i.e., high mass loadings resulting in larger growth-rates. A possible reason for this reversal in trend is explained in this work. Moreover, since impulsive models are only valid within the linear growth regime of the RMI and thus only applicable to small amplitude single-mode perturbations during early times, prior work leaves it unclear how the presence of particles might affect the non-linear processes of the RMI, particularly since after re-shock such processes accelerate mixing. More importantly, both the linear impulsive model and the buoyancy-drag model implicitly assume the gas-particle mixture is in equilibrium, and thus they cannot account for any coupling between the phases. The three-dimensional numerical simulations discussed in the current work seek to explain in a more rigorous manner how the RMI evolves in a two-phase flow before and after re-shock. To do this, studies based on prior single-phase re-shock RMI simulations [64, 88, 89, 90] are used to extend the previous analysis of two-dimensional single-mode RMI in dilute-gas mixtures [32, 97]. By analyzing a wide range of initial Stokes numbers and particle number densities, a previously unobserved increase in the initial two-phase RMI growth-rate is explained. Additionally, a new model for the re-shock RMI growth-rate in a dilute gas-particle mixture is introduced that correlates well with the numerical predictions.

For the two-phase simulations, a uniform region of spherical particles with a radius of r_p spanning the cross-sectional area of $L_y \times L_z$ and the length L_p is superimposed onto the single-mode (SM) and multi-mode (MM) configurations discussed in the previous section and shown schematically in Fig. 5.16. From theoretical analysis [32, 97], two parameters are used to characterize the dynamics of the RMI in a dilute gas-particle mixture, the mass loading (f) and the Stokes number (St). The mass loading is defined as the ratio of the particle mass per volume to the gas density ($f = mn_0/\rho$, where n_0 is the number of particles per volume, m is the particle mass, and ρ is the fluid density). From this, a multi-phase Atwood number can be defined as [32]

$$A_m = \frac{\rho_2\,(1 + f_2) - \rho_1\,(1 + f_1)}{\rho_2\,(1 + f_2) + \rho_1\,(1 + f_1)}, \tag{5.7}$$

where the subscripts 1 and 2 refer respectively to the light (air) and the heavy (SF_6) gases separated by the contact discontinuity. If no particles are present ($f_1 = f_2 = 0$), as in case SM0, then A_m reduces to A. Also, note that for $A > 0$ and uniform particle loading across the contact discontinuity, A_m is always less than A. By linearizing the dilute gas-particle equations, it is possible to derive a multi-phase impulsive theory [32], which results in the following linear equation for the mixing length as a function of time:

$$\eta(t) = \eta_0(1.0 + k_0 A_m \Delta V t) = \eta_0 + v_{0,m} t. \tag{5.8}$$

The result is that A_m simply replaces A where the use of A_m accounts for the reduction in the effective impulse strength resulting from the particle mass loading of the flow. This theory, however, is derived in the limit of vanishing Stokes number, and thus is only applicable for St $<<$ 1.0 flows. The Stokes number is computed as $\tau_p/\tau_{RMI} = kA\Delta V \tau_p$, where the time-scale of the particles is $\tau_p = (1/4)\pi r_p \rho_p C_D \mu$. For the SM cases, τ_{RMI} is approximately 2.4 ms. In this study, the particles are chosen to have the properties of steel, such that $\rho_p = 7800$ kg/m^3. Therefore, given the same gas-phase conditions, St is a strong function of the particle radius.

Using these multiphase parameters, A_m and St, a parameter study is conducted to study the RMI in a dilute gas-particle mixture. The gas-phase reference conditions ($M_s = 1.5$,

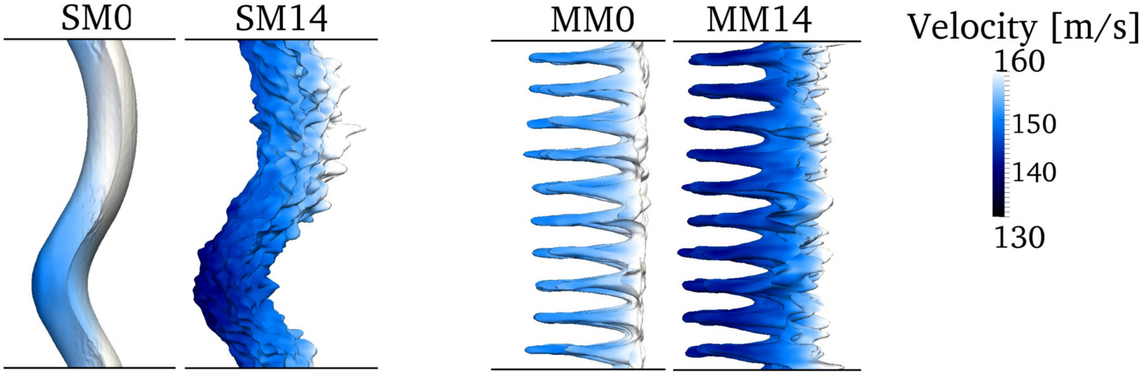

Figure 5.20: Contours of the species mass fraction, $Y_{SF_6} = Y_{Air} = 0.5$ for the single-phase cases SM0 and MM0 compared to representative multi-phase cases SM14 and MM14 colored by the velocity in the x-direction.

$p_0 = 23$ kPa, $T_0 = 298.15$ K) of case VS0-VI from Table 5.2 are kept constant (for reasons explained in Section 5.4.1), while the size (r_p) and the number of particles (N_0) within the domain are varied independently. The multi-phase conditions discussed in this study are summarized in Table 5.4. The values of r_p and N_0 considered in this study are limited by the dilute assumption, i.e., dispersed-phase volume fractions, α, less than 1 percent. While the simulations presented here are only a portion of the possible conditions, additional simulations indicate that the conclusions drawn from the data reported here apply over a much larger range within the limits of the numerical formulation. Furthermore, as will be discussed in more detail later, the particle cloud compresses throughout the simulation which limits the initial value of α_0. Henceforth, these numerical experiments are referred to by the case name (i.e., SM, MM, etc.) defined in Table 5.3 and the case number (i.e., 0, 1, 2, etc.) defined in Table 5.4. The former defines the initial configuration and perturbation interface, while the later defines multi-phase parameters. For example, case MM0 refers to a multi-mode, single-phase simulation.

Also given in Table 5.4 is the number of particles per parcel, $\mathcal{P}$, used in each case as well as the initial volume fraction α_0, which is defined as the ratio of the total volume occupied by the particles, $V_p = N_0(4/3)\pi r_p^3$, to the volume $V = L_y L_z L_p$, where L_p is the distance from the end-wall in the x-direction occupied by the particles (see Fig. 5.16). In this study, $L_p = 65.0$ cm is kept constant.

There are noticeable differences in the time evolution of the RMI in multi-phase flows. Figure 5.19 shows the time history of the mixing length, $\eta(t)$, and mixing fraction, $\Theta(t)$, of two representative multi-phase cases, MM12 and MM14, compared to results from the single-phase simulation MM0. The molecular mixing fraction, Θ, is defined as

$$\Theta(t) = \frac{\int \langle Y_{\mathrm{SF}_6} Y_{\mathrm{air}} \rangle \mathrm{d}x}{\int \langle Y_{\mathrm{SF}_6} \rangle \langle Y_{\mathrm{air}} \rangle \mathrm{d}x}. \tag{5.9}$$

It is a more useful description of how well-mixed the two species are in the mixing zone since the span-wise averaged mass fraction carries no distinction between regions that are completely mixed and those regions that are unmixed, but contain equal portions of species.

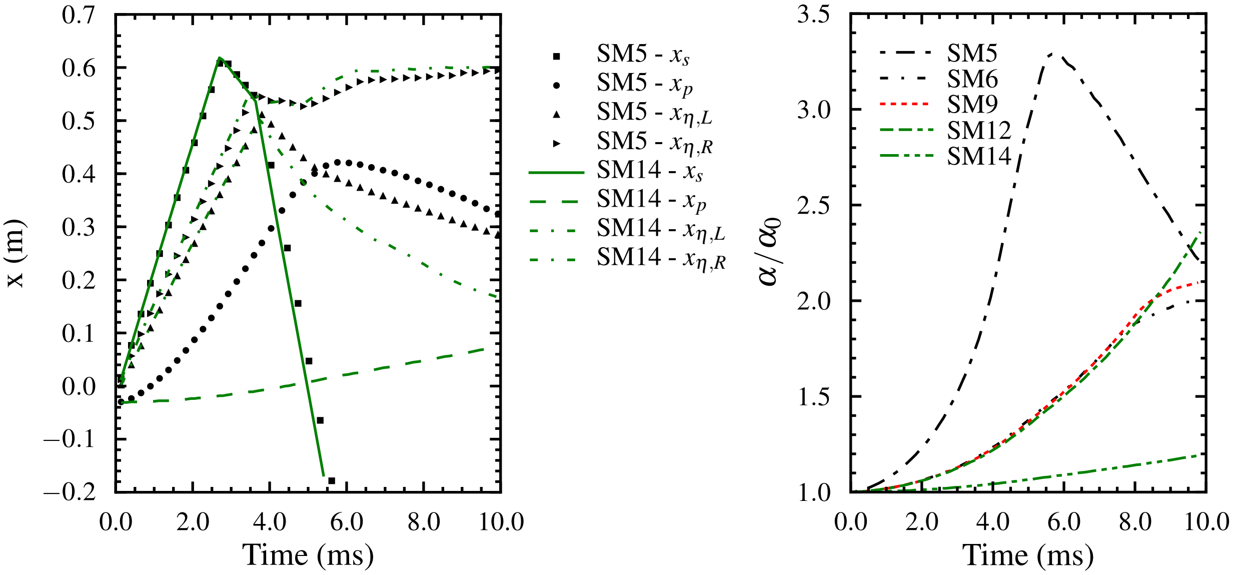

(a)

(b)

Figure 5.21: (a) Time evolution of the ratio of the particle cloud volume fraction, α, to the initial volume fraction, α_0. (b) x-t diagram of the time history of the shock location, x_s, the left interface of the particle cloud, x_p, and the left (spike) and right (bubble) interfaces of the mixing zone, $x_{\eta,L}$ and $x_{\eta,R}$, respectively.

Thus, Θ quantifies the relative amount of molecularly mixed fluid within the mixing layer, such that $\Theta = 1.0$ would mean that the entrained fluids were completely mixed within each transverse plane.

For $\alpha_0 > 1.0 \times 10^{-4}$, there is a noticeable increase in the growth-rate of the multiphase RMI before re-shock as well as a corresponding decrease in the molecular mixing fraction meaning that the rate of entrainment is increased. A comparison of the mass fraction contours colored by the x-velocity at $t = 3.0$ ms in Fig. 5.20 shows that the presence of particles in flow effectively increases the size and distortion of the mixing interface, while decreasing its convective velocity. The location of the mixing zone can be identified by using a threshold value of the species mass fraction. Thus, the left (spike) and right (bubble) interfaces are defined by $x_{\eta,L} = x|_{Y_{\mathrm{SF}_6}=0.01}$ and $x_{\eta,R} = x|_{Y_{\mathrm{SF}_6}=0.99}$. Further, the particle cloud is defined between x_p, the position of the left-most particle, and the end-wall at 0.62 m.

The x-t diagram, shown in Fig. 5.21a, shows the location of the shock in relation to the mixing zone and the particle cloud. For small St, the particle cloud is significantly compressed and interacts with the mixing zone after re-shock. The compression of the particle cloud is further indicated by the ratio of the volume fraction to the initial volume fraction, α/α_0. Thus for low St, the mass loading increases throughout the simulation. Note that the volume fraction still remains within dilute limit. This results in a reduction in the mixing zone length at late-times; however, the molecular mixing fraction for all cases asymptote to values between 0.84-0.88.

RMI develops as a result of vorticity deposited along the interface by the production of baroclinic torque. This process can be investigated using the compressible vorticity transport equation, given by Eq. 5.10, which is derived by taking the curl of the momentum conservation equation. The tensor form of this equation is given as

$$\begin{aligned}\frac{D\omega_i}{Dt} &= \omega_j \frac{\partial u_i}{\partial x_j} - \omega_i \frac{\partial u_j}{\partial x_j} + \epsilon_{ijk} \frac{\partial}{\partial x_j}\left(\frac{1}{\rho}\frac{\partial \tau_{km}}{\partial x_m}\right) + \frac{1}{\rho^2}\epsilon_{ijk}\frac{\partial \rho}{\partial x_j}\frac{\partial p}{\partial x_k} + \epsilon_{ijk}\frac{\partial}{\partial x_j}\left(\frac{\dot{F}_{p,k}}{\rho}\right) \\ &= \Omega_i^s + \Omega_i^d + \Gamma_i + \beta_i + \Pi_i.\end{aligned} \tag{5.10}$$

The first two terms in this equation, Ω_i^s and Ω_i^d, represent the transport of vorticity through vortex stretching and dilatation. The third term, Γ_i, represents the production of vorticity by viscous stresses, while the fourth term, β_i, represents the production/destruction of vorticity by baroclinic torque. In addition to these terms, an additional vorticity production occurs in multi-phase flows resulting from the inter-phase momentum coupling term, $\dot{F}_{p,k}$, which is represented by the term, Π_i. The viscous contribution to vorticity dissipation is ignored here.

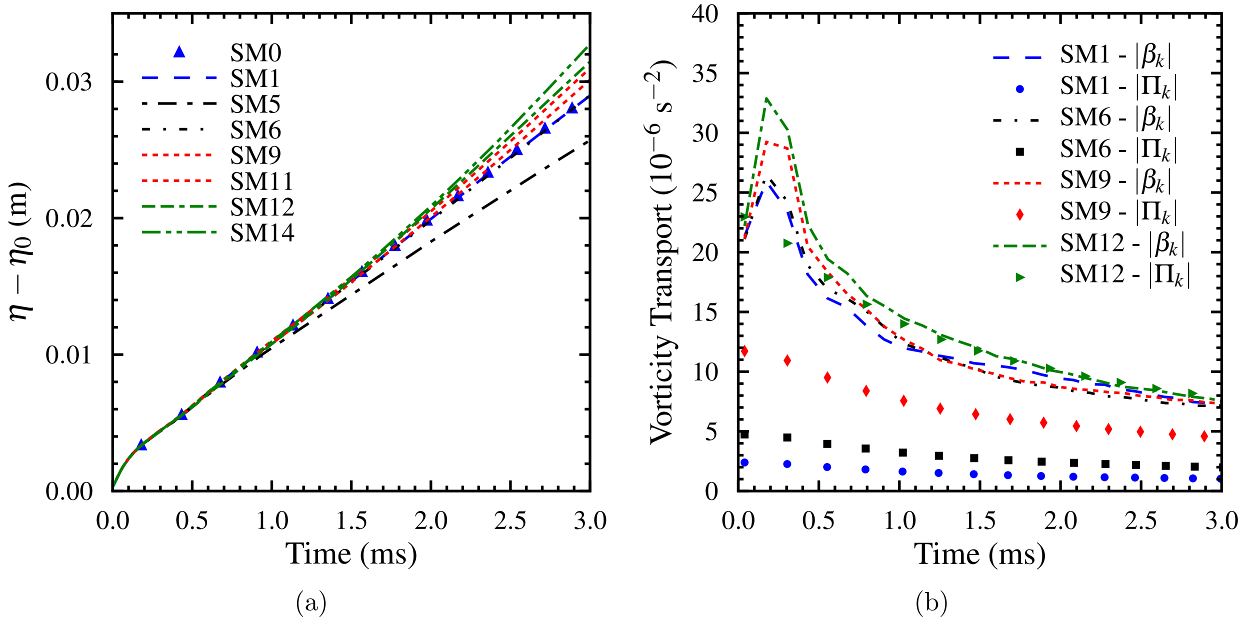

Figure 5.22: (a) Evolution of the mixing layer width, $\eta(t)$, at different α_0 and St. (b) The vorticity transport budget during the initial growth of the RMI for cases with the same r_p where $|\Pi_k(t)|$ and $|\beta_k(t)|$ are the magnitude of the vorticity production due to the particle acceleration term and the baroclinic torque volume-averaged over the mixing zone.

For St < 1, cases SM4 and SM5, Fig. 5.22a shows that the width of the mixing-layer is reduced by approximately 11 percent. This reduction is predicted by the linear impulsive model of Ukai *et al.*, given by Eq. 5.8, where $\dot{\eta}_{\text{num}}/\dot{\eta}_{\text{model}} = 0.96$. For the cases where St > 1, however, the mixing-layer growth rate increases with the increase proportional to the mass loading (larger r_p and larger α_0). For cases SM12 and SM14, there is a 7.3 and 10.8 percent increase, respectively, while for cases SM9 and SM11, there is only a 3.0 and 5.7

percent increase, respectively. To ensure that this observation is a direct result of the gas-particle interaction, a case without particles, but with a random multi-mode initialization, case SMR0 (not shown), is also simulated and shows no observable change in the mixing layer from case SM0. Therefore, the increase in the multi-phase RMI mixing length is a result of the continued presence of the particles within the flow. A possible explanation for this is the presence of an additional vorticity production term in Eq. 5.10, which is non-zero as a result of the differential gas-particle velocities. Figure 5.22b shows the time evolution of the magnitude of the vorticity production contributions from the baroclinic torque, $|\beta_i(t)|$, and the interphase particle term, $|\Pi_i(t)|$, volume averaged over the mixing layer, defined as extending between $x_{\eta,L}$ and $x_{\eta,R}$ in the longitudinal direction and L_y and L_z in the transverse directions. For simulations where the particle vorticity production is much less than the vorticity production by baroclinic torque ($|\beta_i(t)| >> |\Pi_i(t)|$), there is a correspondingly little or no increase in the mixing-layer growth rate. However, when the two terms are of similar magnitude, the mixing-layer growth-rate increases as a result of this additional vorticity production. For example, the magnitude of the span-wise volume averaged vorticity, $|\omega_i(t)|$, at $t = 2.5$ ms for case SM14 is 38.7 s^{-2} compared to 20.6 s^{-2} for case SM0.

By increasing $k_0\eta_0$, the initial misalignment of the pressure and the density at the interface increases the baroclinic torque production and therefore, the relative difference between $|\Pi_i(t)|$ and $|\beta_i(t)|$, is altered. Though not shown here, this trend is observed by comparing the deviations of cases SMN12-14 and SM12-14 from the single-phase cases SMN0 and SM0, respectively. The mixing zone width at $t = 3.0$ ms for case SMN12 is slightly reduced by 1.78 percent compared to case SMN0 ($\eta_{SMN12} = 0.143$, $\eta_{SMN0} = 0.145$), and for case SMN14, a small increase of 2.2 percent is observed. These deviations from the single-phase results are much less than those observed for SM12 and SM14 shown in Fig. 5.22a, with case SMN12 actually showing reduction in η instead of an increase.

Also, it is interesting to note that from comparison of cases MM12-14 and SM12-14 between Figs. 5.19a and 5.22a, the increase in the width of the mixing layer is much larger for the multi-mode initializations than the single-mode initializations. Physically, this results from an increase in the inter-phase coupling within the mixing layer for the multi-mode initializations, and is ultimately observed in the vorticity transport budget. It should be further noted that in the multi-mode RMI, the width of the mixing layer is larger for case MM12 than case MM14. This is a reversal in the trend observed in single-mode RMI, which can be explained by the differences in time-history of vorticity magnitude. For case MM12, at $t = 2.5$ ms, $|\omega_i|$ is 35.5 s^{-2} compared to a value of 25.5 s^{-2} for case MM14, where for the single-mode cases SM12 and SM14 at $t = 2.5$ ms, $|\omega_i|$ is 38.9 s^{-2} and 42.1 s^{-2}, respectively.

In summary, for St $<< 1$, the assumption of gas-particle equilibrium is more accurate, and the two-phase linear impulse model [64] and multi-phase buoyancy-drag model [97] match the trends observed in the current three-dimensional numerical simulations. For St > 1, however, the assumptions made in these models are less accurate since the non-linear two-phase coupling terms are significant.

After the initial shock refraction, the transmitted wave continues to propagate through the two-phase medium. The presence of the particles reduces the speed of the shock wave, thus the time for the wave to reach the end wall and reflect is increased. For instance, the shock wave takes 2.64 ms to travel the length of the domain in case SM0, while it takes 2.81

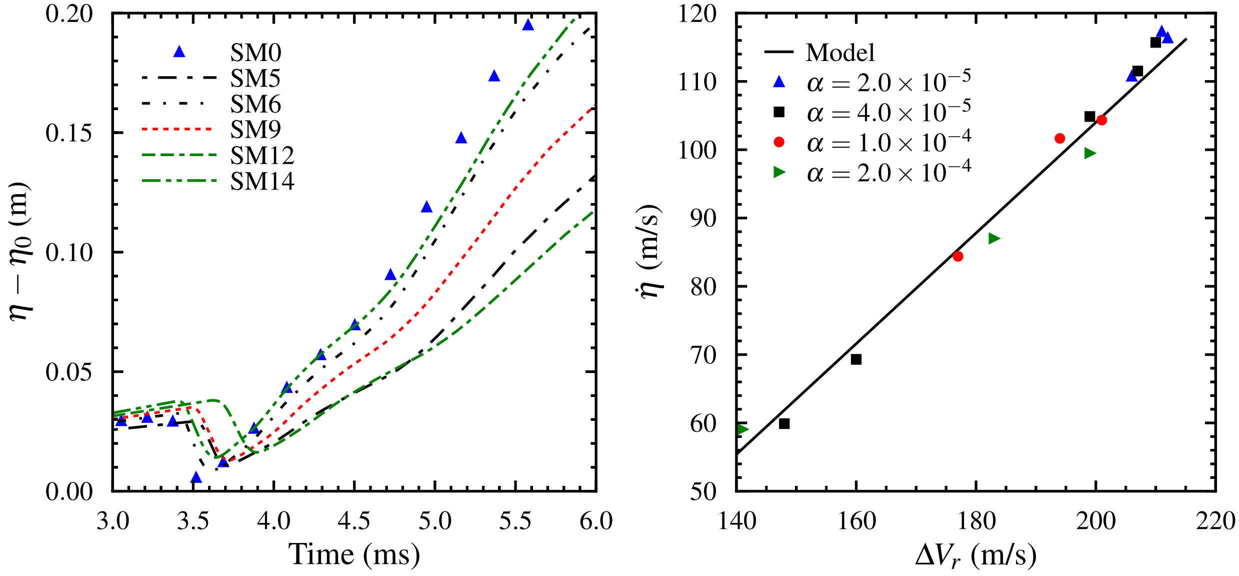

(a) (b)

Figure 5.23: Time evolution of the mixing-layer growth, $\eta(t)$, after re-shock (b) Relationship between the velocity jump, ΔV_r, at re-shock and the re-shocked RMI growth-rate, $\dot{\eta}$, compared to the model given by Eq. 5.12.

ms in case SM5. In general, the dynamics of the shock, particle cloud and mixing zone is summarized in x-t diagram in Fig. 5.21a. At re-shock the reflected wave compresses the flow further and refracts through the developing mixing-zone. As a result of the particle drag, the time at which re-shock is delayed as observed in Fig. 5.23a. This analysis, however, is complicated by the time-dependence of the mass loading. For a given initial volume fraction, simulations with a smaller St (smaller r_p) show that the effective volume fraction increases in the domain (see Fig. 5.21b) as the particle cloud compresses due to the presence of the end-wall. Thus, the total drag is more significant for flows of the same α_0 but smaller St. For example, the mixing layer width just begins to compress at $t_r = 3.73$ ms for case SM12 and at $t_r = 3.51$ ms for case SM14, a 6 percent change, while between cases SM5 and SM8 there is only a 4.5 percent change ($t_r = 3.61$ ms and $t_r = 3.45$ ms, respectively).

The correlation between the velocity jump across the contact at re-shock and the re-shocked RMI growth-rate is shown in Fig. 5.23b with the data summarized. As observed in Fig. 5.23b, there is a clear linear relationship between ΔV_r and $\dot{\eta}_r$. This follows the trends observed in the single-phase re-shock experiments [1] and corresponds to the analytical model derived by Mikaelian [86] given by the correlation

$$\dot{\eta}_r = C A_r^+ \Delta V_r, \tag{5.11}$$

where C is an empirical constant determined by Mikaelian [86] to be 0.28, ΔV_r is the jump in velocity across the contact at re-shock, and A_r^+ is the post re-shock Atwood number. Thornber *et al.* [93] have modified this relationship to account for differences in the initial conditions which are manifested through the changes in the molecular mixing fraction at the time of re-shock. The time evolution of $\Theta(t)$ indicates that the molecular mixing fraction prior to re-shock is a function of the initial St, where the molecular mixing fraction at re-shock, Θ_r, is larger for smaller St. Given this dependence, a semi-analytical model for the re-shocked RMI growth rate can be adapted for dilute gas-particle mixtures and is given by

$$\dot{\eta}_r = C_r \sqrt{1 - \Theta_r} A^+_{m,r} \Delta V_r, \tag{5.12}$$

where similar to the multi-phase impulsive model, Eq. 5.8, the post re-shock multi-phase Atwood number, $A^+_{m,r}$, replaces A^+_r. The value of C_r is determined to be approximately 0.895. Table **??** gives the numerically calculated values of the constant C_r. This model is then used to predict the re-shocked RMI growth rate of the multi-mode cases MM12-14. The agreement is within 10 percent of the numerically predicted values further indicating that both $A^+_{m,r}$ and Θ_r are able to capture the dependence of the re-shocked growth-rate on the initial mass loading and the particle radius. The constant, however, seems to be weakly dependent on the initial volume fraction.

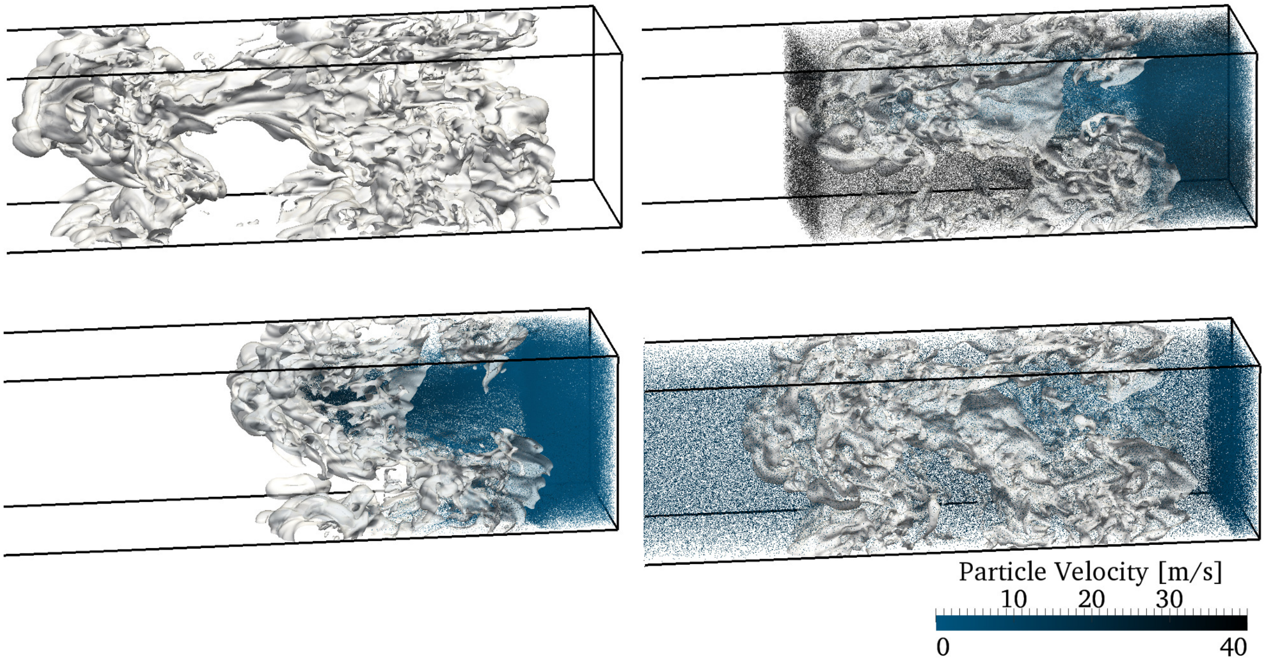

Figure 5.24: Contours of the species mass fraction at $Y_{SF_6} = Y_{Air} = 0.5$ and particle locations colored by the magnitude of the particle velocity for case SM0 (top left), SM5 (bottom left), SM9 (top right) and SM14 (bottom right).

5.4.3 RMI in Conducting Flows

Several recent studies using numerical simulations [99, 100, 101] and simplified analytical models [102, 103, 104, 105, 106] have investigated how the RMI evolves in an electrically conducting flow in the presence of a background magnetic field. Such studies were motivated by previous research on the RTI in similar environments [107, 108], which established that a magnetic field, when parallel to the interface, acts as a stabilizing mechanism similar to the effects of surface tension or viscosity [109]. Magnetic fields perpendicular to the interface, however, were observed to enhance the growth-rate of the RTI. Extending this research, Samtaney *et al* [99] show through numerical simulation that the magnetic field also acts to suppress the growth of the RMI. Since they studied the RMI as it evolves from an oblique contact discontinuity, the magnetic field has components both normal and transverse to the initial interface, and thus no conclusion can be drawn about effect of the field's orientation.

Wheatley *et al* [110] explain that in MHD, when there is a component of the magnetic field vector normal to the contact discontinuity, discontinuities in the transverse components of the velocity across a contact discontinuity are prohibited. Therefore, instead of a vortex sheet forming along the interface of the two fluids and persistently driving the amplification of the interface perturbations, vorticity is transported away from the contact discontinuity by Alfvén waves, which travel along the magnetic field lines. In other words, the vorticity generated by baroclinic torque during shock refraction is not given sufficient time to destabilize the interface and promote mixing. By linearizing the ideal, incompressible magnetohydrodynamic (MHD) equations, Wheatley *et al* [102, 100] show that in the presence of a magnetic field normal to the initial interface perturbation, the RMI grows for some initial time, but then asymptotes to a value inversely proportional to the strength of the magnetic field. This inverse relationship is ultimately related to the velocity of the Alfvén wave, which Wheatley *et al* [100] assume is always larger than some critical value that would be required if the RMI were to be suppressed. Such a critical value must exist, since if the magnetic field is finite, but small, it is possible for the RMI to develop unadulterated [101]–a distinction the current work makes clear.

In the other scenario, where the magnetic field is parallel to the initial density interface, the RMI is potentially stabilized for a different reason, one following from the same logic used to explain the stability of the RTI in a parallel magnetic field–in MHD, their is resistance to the movement of flow across magnetic field lines [17]. These tensile forces are manifested through the Lorentz force, and in the case of the RTI and the RMI, the perturbations amplified by the deposition of vorticity during shock refraction are met with resistance by this force such that their growth is altered. As a result, the instability behaves more like mass-spring-damper system where the growth-rate of the ensuing dynamics is some combination of amplification, dampening, and oscillation [17]. Analytical models derived from the linearized MHD equations seem to corroborate this explanation [103, 104, 105]. Yet, besides the study of Sano *et al*, where only very weak fields were considered, the authors are unaware of any numerical simulations of the RMI investigating the effect of the magnetic field orientation.

In the current work, the evolution of the RMI instability is investigated using three-dimensional numerical simulations. Prior numerical simulations have only been conducted in two-dimensions, for single-mode perturbations, and for magnetic fields orientated normal to the initial interface perturbations. While the analytical model of Wheatley *et al.* [102, 100] is expected to apply in a qualitative sense, the applicability of the model is nonetheless compared against the three-dimensional, single-mode and multi-mode numerical simulations presented in this study. Most importantly, previous analytical models [103, 104, 105, 106] are conflicting on the affect of the transverse magnetic field.

Figure 5.16 shows the computational setup. A Mach 2 shock propagates to the right impinging on the contact discontinuity formed by discontinuity in molecular weight between air (0.79 N_2 / 0.21 O_2 by mole) and SF_6. In the figure, λ is the wavelength of the initial sinusoidal density perturbation of amplitude, a_0, A is the Atwood number defined as $A = (\rho_{SF_6} - \rho_{Air})/(\rho_{SF_6} + \rho_{Air})$. In simulations with an external magnetic field, the field is the direction parallel to the shock wave. In Fig. **??**, the species interface is shown at 0.4 ms for the simulation without an applied magnetic field. The figure shows the bubble-spike formation typical of the RM instability. The growth-rate of instability can be predicted theoretically using Eq. 5.13.

$$\begin{aligned} a_{b/s}(t) &= v_0 \frac{1 + v_0 k t}{1 + D v_0 k t + E v_0^2 k^2 t^2} \\ a(t) &= \frac{1}{2}\left[a_b(t) + a_s(t)\right] \end{aligned} \tag{5.13}$$

where v_0 is the Richtmyer velocity defined as $v_0 = k a_0 A \Delta V$, k is the wavenumber given as $k = 2\pi/\lambda$ and the constants D and E are defined as $D = 1 \pm A$ and $E = 3(1 \pm A)/2(1 + A)$ where the plus sign refers to bubble growth rate, $a_b(t)$, and the negative to spike growth, $a_s(t)$. Defined as such, the theoretical model is referred to as the 2D Sadot model [6].

An explanation for the growth of the instability can be given by observation of the vorticity conservation equation, Eq. 5.14, which is obtained by taking the curl of the momentum conservation equation. The third term on the right-hand-side of the Eq. 5.14 is the baroclinic source term. Baroclinic torque is generated at the interface when the shock passes over the contact discontinuity. The vorticity imparted onto the interface causes the species interface to curl up and form the characteristic spikes and bubbles observed in the bottom figure of Fig. 5.25.

$$\frac{\partial \omega}{\partial t} + \left(u \dot{\nabla}\right) \omega = -\omega \left(\nabla \dot{u}\right) + \left(\omega \dot{\nabla}\right) u + \frac{\nabla \rho \times \nabla p}{\rho^2} + \nabla \left(\frac{\nabla \times B \times B}{\rho}\right) \tag{5.14}$$

When the external magnetic field is applied, the interface is stabilized because the transport of vorticity is fundamentally altered as a result of the different characteristic waves present in MHD flows. This behavior of the RM instability in a perfectly conducting fluid has previously observed and explained [99, 102, 110]. The dynamics, however, are altered when the fluid is no longer perfectly conducting. This situation is more realistic to conditions relevant to aerospace applications. As far as the authors know, the effects of finite resistivity have not been considered before. Considering the drastic change in the dynamics as a result of introducing some resistivity, this work is being investigated further. Preliminary results show that the instability is neither dampened nor does it show the characteristic spikes and bubbles. Figure 5.25 shows a color contour of density at various electrical conductivities. At a critical electrical conductivity, a MHD tearing instability is initiated, which destroys the typical bubble-spike features of the RM instability. Tearing instabilities result when magnetic field lines merge and change topology, which releases magnetic energy. In ideal MHD, the topology of the magnetic field lines are frozen and reconnection is not possible. At still higher electrical conductivity, however, the RM instability is completely stabilized as expected. Figure 5.26 shows the calculated linear growth rate of the RM instability before the tearing instability occurs.

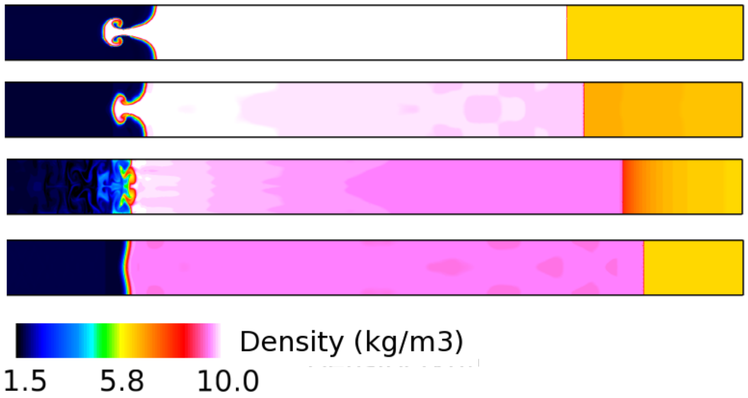

Figure 5.25: Density contours of RM instability for different values of the electrical conductivity. The electrical conductivity increases from top to bottom starting at zero.

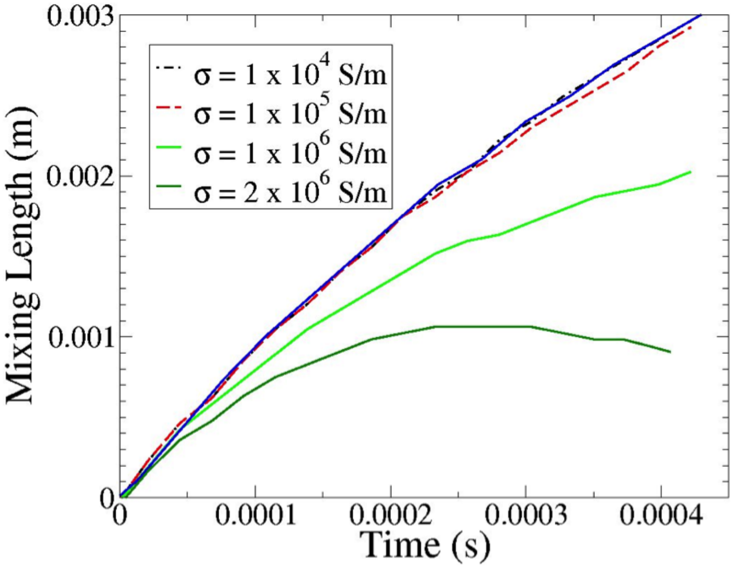

Figure 5.26: The growth-rate of the RM instability before the tearing instability is initiated.

CHAPTER VI

CONCLUSIONS

A multi-physics model capable of simulating MHD flows relevant to study of plasma-producing gaseous detonations and condensed-phase explosions has been developed and validated both quantitatively by comparison to theoretical predictions and experimental measurements as well as qualitatively in the simulation of several canonical MHD flows. A model for predicting the electrical conductivity in a post-detonation flow was developed for H_2-air mixtures with potassium particles. The inclusion of low ionization potential alkali salts in the mixture is necessary to increase the electrical conductivity of the flow to values where MHD effects are observed. While seeding does increase the electrical conductivity, simulations in both one and two dimensions show that the detonation is sensitive to the amount of seeding material injected into the flow. Too high of a seeding percentage adversely affects the detonation propagation. Using these calculations, estimates of the basic non-dimensional MHD parameters were obtained and used simplify the study since it was found that the quasi-static assumption is valid for the majority of conditions observed in post-detonation flows. In condensed-phase explosion, larger values of the magnetic Reynolds number were observed, but methods to calculate the electrical conductivity and the plasma species are still an ongoing topic of research. A simplified model is proposed for dispersed-phase mixtures. Using numerical simulations, the propagation of a detonation wave in the presence of an applied magnetic field is investigated. The interaction parameter is varied as well as the magnetic field orientation in order to investigate how the field may affect the propagation and stability of the detonation. For transverse fields of large N, the cellular structure of the detonation is affected resulting in cell-widths half the size of those observed in detonations with no applied magnetic field. The reduction in the half-reaction distance consequently results in an increase in the detonation velocity. For magnetic fields in the direction of the detonation propagation, an increase in detonation velocity is also observed, but at high N, the transverse waves are adversely affected. The suppression of the transverse waves results in the elimination of the detonation structure. Turning off the magnetic field results in the regeneration of cellular structures. To further understand the mixing processes in these types of flows and how they are affected by the presence of a magnetic field, the Richtmyer-Meshkov instability is studied in detail using detailed three-dimensional numerical simulations. In the dispersed-phase studies, for conditions where $\mathrm{St} < 1$, there is a reduction in the initial growth-rate of the RMI, but with increases in St and mass loading, there is an observable increase in the width of the mixing layer, as much as 43 percent in the range of conditions investigated. This increase is attributed to the additional vorticity production due to the presence of particles and inter-phase momentum coupling–a non-linear affect not observable in the prior simplified analytical models of two-phase RMI. Most importantly, the re-shocked RMI growth rate is shown to be linearly correlated to the velocity jump at re-shock, which is reduced for smaller Stokes numbers. A new growth-rate correlation for the re-shocked RMI growth rate is introduced that is dependent on the molecular mixing fraction and the multi-phase Atwood number at re-shock resulting in a growth-rate constant of approximately 0.895. In studies of the RMI with an applied field, the growth-rate of the mixing layer is shown to be highly dependent on both the electrical conductivity of the flow and value of the magnetic field relative to the Mach number of the initial shock. A critical value is observed for which the instability is suppressed. Moreover, the MHD tearing instability is observed in certain conditions. This instability induces a magnetic reconnection event that drastically alters the flow features and substantially increases the fluid mixing.

CHAPTER VII

SIGNIFICANCE AND RELEVANCE TO THE DTRA MISSION

Fundamental studies of detonations including formation of plasma and its interaction with EM field are very complex but with many practical implications. These processes at the extreme (nuclear) EMP conditions constitute a major WMD threat. Past studies and more recent developments suggest that there are some key areas where better understanding of the underlying physics is needed. Key among them is the nature of plasma formation in the detonation products, and also its characteristic lifetime and evolution, especially since three-dimensional fields can have turbulent features that can be changed under the influence of an external magnetic field. In addition, recent studies have shown that in multi-dimensional detonation, perturbation and/or motion of the detonation front can form vortical features and even cause Richtmyer-Meshkov instability, both of which can have significant impact on the plasma concentration and distribution of ions/electrons. Furthermore, if an external field is imposed on this electrically conducting and spatially heterogeneous field significant changes can occur. Many of these issues have never been addressed in past studies. The unique numerical capabilities developed during this project have allowed the study of basic research problems that focus on these applications.

7.1 Personnel Supported

This research has supported one PhD Graduate Student and part of another student.

7.2 Publications

J.C. Schulz, K.C. Gottiparthi, and S. Menon (2010), “Numerical simulation of non-equilibrium effects and ionization in H_2-air detonations,” AIAA-2010-0772, 48th AIAA Aerospace Sciences Meeting, Orlando, FL, January 2010.

J.C. Schulz, K.C. Gottiparthi, and S. Menon (2012),“Ionization in Gaseous Detonation Waves,” Shock Waves, 22(6), 579–590.

J.C. Schulz, K.C. Gottiparthi, S. Menon (2013), “Richtmyer-Meshkov instability in dilute gas-particle mixtures with re-shock,” Phys. Fluids, 25, 114105.

J.C. Schulz, K.C. Gottiparthi, S. Menon (2013), “On the effects of an external magnetic field on the propagation of detonations in gases,” *under review*, Proceedings of Combustion Institute.

7.3 Related Publications

K. Miki, J.C. Schulz, and S. Menon (2009), "Large Eddy Simulation of equilibrium Plasma-Assisted Combustion in Supersonic Flow," Proceedings of Combustion Institute, 32, 2413–2420.

J.C. Schulz, K. Miki, and S. Menon (2009), "Large-Eddy Simulation of Pulsed Arc Discharges in Supersonic Flow," AIAA-2009-4072, 40th AIAA Aerospace Sciences Meeting, Orlando, FL, January 2009.

K. Miki, J.C. Schulz, and S. Menon (2013), "Large eddy simulation of a free-burning arc discharge in argon with a turbulent cross flow and external field," Plasma Chem. Plasma Process., 33, 959–978.

7.4 Interactions/Transitions

- Interactions where with Eglin AFB Weapons Division on impact of ionization on detonation studies
- Codes developed in Georgia Tech have been delivered to Eglin AFB and Lawrence Livermore National Laboratory (LLNL), CA.

7.5 New Discoveries

7.6 Honors/Awards

- Professor Menon is appointed the Hightower Professor in Engineering by Georgia Tech College of Engineering
- Professor Menon is appointed a Fellow of the American Association for the Advancement of Science (AAAS)

None for this reporting period.

CHAPTER VIII

APPENDIX

The combined model for both hydrogen-air detonation and the subsequent ionization consists of 26 species and 65 reactions and is described by Tables 8.1 and 8.2. From experimental analysis [55], the ionization of NO is the primary pathway for ionization in hydrogen-air mixtures. Thus, modeling of the N_2/O_2 chemistry is most important in non-seeded mixtures, however, for completeness ionization reactions involving all of the hydrogenous species are included whenever reliable data could be found. The N_2/O_2 chemistry relies heavily on the reaction mechanism developed by Park [111, 112], which is widely used with slight modifications in a variety of applications. The electron impact dissociation and ionization reactions are taken from the data collected by Teulet *et al.* [113] and Riahi *et al.* [114]. All reactions are taken as reversible.

This kinetic model is verified by comparison to theoretical values of the detonation velocity and to equilibrium values of the electrical conductivity. The theoretical value of the detonation velocity, D_{CJ}, is computed using NASA's Chemical Equilibrium with Applications (CEA) code [115]. The percent of N_2 in the H_2/O_2 mixture is varied and for each mixture the detonation velocity is calculated using the proposed kinetic mechanisms. The addition of ionization chemistry should not change the overall detonation parameters. For one, N_2/O_2 and ionization chemistry occurs mostly downstream so it doesn't affect the chemical thermicity at the detonation front, and two, the inclusion of the N_2/O_2 and ionization chemistry is actually more accurate with the 18-step and 21-reaction H_2/O_2 model being merely a subset. Regardless, the values from the one-dimensional simulations are within 3-5% of the theoretical values for the range of N_2 dilution considered. As shown in Fig. **??**, both mechanisms are good at predicting the proper detonation parameters.

The electrical conductivity of a stoichiometric mixture of hydrogen and air is computed for various temperatures and pressures using Eq. 3.26. The species mass fractions at equilibrium are determined by integrating in time the conservation of mass, species and energy equations under the assumption of constant pressure. Once the equilibrium species mass fractions are determined, the electrical conductivity is computed. A similar calculation is done with the addition of 1% potassium by weight. The results are shown in Fig. 3.1. The values are similar to those reported elsewhere in the literature [21].

Table 8.1: Summary of the hydrogen-air combustion mechanism used in the present detonation simulations. For the three-body reactions, M includes H_2, O_2, H, O, OH, HO_2, H_2O_2, H_2O and N_2 where the collision efficiency is unity with the exceptions: M_a does not include O_2, H_2O, or N_2, and the collision efficiencies for H_2 and H_2O in M_b are 2.4 and 6.0, in M_c are 1.7 and 7.0, in M_d are 2.4 and 15.4, and in M_e are 0.73 and 3.65, respectively. For reactions $r11$ and $r14$, $k = k_a + k_b$, and for reaction $r12$, $k = k_{\text{inf}}[P_r/(1+P_r)]F$ with $P_r = k_0[\text{M}]/k_{\text{inf}}$ and F as defined in [2].

Number	Reaction	Rate Coefficients			
		A	n	E	
1	$O + H_2 \rightarrow H + OH$	5.0×10^4	2.70	6290	
2	$H + O_2 \rightarrow O + OH$	8.3×10^{13}	0.00	14413	
3	$H + O_2 + M_a \rightarrow HO_2 + M_a$	2.8×10^{18}	−0.90	0	
4	$H + O_2 + O_2 \rightarrow HO_2 + O_2$	3.0×10^{20}	−1.70	0	
5	$H + O_2 + H_2O \rightarrow HO_2 + H_2O$	9.38×10^{18}	−0.80	0	
6	$H + O_2 + N_2 \rightarrow HO_2 + N_2$	2.60×10^{19}	−1.20	0	
7	$H + HO_2 \rightarrow OH + OH$	1.34×10^{14}	0.00	635	
8	$OH + H_2 \rightarrow H_2O + H$	2.16×10^{8}	1.50	3430	
9	$H + H_2O_2 \rightarrow HO_2 + H_2$	1.21×10^{7}	2.00	5200	
10	$H + HO_2 \rightarrow O_2 + H_2$	2.80×10^{13}	0.00	1068	
11	$HO_2 + HO_2 \rightarrow O_2 + H_2O_2$	1.30×10^{11}	0.00	−1630	k_a
		4.20×10^{14}	0.00	12000	k_b
12	$OH + OH + M_b \rightarrow H_2O_2 + M_b$	7.40×10^{13}	−0.40	0	k_{inf}
		2.30×10^{18}	−0.90	−1700	k_0
13	$OH + HO_2 \rightarrow O_2 + H_2O$	2.90×10^{13}	0.00	−500	
14	$OH + H_2O_2 \rightarrow HO_2 + H_2O$	1.75×10^{12}	0.00	320	k_a
		5.80×10^{14}	0.00	9560	k_b
15	$H + H + M_c \rightarrow H_2 + M_c$	1.00×10^{18}	−1.00	0	
16	$O + O + M_d \rightarrow O_2 + M_d$	1.20×10^{17}	−1.00	0	
17	$H + OH + M_e \rightarrow H_2O + M_e$	2.20×10^{22}	−2.00	0	
18	$O + H + M_b \rightarrow OH + M_b$	5.00×10^{17}	−1.00	0	

Table 8.2: Arrhenius rate coefficients for the dissociation reactions. All collision efficiencies are unity. M_f includes N_2, O_2, H_2, NO, OH, H_2O_2, HO_2, H_2O and all ions, and M_g includes N, O, H. In order not to repeat reactions included in the combustion chemistry, M_h only includes NO and all ions, and M_i includes NO, N and all ions.

Number	**Reaction**	**Rate Coefficients**			**Ref.**
		A	n	E	
Dissociation					
19	$N_2 + M_f \rightarrow N + N + M_g$	7.0×10^{21}	-1.60	113200	[112]
20	$N_2 + M_g \rightarrow N + N + M_g$	3.0×10^{22}	-1.60	113200	[112]
21	$O_2 + M_h \rightarrow O + O + M_h$	2.0×10^{21}	-1.50	59360	[112]
22	$O_2 + N \rightarrow O + O + N$	1.0×10^{22}	-1.50	59360	[112]
23	$H_2 + M_i \rightarrow H + H + M_i$	2.2×10^{14}	0.00	48300	[112]
24	$NO + M_f \rightarrow N + O + M_f$	5.0×10^{15}	0.00	75500	[111]
25	$NO + M_g \rightarrow N + O + M_g$	1.1×10^{17}	0.00	75500	[111]
Electron Impact Dissociation					
26	$N_2 + e \rightarrow N + N + e$	2.48×10^{-9}	6.16	113263	[113]
27	$O_2 + e \rightarrow O + O + e$	3.47×10^{2}	3.52	59370	[113]
28	$H_2 + e \rightarrow H + H + e$	2.69×10^{20}	-0.80	126565	[114]
29	$H_2O + e \rightarrow H + OH + e$	3.20×10^{15}	0.50	92832	[116]
30	$NO + e \rightarrow N + O + e$	1.05×10^{-2}	4.52	75390	[113]
31	$OH + e \rightarrow O + H + e$	1.54×10^{20}	-0.76	80107	[114]
Electron Impact Ionization					
32	$N_2 + e \rightarrow N_2^+ + e + e$	5.17×10^{12}	0.72	184300	[113]
33	$O_2 + e \rightarrow O_2^+ + e + e$	2.20×10^{10}	1.16	130102	[113]
34	$H_2 + e \rightarrow H_2^+ + e + e$	1.78×10^{9}	1.61	207369	[114]
35	$H_2O + e \rightarrow H_2O^+ + e + e$	8.40×10^{15}	0.50	174060	[116]
36	$H_2O + e \rightarrow H + OH^+ + e + e$	2.80×10^{15}	0.50	209376	[116]
37	$NO + e \rightarrow NO^+ + e + e$	2.70×10^{10}	1.13	95092	[113]
38	$OH + e \rightarrow OH^+ + e + e$	6.99×10^{6}	1.78	160267	[114]
39	$N + e \rightarrow N^+ + e + e$	2.50×10^{34}	-3.82	168600	[111]
40	$O + e \rightarrow O^+ + e + e$	3.90×10^{33}	-3.78	158500	[111]
41	$H + e \rightarrow H^+ + e + e$	2.20×10^{30}	-2.80	157800	[112]
Zel'dovich Reactions					
42	$O_2 + N \rightarrow NO + O$	2.49×10^{9}	1.18	4006	[117]
43	$N_2 + O \rightarrow NO + N$	5.69×10^{12}	0.42	42938	[118]
Dissociative Recombination					
44	$N + N \rightarrow N_2^+ + e$	4.40×10^{7}	1.50	67500	[111]
45	$O + O \rightarrow O_2^+ + e$	7.10×10^{2}	2.70	80600	[111]
46	$N + O \rightarrow NO^+ + e$	8.80×10^{8}	1.00	31900	[111]
47	$OH^+ + e \rightarrow O + H$	3.91×10^{17}	-0.50	0	[119]
48	$H_2O^+ + e \rightarrow OH + H$	3.29×10^{18}	-0.50	0	[119]
Charge Exchange					
49	$O + NO^+ \rightarrow O_2 + N^+$	1.00×10^{12}	0.50	77200	[111]
50	$N_2 + N^+ \rightarrow N + N_2^+$	1.00×10^{12}	0.50	12200	[111]
51	$N + O_2^+ \rightarrow O_2 + N^+$	8.70×10^{13}	0.14	28600	[111]
52	$NO + O^+ \rightarrow O_2 + N^+$	1.40×10^{5}	1.90	15300	[111]
53	$N_2 + O_2^+ \rightarrow O_2 + N_2^+$	9.90×10^{12}	0.00	40700	[111]
54	$O + O_2^+ \rightarrow O_2 + O^+$	4.00×10^{12}	-0.09	18000	[111]
55	$N + NO^+ \rightarrow N_2 + O^+$	3.40×10^{13}	-1.08	12800	[111]
56	$O_2 + NO^+ \rightarrow NO + O_2^+$	2.40×10^{13}	0.41	32600	[111]
57	$O + NO^+ \rightarrow N + O_2^+$	7.20×10^{12}	0.29	48600	[111]
58	$N_2 + O^+ \rightarrow O + N_2^+$	9.10×10^{11}	0.36	22800	[111]
59	$N + NO^+ \rightarrow O + N_2^+$	7.20×10^{13}	0.00	35500	[111]
Potassium Reactions					
60	$K + O_2 + M \rightarrow KO_2 + M$	1.138×10^{2}	-2.68	596	[27]
61	$K + OH + M \rightarrow KOH + M$	1.144×10^{-1}	-2.00	0	[27]
62	$KOH + H \rightarrow K + H_2O$	2.21×10^{12}	0.50	0	[27]
63	$KO_2 + H \rightarrow KO + OH$	2.21×10^{12}	0.50	0	[27]
64	$KO + H_2O \rightarrow KOH + OH$	5.95×10^{11}	0.50	0	[27]
65	$K + M \rightarrow K^+ + e + M$	5.962×10^{15}	0.50	101055	[28]

REFERENCES

[1] M. Vetter and B. Sturtevant. Experiments on the Richtmyer-Meshkov instability of an air/SF_6 interface. *Shock Waves*, 4:247–252, 1995.

[2] E.L. Petersen and R. K. Hanson. Reduced kinetics mechanisms for ram accelerator combustion. *Journal of Propulsion and Power*, 15(4):591–600, 1999.

[3] W. Dai and P.R. Woodward. Extension of the piecewise Parabolic Method to Multidimensional ideal magnetohdrodynamics. *J. Comput. Phys.*, 115(2):485–514, 1998.

[4] D. Ryu and T.W. Jones. Numerical magnetohydrodynamics in astrophysics: algorithm and tests for one-dimensional flow. *Astrophys. J.*, 442:228–260, 1995.

[5] A. V. Fedorov, D. A. Tropin, and I. A. Bedarev. Mathematical modeling of detonation suppression in a hydrogen-oxygen mixture by inert particles. *Combustion, Explosion and Shock Waves*, 46(3):332–343, 2010.

[6] O. Sadot, L. Erez, U. Alon, D. Oron, and L.A. Levin. Study of nonlinear evolution of single-mode and two-bubble interaction under Richtmyer-Meshkov instability. *Phys. Rev. Lett.*, 80:1654–1657, 1998.

[7] D. Biskamp and W.-C. Müller. Scaling properties of three-dimensional isotropic magnetohydrodynamic turbulence. *Phys. Plasmas*, 7(12):4889–4891, 2000.

[8] R. Monchaux, M. Berhanu, S. Aumaître, A. Chiffaudel, F. Daviaud, B. Dubrulle, F. Ravelet, S. Fauve, N. Mordant, F. Pétrélis, M. Bourgoin, P. Odier, J.-F. Pinton, B. Plihon, and R. Volk. The von Kármán sodium experiment: turbulent dynamical dynamos. *Phys. Fluids*, 21(035108), 2009.

[9] B. Knaepen and R. Moreau. Magnetohydrodynamic turbulence at low magnetic Reynolds number. *Annu. Rev. Fluid Mech.*, 40:25–45, 2008.

[10] M.A. Cook and T.Z. Gwyther. Influence of electrical fields on shock to detonation transition. Technical report, Utah University, Salt Lake City, UT, 1965.

[11] D.G. Tasker, V.H. Whitley, J.L. Mace, S.J. Pemberton, T.D. Sandoval, and R.J. Lee. Electromagnetic effects on explosive reaction and plasma. In *Proceedings of the 14th International Detonation Symposium*, 2009.

[12] M.A. Cook. *The Science of High Explosives.* Reinhold Publishing Corporation, New York, 1958.

[13] M.A. Cook and W.S. McEwan. Cohesion in plasma. *J. Appl. Phys.*, 29(11):1612–1613, 1958.

[14] M.A. Cook, R.T. Keyes, and L.L. Udy. Propagation characteristics of detonation-generated plasmas. *J. Appl. Phys.*, 30(12):1882–1892, 1959.

[15] F. Chen. *Introduction to Plasma Physics.* Plenum Press, New York, NY, Second edition, 1974.

[16] D. Biskamp. *Magnetohydrodynamic turbulence.* Cambridge University Press, Cambridge, United Kingdom, 2003.

[17] P.A. Davidson. *An Introduction to Magnetohydrodynamics.* Dover Publications, 2001.

[18] Franklin Génin and Suresh Menon. Dynamics of sonic jet injection into supersonic crossflow. *J. Turbulence*, 11(4):1–30, 2010.

[19] J.C. Schulz, K.C. Gottiparthi, and S. Menon. Ionization in gaseous detonation waves. *Shock Waves*, 22(6):579–590, 2012.

[20] S. C. Lin, E. L. Resler, and A. Kantrowitz. Electrical conductivity of highly ionized argon produced by shock waves. *J. Appl. Phys.*, 26:95–109, 1955.

[21] F.K. Lu, H.-C. Liu, and D.R. Wilson. Electrical conductivity channel for a shock tube. *Meas. Sci. Tech.*, 16:1730–1740, 2005.

[22] B. Stefanov and L. Zarkova. Electron-potassium-atom momentum transfer cross section: fit to the experimental data. *J. Phys. B: At. Mol. Phys.*, 20:2281–2289, 1987.

[23] M.J. Wright, D. Bose, G.E. Palmer, and E. Levin. Recommended collision integrals for transport property computations, part 1: Air species. *AIAA Journal*, 43(12):2558–2564, 2005.

[24] M. Yousfi and M.D. Benabdessadok. Boltzmann equation analysis of electron-molecule collision cross sections in water vapor and ammonia. *Journal of Applied Physics*, 80(12):6619–6630, 1996.

[25] J.R. Stallcop, H. Partridge, and E. Levin. Collision integrals for the interaction of the ions of nitrogen and oxygen in a plasma at high temperatures and pressures. *Phys. Fluids B*, 4:386–391, 1992.

[26] N. Tsuboi, S. Katoh, and K. Hayashi. Three-dimensional numerical simulation for hydrogen/air detonation: Rectangular and diagonal structures. *Proc. Combust. Inst.*, 29(2):2783–2788, 2002.

[27] M. Slack, J.W. Cox, A. Grillo, and R. Ryan. Potassium kinetics in heavily seeded atmospheric pressure laminar methane flames. *Combustion and Flame*, 77:311–320, 1989.

[28] A.F. Ashton and A.N.: Hayhurst. Kinetics of collisional ionization of alkali metal atoms and recombination of electrons with alkali metal ions in flames. *Combustion and Flame*, 21(1):69–75, 1973.

[29] D.M. Snider. An incompressible three-dimensional multiphase particle-in-cell model for dense particle flows. *J. Comput. Phys.*, 170:523–545, 2001.

[30] K. C. Gottiparthi and S. Menon. A study of interaction of clouds of inert particles with detonation in gases. *Combustion Science and Technology*, 184(3):406–433, 2012.

[31] S. Srinivasan, A. Smith, and S. Menon. Accuracy, reliability and performance of spray combustion models in large-eddy simulations. In Maria Vittoria Salvetti, Bernard Geurts, Johan Meyers, and Pierre Sagaut, editors, *Quality and Reliability of Large-Eddy Simulations II*, pages 211–220. Springer, 2011.

[32] S. Ukai, K. Balakrishnan, and S. Menon. On Richtmyer-Meshkov instability in dilute gas-particle mixtures. *Physics of Fluids*, 22(104103):1–12, 2010.

[33] V. M. Boiko, V. P. Kiselev, S. P. Keselev, A. P. Papyrin, S. V. Poplavsky, and V. M. Fomin. Shock wave interaction with a cloud of particles. *Shock Waves*, 7:275–285, 1997.

[34] R.M. Drake. Discussion on the paper entitled “forced convection heat transfer from an isothermal sphere to water” by G.C. Violet and G. Leppert. *ASME J. Heat Trans.*, 83(2):170–182, 1961.

[35] K. Miki and S. Menon. Localized dynamic subgrid closure for simulation of MHD turbulence. *Phys. Plasmas*, 15(072306), 2008.

[36] Franklin Génin. *Study of Compressible Turbulent Flows in Supersonic Environment by Large-Eddy Simulation*. PhD thesis, Georgia Institute of Technology, 2009.

[37] G. Tóth. The $\bigtriangledown \cdot B = 0$ constraint in shock-capturing magnetohydrodynamic code. *J. Comput. Phys.*, 161:605–652, 2000.

[38] J.U. Brackbill and D.C. Barnes. The effect of nonzero $\bigtriangledown \cdot B = 0$ on the numerical solution of the magnetohydrodynamic equations. *J. Comput. Phys.*, 35:426–430, 1980.

[39] C.R. Evans and J.F. Hawley. Simulation of magnetohydrodynamic flows: A constrained transport method. *Astrophys. J.*, 332:659–677, 1988.

[40] D. Ryu, F. Miniati, T. W. Jones, and A. Frank. A divergence-free upwind code for multidimensional magnetohydrodynamics flows. *Astrophys. J.*, 509:244–255, 1998.

[41] M. Brio and C.C. Wu. An upwind differencing scheme for the equations of ideal magnetohydrodynamics. *J. Comput. Physics*, 75(2):400–422, 1988.

[42] P.L. Roe. Approximate Riemann solver, parameters vectors and difference schemes. *J. Comput. Phys.*, 43:357–371, 1981.

[43] P. Cargo and G. Gallice. Roe matrics for ideal MHD and systematic construction of Roe matrices for systems of conservation laws. *J. Comput. Phys.*, 136(9):446–466, 1997.

[44] D.S. Balsara. Total variation diminishing scheme for adiabatic and isothermal magnetohydrodynamics. *Astrophys. J. Suppl. Ser.*, 116:133–153, 1998.

[45] A.L. Zachary, A. Malagoli, and P. Colella. A high-order Godunov method for multidimensional ideal magnetohydrodynamics. *SIAM J. Sci. Comput.*, 15(2):263–284, 1994.

[46] P. Colella and P. Woodward. The Piecewise-Parabolic Method for hydrodynamics. *J. Comput. Phys.*, 54:174–201, 1984.

[47] W. Dai and P.R. Woodward. An approximate riemann solver for ideal magnetohdrodynamics. *J. Comput. Phys.*, 111(2):354–372, 1998.

[48] K.G. Powell, T.J. Roe, and T.I. Linde. A solution-adaptive upwinding scheme for ideal magnetohydrodynamics. *J. Comput. Phys.*, 154:284–309, 1999.

[49] A. Harten, P.D. Lax, and B. van Leer. On upstream differencing and Godunov-type schemes for hyperbolic conservation laws. *SIAM Review*, 25:35–61, 1983.

[50] T. Miyoshi and K. Kusano. A multi-state HLL approximate Riemann solver for ideal magnetohydrodynamics. *J. Comput. Phys.*, 208:315–344, 2005.

[51] B. Fyrxell and S. Menon. Hybrid simulations of Richtmyer-Meshkov instability. *AIAA-2005-0314, 43rd, AIAA Aerospace Sciences Meeting*, Reno, NV, 10-13 January 2005.

[52] R. Löhner. Finite elements in CFD: what lies ahead. *International Journal for Numerical Methods in Engineering*, 24:1741–1756, 1987.

[53] S.A. Orszag. Two-dimensional turbulence on the surface of a sphere. *J. Fluid Mech.*, 87(2):305–319, 1978.

[54] S. Basu. Ionization in seeded detonation waves. *Proceedings of the 7th International Detonation Symposium*, 1959.

[55] D.H. Edwards, G. Hooper, and A.A. Collyer. Ionization measurement in reactive shock and detonation waves using microwave techniques. *JournalofPhysicsDAppliedPhysics*, 4:854–870, 1971.

[56] W. Fickett and W.C. Davis. *Detonation.* University of California Press, 1979.

[57] J. .H. .S. Lee and A. .J. Higgins. Comments on criteria for direct initiation of detonation. *Phil. Trans. R. Soc. Lond. A*, 357:3503–3521, 1999.

[58] S. Basu. Ionization in seeded detonation waves. *Phys. Fluids*, 3(3):456–463, 1960.

[59] G.J. Sharpe. Transverse waves in numerical simulations of cellular detonations. *J. Fluid Mech.*, 447:31–51, 2001.

[60] K. Balakrishnan and S. Menon. On the role of ambient reactive particles in the mixing and afterburn behind explosive blast waves. *Combustion Science and Technology*, 182:186–214, 2010.

[61] K. Miki, J.C. Schulz, and S. Menon. Large eddy simulation of equilibrium plasma-assisted combustion in supersonic flow. *Proc. Combust. Inst.*, 32:2413–2420, 2008.

[62] J.E. Shepherd. Detonation in gases. *Proc. Combust. Inst.*, 32(1):83–98, 2009.

[63] M. Brouillette. The richtmyer-meshkov instability. *Annual Review of Fluid Mechanics*, 34:445–468, 2002.

[64] S. Ukai, K. Balakrishnan, and S. Menon. Growth rate predictions of single- and multi-mode Richtmyer-Meshkov instability with reshock. *Shock Waves*, 21(6):533–546, 2011.

[65] R.D. Richtmyer. Taylor instability in shock acceleration of compressible fluids. *Commun. Pure Appl. Math.*, 8:297–319, 1960.

[66] M.A. Jones and J.W. Jacobs. A membraneless experiment for the study of Richtmyer-Meshkov instability of a shock-accelerated gas interface. *Phys. Fluids*, 9:3078–3085, 1997.

[67] R.L. Holmes, G. Dimonte, B. Fryxell, M.L. Gittings, and J.W. Grove. Richtmyer-Meshkov instability growth: experiment, simulation and theory. *J. Fluid Mech.*, 389:55–79, 1999.

[68] P.R. Chapman and J.W. Jacobs. Experiments on the three-dimensional incompressible Richtmyer-Meshkov instability. *Phys. Fluids*, 18(074101), 2006.

[69] H. Hecht, U. Alon, and D. Shvarts. Potential flow models of Rayleigh-Taylor and Richtmyer-Meshkov bubble fronts. *Phys. Fluids*, 6:4019–4030, 1994.

[70] Q. Zhang and S.-I. Sohn. Nonlinear theory of unstable fluid mixing drive by shock wave. *Phys. Fluids*, 9:1106–1124, 1997.

[71] P.G. Saffman and D.I. Meiron. Kinetic energy generated by the incompressible Richtmyer-Meshkov instability in a continuous stratified fluid. *Phys. Fluids A*, 1:1767–1771, 1989.

[72] M. Brouillette and B. Strutevant. Experiments on the Richtmyer-Meshkov instability: small-scale perturbations on a continuous interface. *J. Fluid Mech.*, 263:271–292, 1994.

[73] G. Dimonte, C.E. Frerking, and M. Schneider. Richtmyer-Meshkov instability in the turbulent regime. *Phys. Rev. Lett.*, 74:4855–4858, 1995.

[74] B. Thornber, D. Drikakis, D.L. Youngs, and R.J.R. Williams. The influence of initial conditions on turbulent mixing due to Richtmyer-Meshkov instability. *Journal of Fluid Mechanics*, 654:99–139, 2010.

[75] G. Dimonte and M. Schneider. Turbulent Rayleigh-Taylor instability experiments with strong radiatively drive shocks. *Phys. Plasmas*, 4:4347–4357, 1997.

[76] G. Dimonte and M. Schneider. Density ratio dependence of Rayleigh-Taylor mixing for sustained and impulsive acceleration histories. *Phys. Fluids*, 12:304–321, 2000.

[77] J.K. Prasad, A. Rasheed, S. Kumar, and B. Sturtevant. The late-time development of the Richtmyer-Meshkov instability. *Phys. Fluids*, 12:2108–2015, 2000.

[78] D. Oron, L. Arazl, D. Kartoon, A. Rikanati, U. Alon, and D. Shvarts. Dimensionality dependence of the Rayleigh-Taylor and Richtmyer-Meshkov instability late-time scaling laws. *Phys. Plasmas*, 8(6):2883–2889, 2001.

[79] O. Sadot, L. Erez, D. Oron, G. Erez, and G. Ben-Dor. Studies on the nonlinear evolution of the Richtmyer-Meshkov instability. *Astrophys. J. Suppl. S.*, 127:469–473, 2000.

[80] J.D. Ramshaw. Simple model for linear and nonlinear mixing at unstable fluid interfaces with variable acceleration. *Phys. Rev. E*, 58:5834–5840, 1998.

[81] M. Lombardini, D.I. Pullin, and D.I. Meiron. Transition to turbulence in shock-driven mixing: a mach number study. *Journal of Fluid Mechanics*, 690:203–226, 2012.

[82] G.C. Orlicz, S. Balakumar, C.D. Tomkins, and K.P Prestridge. A Mach number study of the Richtmyer-Meshkov instability in a varicose, heavy-gas curtain. *Physics of Fluids*, 21(064102), 2009.

[83] M. Lombardini, D.J. Hill, D.I. Pullin, and D.I. Meiron. Atwood ratio dependence of Richtmyer-Meshkov flows under reshock conditions using large-eddy simulations. *Journal of Fluid Mechanics*, 670:439–480, 2011.

[84] B.J. Balakumar, G.C. Orlicz, J.R. Ristorcelli, S. Balasubramanian, K.P. Prestridge, and C.D. Tomkins. Turbulent mixing in a Richtmyer-Meshkov fluid layer after reshock: velocity and density statistics. *J. Fluid Mech.*, 696:67–93, 2012.

[85] E. Leinov, G. Malamud, Y. Elbaz, L.A. Levin, G. Ben-Dor, D. Shvarts, and O. Sadot. Experimental and numerical investigation of the Richtmyer-Meshkov instability under re-shock conditions. *J. Fluid Mech.*, 626:449–480, 2009.

[86] K.O. Mikaelian. Turbulent mixing generated by Rayleigh-Taylor and Richtmyer-Meshkov instabilities. *Physica D*, 36:356–368, 1989.

[87] A.A. Charakhch'yan. Reshocking at the non-linear stage of the Richtmyer-Meshkov instability. *Plasma Phys. Contr. F.*, 43:1169–1179, 2001.

[88] R.H. Cohen, W.P. Dannevik, A.M. Dimits, D.E. Eliason, A.A. Mirin, Y. Zhou, D.H. Porter, and P.R. Woodward. Three-dimensional simulation of a Richtmyer-Meshkov instability with a two-scale initial perturbation. *Physics of Fluids*, 14:3692–3709, 2002.

[89] D.J. Hill, C. Pantano, and D.I. Pullin. Large-eddy simulation and multiscale modelling of a Richtmyer-Meshkov. *Journal of Fluid Mechanics*, 557:29–61, 2006.

[90] O. Schilling and M. Latini. High-order WENO simulations of three-dimensional reshocked Richtmyer-Meshkov instability to late times: dynamics, dependence of initial conditions, and comparisons to experimental data. *Acta Mathematica Scientia*, 30B(2):595–620, 2010.

[91] L. Houas and I. Chemouni. Experimental investigation of the Richtmyer-Meshkov instability in shock tube. *Phys. Fluids*, 8:614–627, 1996.

[92] A.A. Gowardhan and F.F Grinstein. Numerical simulation of Richtmyer-Meshkov instabilities in shock gas curtains. *J. Turbul.*, 12(43):1–24, 2011.

[93] B. Thornber, D. Drikakis, D.L. Youngs, and R.J.R. Williams. Growth of a Richtmyer-Meshkov turbulent layer after reshock. *Physics of Fluids*, 23(095107):1–14, 2011.

[94] K.O. Mikaelian. Analytic approach to nonlinear Rayleigh-Taylor and Richtmyer-Meshkov instabilities. *Phys. Rev. Lett.*, 80:508–511, 1998.

[95] K. Balakrishnan and S. Menon. On turbulent chemical explosions into dilute aluminum particle clouds. *Combustion Theory and Modelling*, 14(4):583–617, 2010.

[96] P.K. Shukla. A survey of dusty plasma physics. *Physics of Plasmas*, 8(5):1791–1804, 2001.

[97] K. Balakrishnan and S. Menon. A multiphase bouyancy-drag model for the study of Rayleigh-Taylor and Richtmyer-Meshkov instabilities in dusty gases. *Laser and Particle Beams*, 29:201–217, 2011.

[98] Y. Srebro, Y. Elbaz, O. Sadot, L. Arazi, and D. Shvarts. A general buoyancy-drag model for the evolution of the Rayleigh-Talyor and Richtmyer-Meshkov instabilities. *Laser and Particle Beams*, 21:347–353, 2003.

[99] R. Samtaney. Suppression of the Ritchmyer-Meshkov instability in the presence of a magnetic field. *Phys. Fluids*, 15(8):L53–56, 2003.

[100] V. Wheatley, R. Samtaney, and D.I. Pullin. The Richtmyer-Meshkov instability in magnetohydrodynamics. *Phys. Fluids*, 21(082102):1–13, 2009.

[101] T. Sano, K. Nishihara, C. Matsuoka, and T. Inoue. Magnetic field amplification associated with the Richtmyer-Meskhov instability. *Astrophys. J.*, 758:126–139, 2012.

[102] V. Wheatley, D.I. Pullin, and R. Samtaney. Stability of an impulsively accelerated density interface in magnetohydrodynamics. *Phys. Rev. Lett.*, 95(125002):1–4, 2005.

[103] Z. Qiu, Z. Wu, J. Cao, and D. Li. Effects of transverse magnetic field and viscosity on the Richtmyer-Meshkov instability. *Phys. Plasmas*, 15:042305, 2008.

[104] J. Cao, W. Wu, H. Ren, and D. Li. Richtmyer-Meshkov instability of a stratified fluid in transverse magnetic field. *Phys. Plasmas*, 16(062103), 2009.

[105] M. Khan, L. Mandal, R. Banerjee, S. Roy, and M. R. Gupta. Development of Richtmyer-Meshkov and Rayleigh-Taylor instability in the presence of a magnetic field. *Nucl. Instr. and Meth. A*, 653:2–6, 2011.

[106] Y. Levy, S. Jaouen, and B. Canaud. Numerical investigation of magnetic Richtmyer-Meshkov instability. *Laser Part. Beams*, 30:415–419, 2012.

[107] S. Chandrasekhar. *Hydrodynamic and Hydromagnetic Stability.* Dover, New York, 1961.

[108] B.-I. Jun, M. L. Norman, and J. M. Stone. A numerical study of Rayleigh-Taylor instability in magnetic fluids. *Astrophys. J.*, 453:332–349, 1995.

[109] K. O. Mikaelian. Effect of viscosity on rayleigh-taylor and richtmyer-meshkov instabilities. *Phys. Rev. E*, 47:375–383, 1993.

[110] V. Wheatley, D.I. Pullin, and R. Samtaney. Regular shock refraction at an oblique planar density interface in magnetohydrodynamics. *J. Fuild Mech.*, 522:179–214, 2005.

[111] C. Park. Review of chemical-kinetic problems of future nasa missions, i: Earth entries. *JournalofThermophsyicsandHeatTransfer*, 7:385–398, 1993.

[112] C. Park. Chemical-kinetic parameters of hyperbolic earth entry. *AIAA Paper 00-0210*, 2000.

[113] Ph. Teulet, J.P. Sarrette, and A.M. Gomes. Calculation of electron impact inelastic cross sections and rate coefficients for diatomic molecules. applications to air molecules. *Journal of Quantitative Spectroscopy and Radiative Transfer*, 62:549–569, 1999.

[114] R. Riahi, Ph. Teulet, Z.B. Lakhdar, and A. Gleizes. Cross-section and rate coefficient calculate for electron impact excitation, ionisation and dissociation of h_2 and oh molecules. *European Physical Journal D*, 2006:223–230, 40.

[115] B. J. McBride and S. Gordon. Computer program for calculating and fitting thermodynamic functions. Technical Report RP-1271, NASA, 1992.

[116] R.S. Konstantinovskii, V.M. Shibkov, and L.V. Shibkova. Effect of a gas discharge on the ignition in the hydrogen-oxygen system. *Kinetics and Catalysis*, 46(6):775–788, 2005.

[117] D. Bose and G.V. Candler. Thermal rate constants of the $o_2 + n \rightarrow no + o$ reaction using *ab initio* $^2a'$ and $^4a'$ potential-energy surfacesr. *Journal of Chemical Physics*, 107(16):6163–6145, 1997.

[118] D. Bose and G.V. Candler. Thermal rate constants of the $n_2 + o \rightarrow no + n$ reaction using *ab initio* $^3a''$ and $^3a'$ potential energy surfaces. *Journal of Chemical Physics*, 104(8):2825–2833, 1996.

[119] J.B.A. Mitchell. The dissociation recombination of molecules. *Physical Report*, 186:216–248, 1990.

8.1 Published Papers

Shock Waves (2012) 22:579–590
DOI 10.1007/s00193-012-0412-9

ORIGINAL ARTICLE

Ionization in gaseous detonation waves

J. C. Schulz · K. C. Gottiparthi · S. Menon

Received: 10 April 2012 / Revised: 21 August 2012 / Accepted: 11 September 2012 / Published online: 12 October 2012
© Springer-Verlag Berlin Heidelberg 2012

Abstract Using numerical simulations the spatial and temporal evolution of the electrical conductivity in ionized gas mixtures produced by detonation is investigated in mixtures with and without potassium seeding. Without flow seeding, the magnitude of the electrical conductivity is observed to be too small for significant magnetohydrodynamic forces to affect the conducting flow. This is consistent with past observations. With potassium seeding the electrical conductivity can be increased by 4–5 orders of magnitude, however, a critical percentage of seed particles is observed for which detonation is no longer sustainable. Therefore, there are limits to the electrical conductivity that can be achieved in burned gas mixtures. To further understand the dynamics of the physics involved a parametric study is conducted by varying the ambient pressure, the nitrogen dilution and the potassium seeding percentage. In order to reach these conclusions, a detailed kinetic mechanism of 26 species and 65 reactions has been compiled from the available literature and validated for applications of detonation and ionization chemistry. From the computed mass fractions the mixture-averaged electrical conductivity is then computed.

Keywords Detonation · Ionization · Electrical conductivity

Communicated by F. Lu.

J. C. Schulz (✉) · K. C. Gottiparthi · S. Menon
School of Aerospace Engineering, Georgia Institute of Technology,
Atlanta, GA 30332-0150, USA
e-mail: jschulz@gatech.edu

S. Menon
e-mail: suresh.menon@aerospace.gatech.edu

1 Introduction

The interaction between an electromagnetic field and a conducting flow is of interest since magnetohydrodynamic (MHD) forces can generate electrical power, increase propulsive thrust or improve aerodynamic performance. How these MHD forces interact with the flow and how well they might improve the efficiency of the device is predominately determined by the electrical conductivity of the gas mixture. Using numerical simulations, this paper addresses for the first time the spatial and temporal evolution of the electrical conductivity in ionized gas mixtures produced by detonation. Such work is directly applicable to MHD applications in pulse-detonation engines [7], but is also a first step in addressing the role electromagnetic fields play in the initiation and the propagation of detonation waves [29].

The first measurements of electrical conductivity in gaseous detonations were conducted by Basu and Fay [3] in gaseous mixtures of H_2/O_2 and C_2H_2/O_2 with an inclusion of 0.667 % N_2. From theoretical calculation and comparison to the experimental results, the formation of NO ions was concluded to be the dominating contribution to the rise in the electrical conductivity followed by contributions from O_2 and H_2O ions. The initial pressure was varied from 0.1 to 1.0 atm. Higher initial pressures resulted in higher values of conductivity. Edwards et al. [8] have compiled a large amount of data for both H_2/O_2 and C_2H_2/O_2 mixtures. The measured conductivities are in the range of 10^{-3}–10^{-1} S m^{-1} depending on the conditions. More recent studies of electrical conductivity in gaseous detonation have reported similar trends [32].

At such low electrical conductivities, however, MHD effects are negligible. For these effects to be of importance, the electrical conductivity must be increased. In order to do this particles with low ionization potentials, such as potassium carbonate, are injected into the flow where the formation of potassium ions increases the electrical conductivity. Basu and Fay [4] report an electrical conductivity of 270 S m^{-1} in oxy-acetylene detonations at initial pressures of 0.1 atm when seeded with 3 % potassium acetylide–a four-order of magnitude increase compared to the non-seeded electrical conductivity. More recently, similar studies using a potassium carbonate seed were done in hydrogen–oxygen detonations [17]. In this work the measured electrical conductivity was much less than expected. The researchers attribute this to poor mixing and incomplete oxidation of the potassium carbonate, however, a two-order of magnitude increase in the electrical conductivity is still observed for a 1 % addition of potassium by weight. The effect of alkali metals has been studied more extensively in flames [26]. In these studies a 1 % addition of potassium can result in flame extinction due to heat absorption by the seed particle during phase transition and the increased competition for atomic oxygen in the reacting mixture. Such effects may not necessarily be detrimental to detonations, which are sustained by different mechanisms, yet a study of the effect of seed particles on detonation has not been done.

To address the effect of seeding on both the ionization process and the detonation physics, numerical simulations are used to gain in depth understanding of the time-dependent and spatial processes involved in flows with and without seeding. Such simulations are important in MHD applications for pulse-detonation engines, and more fundamentally in the study of the effects of electromagnetic fields on detonation. A finite-rate detailed kinetic mechanism for the combustion and ionization of H_2–air mixtures with and without potassium seeding is employed and validated through comparison to theory. The effects of ambient pressure, N_2 dilution, and potassium seeding on the electrical conductivity of the flow are investigated. These results reveal trends similar to those observed in the experimental work discussed previously but also suggest new physics that may limit the electrical conductivity from what is attainable theoretically. In the current study, only stoichiometric mixtures of H_2 and O_2 are considered.

This paper is organized as follows. In Sect. 2, the governing equations and the chemical mechanism for both combustion and ionization are discussed. Methods for computing the electrical conductivity are also presented. In Sect. 3 the affects of N_2 dilution, ambient pressure and seeding are discussed for one-dimensional detonations, and in Sect. 4 for two-dimensional simulations. Finally, Sect. 5 summarizes the results from the simulations which are listed in Table 1 for reference.

Table 1 A summary of the parameter set for the simulations used in this study

Case	Dimension	P_a (bar)	N_2 (%)	K (%)
1	1d, 2d	0.2	74.52	0.0
2	1d	0.1	0.667	0.0
3	1d	0.2	0.667	0.0
4	1d	0.4	0.667	0.0
7	1d	0.2	10.00	0.0
8	1d	0.2	30.00	0.0
9	1d	0.2	50.00	0.0
10	1d	0.2	74.52	0.01
11	1d	0.2	74.52	0.03
12	1d	0.2	30	0.05
13	1d	0.2	50	0.05
12	1d, 2d	0.2	74.52	0.05
15	1d, 2d	0.2	74.52	0.10
16	2d	0.2	74.52	0.75
17	2d	0.2	74.52	1.00
18	2d	0.2	74.52	1.25
19	2d	0.2	74.52	2.00

P_a is the ambient pressure and the percent (%) concentration of N_2 and K is per weight

2 Governing equations and chemical mechanism

The unsteady, compressible Euler equations for a reacting mixture are solved. The conservation equations for mass, momentum, energy and species are given as:

$$\frac{\partial \rho}{\partial t} + \frac{\partial}{\partial x_j}\left(\rho u_j\right) = 0 \tag{1}$$

$$\frac{\partial \rho u_i}{\partial t} + \frac{\partial}{\partial x_j}\left(\rho u_i u_j + p\delta_{ij}\right) = 0 \tag{2}$$

$$\frac{\partial \rho E}{\partial t} + \frac{\partial}{\partial x_i}\left[u_i\left(\rho E + p\right)\right] = 0 \tag{3}$$

$$\frac{\partial \rho Y_k}{\partial t} + \frac{\partial}{\partial x_i}\left(\rho u_i Y_k\right) = \dot{\omega}_k \tag{4}$$

Here ρ denotes the gas density, p the thermodynamic pressure, u_i the velocity vector, and Y_k the kth species mass fraction. The gas is assumed to be thermally perfect and therefore temperature, T, is determined from the total energy, E, and related to the pressure and density through the perfect gas equation of state. The net rate of change of the kth species, $\dot{\omega}_k$, is determined from a reduced set of reaction rates given by Tables 2 and 3. In (1)–(4) the transport terms are assumed to be negligible. As is shown later, this assumption does not affect the accuracy of the simulation since comparisons to both theory and experiments are favorable. Moreover, in the absence of boundary-layer effects, other researchers have

Table 2 Summary of the hydrogen–air combustion mechanism used in the present detonation simulations

Number	Reaction	Rate coefficients			
		A	*n*	*E*	
1	$O + H_2 \rightarrow H + OH$	5.0×10^4	2.70	6,290	
2	$H + O_2 \rightarrow O + OH$	8.3×10^{13}	0.00	14,413	
3	$H + O_2 + M_a \rightarrow HO_2 + M_a$	2.8×10^{18}	−0.90	0	
4	$H + O_2 + O_2 \rightarrow HO_2 + O_2$	3.0×10^{20}	−1.70	0	
5	$H + O_2 + H_2O \rightarrow HO_2 + H_2O$	9.38×10^{18}	−0.80	0	
6	$H + O_2 + N_2 \rightarrow HO_2 + N_2$	2.60×10^{19}	−1.20	0	
7	$H + HO_2 \rightarrow OH + OH$	1.34×10^{14}	0.00	635	
8	$OH + H_2 \rightarrow H_2O + H$	2.16×10^8	1.50	3,430	
9	$H + H_2O_2 \rightarrow HO_2 + H_2$	1.21×10^7	2.00	5,200	
10	$H + HO_2 \rightarrow O_2 + H_2$	2.80×10^{13}	0.00	1,068	
11	$HO_2 + HO_2 \rightarrow O_2 + H_2O_2$	1.30×10^{11}	0.00	−1,630	k_a
		4.20×10^{14}	0.00	12,000	k_b
12	$OH + OH + M_b \rightarrow H_2O_2 + M_b$	7.40×10^{13}	−0.40	0	k_{inf}
		2.30×10^{18}	−0.90	−1,700	k_0
13	$OH + HO_2 \rightarrow O_2 + H_2O$	2.90×10^{13}	0.00	−500	
14	$OH + H_2O_2 \rightarrow HO_2 + H_2O$	1.75×10^{12}	0.00	320	k_a
		5.80×10^{14}	0.00	9,560	k_b
15	$H + H + M_c \rightarrow H_2 + M_c$	1.00×10^{18}	−1.00	0	
16	$O + O + M_d \rightarrow O_2 + M_d$	1.20×10^{17}	−1.00	0	
17	$H + OH + M_e \rightarrow H_2O + M_e$	2.20×10^{22}	−2.00	0	
18	$O + H + M_b \rightarrow OH + M_b$	5.00×10^{17}	−1.00	0	

For the three-body reactions, M includes H_2, O_2, H, O, OH, HO_2, H_2O_2, H_2O and N_2 where the collision efficiency is unity with the exceptions: M_a does not include O_2, H_2O, or N_2, and the collision efficiencies for H_2 and H_2O in M_b are 2.4 and 6.0, in M_c are 1.7 and 7.0, in M_d are 2.4 and 15.4, and in M_e are 0.73 and 3.65, respectively.
For reactions $r11$ and $r14$, $k = k_a + k_b$, and for reaction $r12$, $k = k_{\text{inf}}[P_r/(1 + P_r)]F$ with $P_r = k_0[\text{M}]/k_{\text{inf}}$ and F as defined in [22]

shown that these transport terms have a negligible impact on the solution [24].

The governing equations are solved using a Harten –Lax–Van Leer (HLL) type approximate Riemann solver with a Monotone Upstream-Center Schemes for Conservation Laws (MUSCL) reconstruction technique to achieve second order accuracy. A hybrid upstream flux solver (HLLC/E) is used where the HLLE flux solver is used in the directions transverse to the high pressure gradients and the HLLC flux solver everywhere else [11]. The fluxes are updated using a predictor-correct central scheme resulting in second-order accuracy in time. The chemical source term system, $\dot{\omega}_k$, in (4) is obtained through time-accurate integration. Validation of this approach in a variety of applications and problems have been reported elsewhere [2,11,12].

2.1 Reaction mechanism

A combustion model developed by Petersen and Hanson [22] is used to simulate detonation in H_2/O_2–N_2 mixtures. The full hydrogen–oxygen chemistry is reduced to 18 elementary reactions and 8 primary species (H_2, O_2, OH, H, O, H_2O, HO_2, H_2O_2) and an inert species such as N_2 or Ar. The mechanism has been previously used in high-speed, high-pressure simulations of ram-accelerators and for simulating gaseous detonation of hydrogen–air mixtures [22,31]. Table 2 lists the reactions and their Arrhenius coefficients.

This hydrogen–oxygen combustion model is combined with an independent kinetic mechanism to model the ionization of the post-detonation mixture. These reactions include electron-impact ionization, electron-impact dissociation, associative ionization and charge-exchange reactions. Ionization of the secondary radical species HO_2 and H_2O_2 is neglected. The reaction coefficients for the Arrhenius rates of these elementary reactions are listed for each reaction in Table 3, along with the reference from which the data were obtained.

To model the reactions of potassium in hydrogen–oxygen mixtures a reduced mechanism of four species (KO_2, KOH, KO, K) and five elementary reactions is included. The model has been used previously to analyze the affect of alkali salts in hydrocarbon flames [26]. The ionization of potassium is modeled through a single-step reaction, $M + K = M + e^- + K^+$, where M is any third-body species [1]. The combined reaction mechanism, consisting of 26 species and 65 reactions, is then used to compute the species mass fractions of the ionized gas. The electrical conductivity can then

Table 3 Arrhenius rate coefficients for the dissociation and ionization reactions

Number	Reaction	Rate coefficients			Refs.
		A	*n*	E	
Dissociation					
19	$N_2 + M_f \rightarrow N + N + M_g$	7.0×10^{21}	−1.60	113,200	[21]
20	$N_2 + M_g \rightarrow N + N + M_g$	3.0×10^{22}	−1.60	113,200	[21]
21	$O_2 + M_h \rightarrow O + O + M_h$	2.0×10^{21}	−1.50	59,360	[21]
22	$O_2 + N \rightarrow O + O + N$	1.0×10^{22}	−1.50	59,360	[21]
23	$H_2 + M_i \rightarrow H + H + M_i$	2.2×10^{14}	0.00	48,300	[21]
24	$NO + M_f \rightarrow N + O + M_f$	5.0×10^{15}	0.00	75,500	[20]
25	$NO + M_g \rightarrow N + O + M_g$	1.1×10^{17}	0.00	75,500	[20]
Electron impact dissociation					
26	$N_2 + e \rightarrow N + N + e$	2.48×10^{-9}	6.16	113,263	[30]
27	$O_2 + e \rightarrow O + O + e$	3.47×10^{2}	3.52	59,370	[30]
28	$H_2 + e \rightarrow H + H + e$	2.69×10^{20}	−0.80	126,565	[23]
29	$H_2O + e \rightarrow H + OH + e$	3.20×10^{15}	0.50	92,832	[14]
30	$NO + e \rightarrow N + O + e$	1.05×10^{-2}	4.52	75,390	[30]
31	$OH + e \rightarrow O + H + e$	1.54×10^{20}	−0.76	80,107	[23]
Electron impact ionization					
32	$N_2 + e \rightarrow N_2^+ + e + e$	5.17×10^{12}	0.72	184,300	[30]
33	$O_2 + e \rightarrow O_2^+ + e + e$	2.20×10^{10}	1.16	130,102	[30]
34	$H_2 + e \rightarrow H_2^+ + e + e$	1.78×10^{9}	1.61	207,369	[23]
35	$H_2O + e \rightarrow H_2O^+ + e + e$	8.40×10^{15}	0.50	174,060	[14]
36	$H_2O + e \rightarrow H + OH^+ + e + e$	2.80×10^{15}	0.50	209,376	[14]
37	$NO + e \rightarrow NO^+ + e + e$	2.70×10^{10}	1.13	95,092	[30]
38	$OH + e \rightarrow OH^+ + e + e$	6.99×10^{6}	1.78	160,267	[23]
39	$N + e \rightarrow N^+ + e + e$	2.50×10^{34}	−3.82	168,600	[20]
40	$O + e \rightarrow O^+ + e + e$	3.90×10^{33}	−3.78	158,500	[20]
41	$H + e \rightarrow H^+ + e + e$	2.20×10^{30}	−2.80	157,800	[21]
Zel'dovich reactions					
42	$O_2 + N \rightarrow NO + O$	2.49×10^{9}	1.18	4,006	[6]
43	$N_2 + O \rightarrow NO + N$	5.69×10^{12}	0.42	42,938	[5]
Dissociative recombination					
44	$N + N \rightarrow N_2^+ + e$	4.40×10^{7}	1.50	67,500	[20]
45	$O + O \rightarrow O_2^+ + e$	7.10×10^{2}	2.70	80,600	[20]
46	$N + O \rightarrow NO^+ + e$	8.80×10^{8}	1.00	31,900	[20]
47	$OH^+ + e \rightarrow O + H$	3.91×10^{17}	−0.50	0	[19]
48	$H_2O^+ + e \rightarrow OH + H$	3.29×10^{18}	−0.50	0	[19]
Charge exchange					
49	$O + NO^+ \rightarrow O_2 + N^+$	1.00×10^{12}	0.50	77,200	[20]
50	$N_2 + N^+ \rightarrow N + N_2^+$	1.00×10^{12}	0.50	12,200	[20]
51	$N + O_2^+ \rightarrow O_2 + N^+$	8.70×10^{13}	0.14	28,600	[20]
52	$NO + O^+ \rightarrow O_2 + N^+$	1.40×10^{5}	1.90	15,300	[20]
53	$N_2 + O_2^+ \rightarrow O_2 + N_2^+$	9.90×10^{12}	0.00	40,700	[20]
54	$O + O_2^+ \rightarrow O_2 + O^+$	4.00×10^{12}	−0.09	18,000	[20]
55	$N + NO^+ \rightarrow N_2 + O^+$	3.40×10^{13}	−1.08	12,800	[20]
56	$O_2 + NO^+ \rightarrow NO + O_2^+$	2.40×10^{13}	0.41	32,600	[20]
57	$O + NO^+ \rightarrow N + O_2^+$	7.20×10^{12}	0.29	48,600	[20]

Table 3 continued

Number	Reaction	Rate coefficients			Refs.
		A	n	E	
58	$N_2 + O^+ \rightarrow O + N_2^+$	9.10×10^{11}	0.36	22,800	[20]
59	$N + NO^+ \rightarrow O + N_2^+$	7.20×10^{13}	0.00	35,500	[20]
Potassium reactions					
60	$K + O_2 + M \rightarrow KO_2 + M$	1.138×10^2	−2.68	596	[26]
61	$K + OH + M \rightarrow KOH + M$	1.144×10^{-1}	−2.00	0	[26]
62	$KOH + H \rightarrow K + H_2O$	2.21×10^{12}	0.50	0	[26]
63	$KO_2 + H \rightarrow KO + OH$	2.21×10^{12}	0.50	0	[26]
64	$KO + H_2O \rightarrow KOH + OH$	5.95×10^{11}	0.50	0	[26]
65	$K + M \rightarrow K^+ + e + M$	5.962×10^{15}	0.50	101,055	[1]

All collision efficiencies are unity. M_f includes N_2, O_2, H_2, NO, OH, H_2O_2, HO_2, H_2O and all ions, and M_g includes N, O, H. In order not to repeat reactions included in the combustion chemistry, M_h only includes NO and all ions, and M_i includes NO, N and all ions

be computed from the species mass fractions and the thermodynamic state.

2.2 Electrical conductivity

There are several models available to compute the electrical conductivity of an ionized gas. Most simplistically, Lin et al. [16] proposed that the electrical conductivity is given by $\sigma^{-1} = \sigma_{\text{en}}^{-1} + \sigma_{\text{ei}}^{-1}$, where σ_{en} is the electrical conductivity due to the electron–neutral collisions and σ_{ei} is due to the electron–ion collisions. The Saha equation can be used to determine the electron number density which then can be used to determine σ_{en} and theoretical equations exist for σ_{ei}. Other models are reviewed elsewhere [17].

In this work, the mixture-averaged electrical conductivity is computed from first-order approximations to the Champan–Enskog equations. Such calculations rely on the computation of the modified collision integral, $\Delta_{jk}^{(1)}$, between species j and species k. The electrical conductivity is then computed as:

$$\sigma = \frac{e^2}{kT} \frac{n_e}{\sum_{k \neq e} n_k \Delta_{ek}^{(1)}} \tag{5}$$

where e is the electrical charge, k is Boltzmann's constant and $\Delta_{jk}^{(1)}$ is given by:

$$\Delta_{jk}^{(1)} = \frac{8}{3} \left[\frac{2 W_j W_k}{\pi \hat{R} T (W_j + W_k)} \right]^{1/2} \pi \Omega_{jk}^{(1,1)} \tag{6}$$

where $\pi \Omega_{jk}^{(1,1)}$ is the collision integral of the momentum transfer between species j and species k. The number density is defined by $n_k = \rho Y_k \hat{N} / W_k$, where $\hat{N}$ is Avogadro's number and W_k is the kth-species molecular weight. Values of the collision integral between electrons and neutrals are determined either from experimental or theoretical data [28,33,34]. For electron–ion collisions, theoretical expressions are used [27].

3 Effects of pressure, N_2 dilution and K seeding

A detonation wave forms when a strong shock wave dynamically couples to a reaction-wave in such a way that a balance occurs between the release of chemical energy and the energy required to sustain the shock wave. In the simplest of models, a detonation wave is described as an one-dimensional discontinuity propagating through the mixture at the Chapman–Jouget (CJ) velocity. The theory is surprisingly well-supported. Experimental measurements are within 1–2 % of the theoretical CJ velocity [10]. As a result one-dimensional simulations can be useful in understanding the affects of N_2 dilution, pressure and seeding on the ionization of the post-detonation mixture.

The computational domain is discretized with a uniform resolution of 10 µm. This resolution is shown to be sufficient in Sect. 4. The left boundary is treated as a slip wall and at right boundary all variables are extrapolated. A direct initiation is numerically modeled by initializing a region of high pressure and temperature at the left boundary and allowing the detonation to develop naturally as the gas expands through the unburned mixture. This approach is similar to other studies reported [15]. The initiation is setup to result in a detonation with an overdrive factor close to unity where the overdrive factor, f, is defined as $(D/D_{\text{CJ}})^2$ where D is the velocity of the detonation wave and D_{CJ} is the Chapman–Jouget or CJ detonation speed. Once the detonation is initiated with the correct propagation velocity, the remainder of the simulation is then carried out in the frame of reference of the moving detonation. The boundary conditions are then changed to supersonic inflow and outflow boundaries.

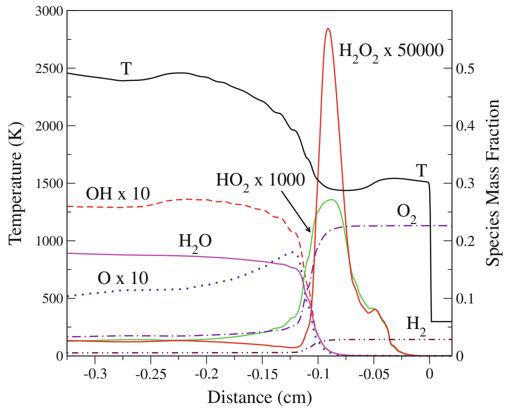

Fig. 1 One-dimensional profiles of temperature and species mass fraction directly behind the detonation-sustained shock wave. The results are shown for a stoichiometric H_2–air detonation in an ambient pressure and temperature of 0.2 bar and 298 K, respectively

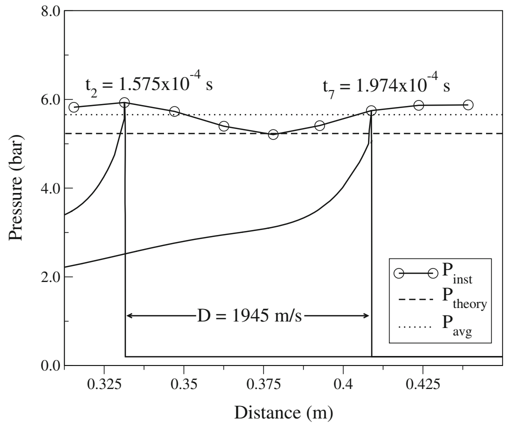

Fig. 2 One-dimensional profiles of pressure shown at two instances in time as the detonation propagates through the domain. The peak pressures oscillate indicating the detonation is in the oscillatory regime [9]. Both results are shown for a stoichiometric H_2–air detonation in an ambient pressure and temperature of 0.2 bar and 298 K, respectively

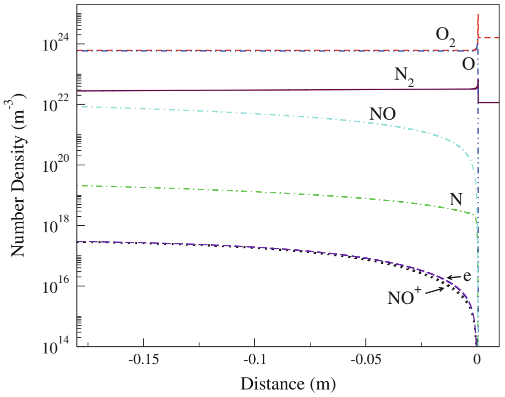

Fig. 3 One-dimensional profiles the species number density showing the important role of NO formation in the ionization process

In the following discussion, the baseline results for a stoichiometric detonation of H_2–air at an ambient pressure of 0.2 bar and temperature of 298 K are first presented followed by parametric studies where the pressure, dilution and seeding percentage are varied with respect to the baseline.

Figure 1 shows profiles of temperature and mass fractions of a few species just downstream of the detonation front. The initial sharp rise in the temperature is a result of the propagating shock wave ($M_s = 4.76$). The temperature ratio across the shock is 5.17 and compares reasonably well to the theoretical value of 5.32. The difference is attributed to the instability of the detonation, which is illustrated in Fig. 2. The average peak pressure is only slightly over-predicted. Following the shock wave, radicals are formed in the induction zone as the reactants, H_2 and O_2, begin to break-down. The sharp increase in the radicals H_2O_2 and HO_2 marks the beginning of heat release. As the temperature increases downstream (with N_2/O_2 and ionization chemistry), N_2 begins to break down, and the presence of N atoms prompts the Zel'dovich reactions and the beginning of NO formation.

Since NO has a low ionization potential, the electrical conductivity is directly dependent on the formation of NO ions [8]. This is demonstrated by computing the species number densities, which are shown in Fig. 3. Since the ionized mixture is assumed to be quasi-neutral, the electron number density, n_e, must be equal to the positive ion number density. Here $n_e = 3.052 \times 10^{17}\ \text{m}^{-3}$ and $n_{\text{NO}^+} = 2.956 \times 10^{17}\ \text{m}^{-3}$. From (5), the electrical conductivity is seen to be directly proportional to n_e. Thus the formation of NO ions is critical to increasing the electrical conductivity of the mixture. Even though both OH and NO are easily ionizable, the production of NO ions dominates. This is because the concentration of OH is depleted downstream due to formation of H_2O resulting in a negligible contribution to the n_e by OH ion production ($n_{\text{OH}^+} = 21.33\ \text{m}^{-3}$). Non-stoichiometric H_2/O_2 detonations could possibly reveal OH ionization to be of more significance.

As the ambient pressure increases, the formation of NO occurs earlier and its equilibrium value increases slightly. This in turn increases the electrical conductivity. The trend is easily observable in the profiles of the electrical conductivity shown in Fig. 4. Similarly, as the dilution of the N_2 is reduced, the electrical conductivity also increases as shown in Fig. 5. Both effects are largely a result of the change

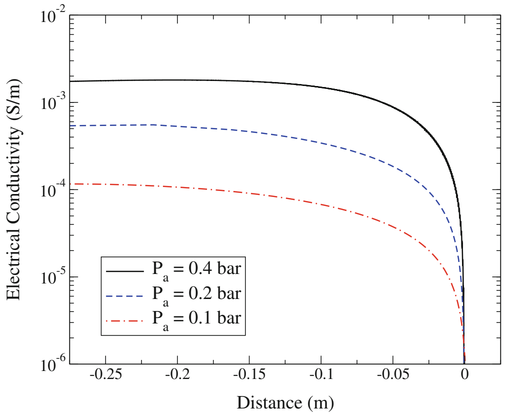

Fig. 4 One-dimensional profiles of the electrical conductivity computed for a stoichiometric H_2/O_2 mixture with 0.667 % N_2 dilution at three different ambient pressures

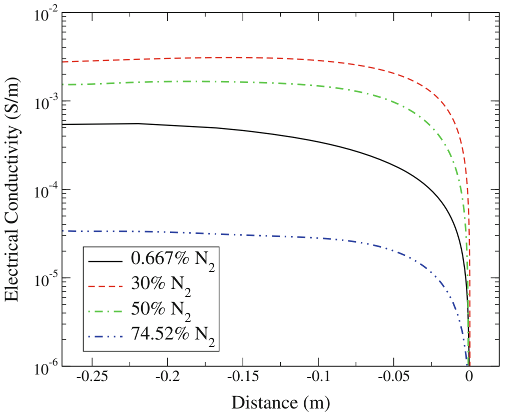

Fig. 5 A comparison of the electrical conductivity at different N_2 dilutions. The peak post-detonation temperature for 0.667, 30, 50, and 79 % N_2 dilution is 3408, 3265, 3180, 2751 K, respectively

in the post-detonation temperature. As the ambient pressure is increased from 0.1 to 0.4 bar, the detonation velocity increases roughly 2.75 % with a corresponding 6.7 % rise in temperature. This increases the reaction rates in the post-detonation mixture and thus increases NO formation. Also as the temperature is increased, N_2 is more easily dissociated. Similar logic applies to why the electrical conductivity increases at lower N_2 concentrations. The reduction of N_2 reduces the heat capacity of the mixture and thus increases the detonation velocity and post-detonation temperature. However, as observed in Fig. 5, the trend reverses at low concentrations regardless of the higher post-detonation temperatures since the reduction of N_2 limits NO production because of the lack of available nitrogen.

As mentioned previously, detonations in H_2–air mixtures produce ionized mixtures with low electrical conductivities of order 10^{-3} S m^{-1}. In order to increase these values potassium can be used to seed the gas with easily ionizable particles. In experiments, potassium is typically injected into the flow as atomized salt particles such as potassium carbonate. These particles quickly decompose and undergo phase change [26]. However, to simplify the current study the phase change process is not modeled and gaseous KOH is injected uniformly at the inflow plane instead. The injected KOH then convects until it reacts at the detonation front due to the elevated temperatures and pressures as well as the presence of H and OH radicals. Gaseous potassium quickly forms which ionizes and increases the electron number density of the mixture. Figure 6 shows the electrical conductivity for potassium seedings of 0.01, 0.03 and 0.05 % by weight. The electrical conductivity not only increases at a faster rate but is 4 orders of magnitude larger than the electrical conductivity of the unseeded detonation.

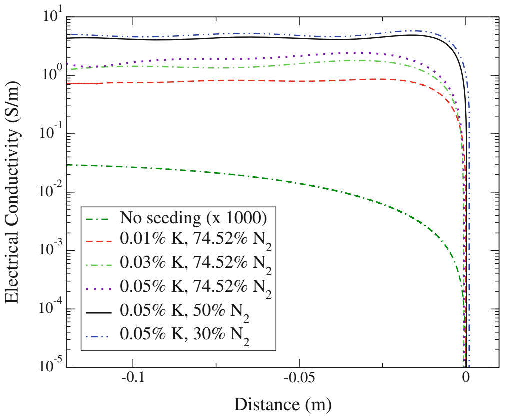

Fig. 6 A comparison of the electrical conductivity at different potassium seeding percentages. The reference case for detonation of a stoichiometric H_2–air mixture at ambient pressure and temperature of 0.2 bar and 298 K is shown for comparison

In the one-dimensional studies conducted, a potassium seeding of larger than 0.06 % was observed to kill the detonation as demonstrated in Fig. 7. This is a result of the potassium chemistry competing for the O and H radicals necessary for combustion. This disruption increases the induction time for combustion which subsequently causes the heat release zone to decouple from the shock wave triggering a reduction in the heat release such that the propagating shock can no longer be sustained. This process is observable in the pressure profiles shown in Fig. 7. The detonation profiles following the addition of the seed are shown approximately every 20 μs.

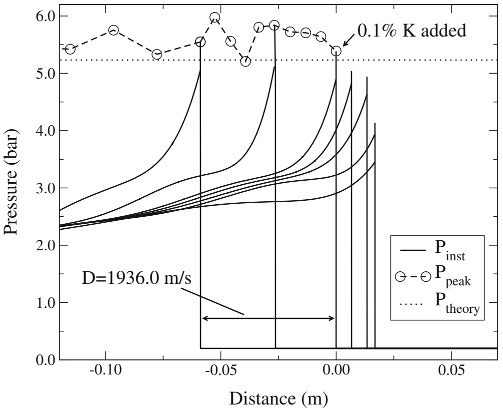

Fig. 7 At seeding percentages higher than 0.06 % K the detonation wave decays into a propagating shock wave

The peak pressures as well as the CJ peak pressure are shown prior to the seeding as reference.

This result is in some contradiction to experiments which use higher seeding percentages [4,17]. Yet this is expected since in one-dimension the detonation lacks the structure necessary for self-propagation and therefore is more sensitive to the disruptions caused by seeding. This does not, however, invalidate the conclusions drawn from these simulations. While in two and three dimensions the detonation may be more impervious to potassium seeding, a critical point most likely exists where too much seeding results in a failure of the detonation. This is investigated in the next section.

4 Potassium seeding in two-dimensional detonation simulations

A two-dimensional stoichiometric hydrogen–air detonation is simulated by initializing the domain with a one-dimensional solution. As in the one-dimensional simulations, the detonation is simulated in the frame of reference moving with the detonation wave. The boundaries in the y-direction are taken as periodic, and a simulation domain of 18 mm × 3 mm is used. From a grid-resolution study, a 10-µm resolution is determined to be sufficient to resolve the Mach stem, incident shock and transverse wave interactions at the detonation front. This interaction is critical in sustaining the detonation as it creates local zones of high pressure and temperature causing the detonation front to pulsate in the direction of propagation. This introduces fluid mixing

Fig. 8 Contours of temperature and electrical conductivity for a stoichiometric H_2–air detonation at an ambient temperature and pressure of 298 K and 0.2 atm. The length scale shown is in millimeters

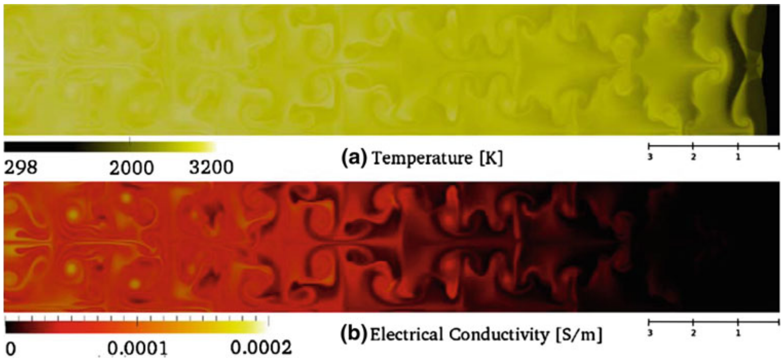

Fig. 9 Contours of temperature and electrical conductivity for a stoichiometric H_2–air detonation at an ambient temperature and pressure of 298 K and 0.2 atm seeded with 1 % K by weight. The length scale shown is in millimeters

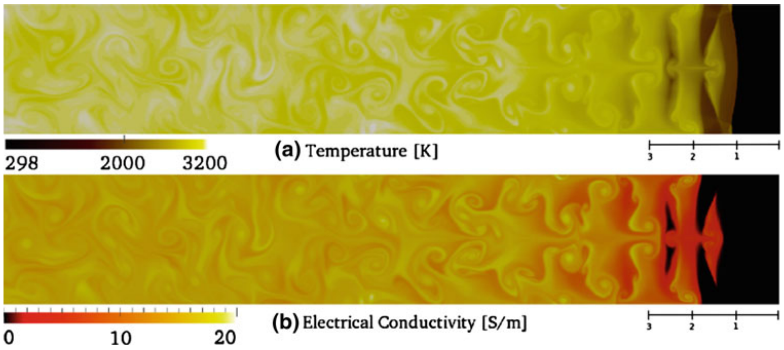

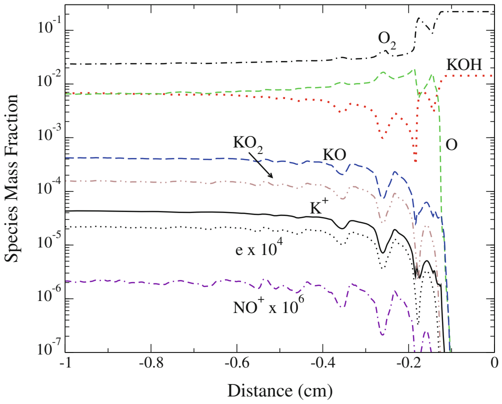

Fig. 10 Planar averaged mass fractions of the species involved in potassium ionization behind the detonation front with 1 % K seeding

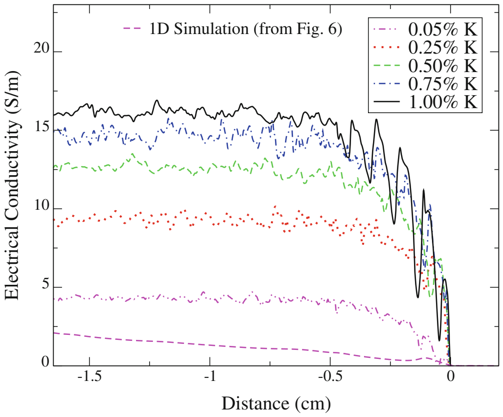

Fig. 11 Planar averaged profiles of the electrical conductivity for various potassium seeding percentages. For the case with 0.05 % potassium seeding, the one-dimensional solution for the electrical conductivity is shown for comparison

time-scales which impact the electrical conductivity in the post-detonation mixture (Figs. 8, 9).

Since the location of the transverse wave, incident shock and Mach stem interaction oscillates perpendicularly to the detonation front a series of vortical structures separated by slip lines are propagated downstream creating a non-uniform distribution of temperature and species mass fraction as illustrated in Fig. 8. Only in the regions of high temperature does significant dissociation of N_2 and NO formation occur. As the vortices interact and merge, the high temperature regions become less distinct and the ion density becomes more uniform. As a result, the distance between the weakly ionized plasma and the detonation front is both a result of the mixing rate of the vortices and the chemical non-equilibrium of the explosion products. This creates a non-uniform distribution of the electrical conductivity with peak values of order 10^{-3} S m^{-1}, which are similar to those observed in the one-dimensional simulations.

When KOH is injected into the inflow, the ionization mechanism becomes dominated by the potassium chemistry. The ionization is now prompt, occurring at the detonation front, and is no longer rate-limited by the slow formation of NO (Figs. 10, 11). This could have important consequences in applications where an external magnetic field is present since a combination of a high electrical conductivity at the detonation front and a strong magnetic field could alter the way the transverse waves interact at the detonation front.

The main difference from the one-dimensional and two-dimensional simulations is that the strong interaction between the Mach stem, incident shock and transverse waves at the detonation front creates local regions of high temperature and pressure. These regions of heat release allow for the two-dimensional detonation to sustain higher mass fractions of potassium seeding. Yet above a seeding of 1.25 % by weight

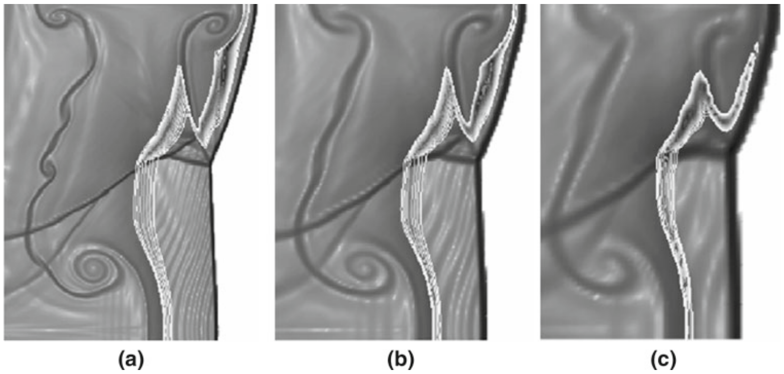

Fig. 12 Contours of the $\ln(|\nabla\rho| + 1)$ and of the mass fraction of H_2O_2 (in *white*) delineate the prominent features of gaseous detonations. The grid resolution is varied from **a** 5 µm, **b** 10 µm and **c** 20 µm to determine the minimum grid resolution required

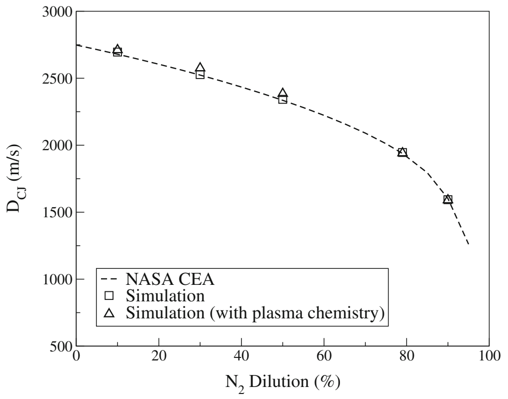

Fig. 13 The detonation velocity is computed for detonation in a H_2–O_2/N_2 mixture with an ambient pressure and temperature of 0.2 bar and 298 K, respectively. The values are compared to the theoretical detonation velocity (D_{CJ}) obtained from NASA's CEA code

of K, the detonation becomes unstable and decays into a propagating shock wave. This indicates that the ionization fraction of the gas mixture that can be achieved through detonation is limited. This constraint is imposed along with the additional problems of uniform mixing and burning of the seed particles. Extending these conclusions to three dimensions, some increase in the seeding limit could be hypothesized since in three dimensions the nature of the shock-wave interactions will result in higher peak pressures and temperatures [13].

5 Conclusions

The electrical conductivity of a plasma produced by a hydrogen–air detonation is computed. The proposed detailed chemistry is able to model both hydrogen–oxygen combustion and ionization in hydrogen–air mixtures. Basic detonation properties, such as D_{CJ}, are reproducible at various pressures and N_2 dilutions indicating that the numerical approach is both robust and accurate. For unseeded detonations, ionization is slower as a result of the relatively slow formation of NO. At higher ambient pressures, the post-detonation temperature is increased resulting in an increase in the electrical conductivity. Reducing the N_2 dilution also increases the post-detonation temperature and the electrical conductivity until the reduction of nitrogen in the mixture begins to limit NO production. Since the observed electrical conductivities in unseeded detonations are too low for MHD devices to be efficient, seeding the mixture with low ionization potential alkali salts is necessary. While seeding does increase the electrical conductivity, simulations in both one and two dimensions show that the detonation is sensitive to the amount of seeding material injected into the flow. Too high of a seeding percentage can adversely affect the detonation propagation, however, even at lower seeding percentages (less than 1.25 %) a 4–5 order of magnitude increase in the electrical conductivity is observed.

Acknowledgments This work is supported by the Defense Threat Reduction Agency. Computational resources were provided by DOD HPC Centers at ERDC, ARL and NAVO.

Appendix A: Grid-resolution study

A grid-resolution study is performed to determine the required resolution, which is determined by the ability to resolve the interaction between the Mach stem, incident shock and transverse waves [25]. The interaction is critical in sustaining the detonation as it creates a zone of high pressure and temperature that causes the gas to expand as chemical energy is released. Figure 12 shows the shock structures formed behind the detonation front for half of the channel at three different resolutions: 5, 10 and 20 µm. At the highest resolution, the incident shock, Mach stem and the transverse shock are clearly defined as well as are the slip-lines. Overlaid on these figures in white are the contour lines of the mass fraction of the H_2O_2 radical, which indicates the region of heat release. In comparison to Fig. 12a, b, the detonation features in Fig. 12c are not clear, indicating that a resolution of 20 µm is inadequate. Hence, a uniform resolution of 10 µm is used in the remainder of the studies.

Appendix B: Chemical mechanism validation

The combined model for both hydrogen–air detonation and the subsequent ionization consists of 26 species and 65 reactions and is described by Tables 2 and 3. From experimental analysis [8], the ionization of NO is the primary pathway for ionization in hydrogen–air mixtures. Thus, modeling of the N_2/O_2 chemistry is most important in non-seeded mixtures, however, for completeness ionization reactions involving all of the hydrogenous species are included whenever reliable data could be found. The N_2/O_2 chemistry relies heavily on the reaction mechanism developed by Park et al. [20,21], which is widely used with slight modifications in a variety of applications. The electron impact dissociation and ionization reactions are taken from the data collected by Teulet et al. [30] and Riahi et al. [23]. All reactions are taken as reversible.

This kinetic model is verified by comparison to theoretical values of the detonation velocity and to equilibrium values of the electrical conductivity. The theoretical value of the detonation velocity, D_{CJ}, is computed using NASA's Chemical Equilibrium with Applications (CEA) code [18]. The percent of N_2 in the H_2/O_2 mixture is varied and for each

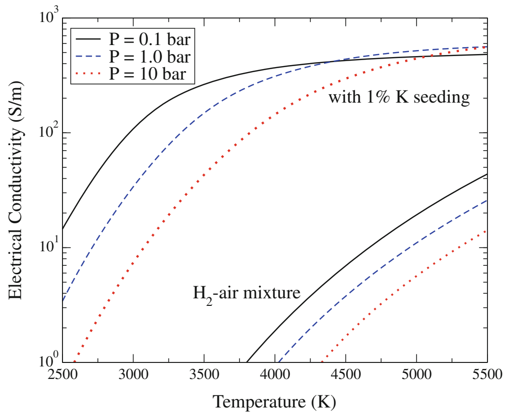

Fig. 14 The equilibrium electrical conductivity is shown as a function of pressure and temperature for a stoichiometric H_2–air mixture

mixture the detonation velocity is calculated using the proposed kinetic mechanisms. The addition of ionization chemistry should not change the overall detonation parameters. For one, N_2/O_2 and ionization chemistry occurs mostly downstream so it does not affect the chemical thermicity at the detonation front, and two, the inclusion of the N_2/O_2 and ionization chemistry is actually more accurate with the 18-step and 21-reaction H_2/O_2 model being merely a subset. Regardless, the values from the one-dimensional simulations are within 3–5 % of the theoretical values for the range of N_2 dilution considered. As shown in Fig. 13, both mechanisms are good at predicting the proper detonation parameters.

The electrical conductivity of a stoichiometric mixture of hydrogen and air is computed for various temperatures and pressures using (5). The species mass fractions at equilibrium are determined by integrating in time the conservation of mass, species and energy equations under the assumption of constant pressure. Once the equilibrium species mass fractions are determined, the electrical conductivity is computed. A similar calculation is done with the addition of 1 % potassium by weight. The results are shown in Fig. 14. The values are similar to those reported elsewhere in the literature [17].

References

1. Ashton, A.F., Hayhurst, A.N.: Kinetics of collisional ionization of alkali metal atoms and recombination of electrons with alkali metal ions in flames. Comb. Flame **21**(1), 69–75 (1973)
2. Balakrishnan, K., Nance, D.V., Menon, S.: Numerical study of blast characteristics from detonation of homogenous explosives. Shock Waves **20**, 147–162 (2010)
3. Basu, S., Fay, J.: Ionization in detonation waves. Int. Symp. Combust. **7**(1), 277–282 (1958)
4. Basu, S.: Ionization in seeded detonation waves. Phys. Fluids **3**(3), 456–463 (1960)
5. Bose, D., Candler, G.V.: Thermal rate constants of the N_2 + O → NO + N reaction using ab initio $^3A''$ and $^3A'$ potential energy surfaces. J. Chem. Phys. **104**(8), 2825–2833 (1996)
6. Bose, D., Candler, G.V.: Thermal rate constants of the O_2 + N → NO + O reaction using ab initio $^2A'$ and $^4A'$ potential-energy surfaces. J. Chem. Phys. **107**(16), 6145–6163 (1997)
7. Cambier, J.-L.: MHD power extraction from a pulse detonation engine. In: 34th AIAA/ASME/SAE/ASEE Joint Propulsion Conference and Exhibit, AIAA-1998-3876, Cleveland, OH (1998)
8. Edwards, D.H., Hooper, G., Collyer, A.A.: Ionization measurement in reactive shock and detonation waves using microwave techniques. J. Phys. D Appl. Phys. **4**, 854–870 (1971)
9. Fedorov, A.V., Tropin, D.A., Bedarev, I.A.: Mathematical modeling of detonation suppression in a hydrogen-oxygen mixture by inert particles. Comb. Exp. Shock Waves **46**(3), 332–343 (2010)
10. Fickett, W., Davis, W.C.: Detonation. University of California Press (1979)
11. Génin, F., Menon, S.: Dynamics of sonic jet injection into supersonic crossflow. J. Turbulence **11**(4), 1–30 (2010)
12. Génin, F., Menon, S.: Studies of shock/turbulence shear layer interaction using large-eddy simulation. Comp. Fluids **39**, 800–819 (2010)
13. Gottiparthi, K.C., Menon, S.: A study of interaction of clouds of inert particles with detonation in gases. Comb. Sci. Tech. **184**(3), 406–433 (2012)
14. Konstantinovskii, R.S., Shibkov, V.M., Shibkova, L.V.: Effect of a gas discharge on the ignition in the hydrogen-oxygen system. Kinetics Catal. **46**(6), 775–788 (2005)
15. Lee, J.H.S., Higgins, A.J.: Comments on criteria for direct initiation of detonation. Phil. Trans. R. Soc. Lond. A **357**, 3503–3521 (1999)
16. Lin, S.C., Resler, E.L., Kantrowitz, A.: Electrical conductivity of highly ionized argon produced by shock waves. J. Appl. Phys. **26**, 95–109 (1955)
17. Lu, F.K., Liu, H.-C., Wilson, D.R.: Electrical conductivity channel for a shock tube. Meas. Sci. Tech. **16**, 1730–1740 (2005)
18. McBride, B.J., Gordon, S.: Computer program for calculating and fitting thermodynamic functions. NASA-RP-1271 (1992)
19. Mitchell, J.B.A.: The dissociation recombination of molecules. Phys. Rep. **186**, 216–248 (1990)
20. Park, C.: Review of chemical-kinetic problems of future NASA missions, I: Earth entries. J. Therm. Heat Trans. **7**, 385–398 (1993)
21. Park, C., Jaffe, R.L., Partridge, H.: Chemical-kinetic parameters of hyperbolic Earth entry. J. Therm. Heat Trans. **15**(1), 76–90 (2001)
22. Petersen, E.L., Hanson, R.K.: Reduced kinetic mechanisms for ram accelerator combustion. J. Propul. Power **4**(15), 591–600 (1999)
23. Riahi, R., Teulet, Ph, Lakhdar, Z.B., Gleizes, A.: Cross-section and rate coefficient calculate for electron impact excitation, ionisation and dissociation of H_2 and OH molecules. Eur. Phys. J. D **40**, 223–230 (2006)
24. Shepherd, J.E.: Detonation in gases. Proc. Combust. Inst. **32**, 83–98 (2009)
25. Sharpe, G.J.: Transverse waves in numerical simulations of cellular detonations. J. Fluid Mech. **447**, 31–51 (2001)
26. Slack, M., Cox, J.W., Grillo, A., Ryan, R.: Potassium kinetics in heavily seeded atmospheric pressure laminar methane flames. Comb. Flame **77**, 311–320 (1989)
27. Stallcop, J.R., Partridge, H., Levin, E.: Collision integrals for the interaction of the ions of nitrogen and oxygen in a plasma at high temperatures and pressures. Phys. Fluids B **4**, 386–391 (1992)
28. Stefanov, B., Zarkova, L.: Electron-potassium-atom momentum transfer cross section: fit to the experimental data. J. Phys. B: Atmos. Mol. Phys. **20**, 2281–2289 (1987)
29. Tasker, D.G., Whitley, V.H., Mace, J.L., Pemberton, S.J., Sandoval, T.D., Lee, R.J.: Electromagnetic effects on explosive reaction and

plasma. In: Proceedings of the 14th International Detonation Symposium, Coeur d'Alene Resort, Idaho (2010)

30. Teulet, Ph, Sarrette, J.P., Gomes, A.M.: Calculation of electron impact inelastic cross sections and rate coefficients for diatomic molecules. Applications to air molecules. J. Quant. Spec. Rad. Transfer **62**, 549–569 (1999)
31. Tsuboi, N., Katoh, S., Hayashi, K.: Three-dimensional numerical simulation for hydrogen/air detonation: rectangular and diagonal structures. Proc. Combust. Inst. **29**(2), 2783–2788 (2002)
32. Wang, X., Ye, D., Gu, F.: Research on the thermal ionization model of detonation products by quantum mechanics methods. Comb. Expl. Shock Waves **44**(1), 101–109 (2008)
33. Wright, M.J., Bose, D., Palmer, G.E., Levin, E.: Recommended collision integrals for transport property computations, part 1: air species. AIAA J. **43**(12), 2558–2564 (2005)
34. Yousfi, M., Benabdessadok, M.D.: Boltzmann equation analysis of electron-molecule collision cross sections in water vapor and ammonia. J. Appl. Phys. **80**(12), 6619–6630 (1996)

PHYSICS OF FLUIDS **25**, 114105 (2013)

Richtmyer-Meshkov instability in dilute gas-particle mixtures with re-shock

J. C. Schulz, K. C. Gottiparthi, and S. Menon
School of Aerospace Engineering, Georgia Institute of Technology, Atlanta, Georgia 30332, USA

(Received 17 August 2013; accepted 28 October 2013; published online 13 November 2013)

The Richtmyer-Meshkov instability (RMI) is investigated in a dilute gas-particle mixture using three-dimensional numerical simulations. This work extends an earlier two-dimensional study [S. Ukai, K. Balakrishnan, and S. Menon, "On Richtmyer-Meshkov instability in dilute gas-particle mixtures," Phys. Fluids **22**, 104103 (2010)] to a larger parameter space consisting of variations in the mass loading and the particle size as well as considering both single-mode and multi-mode interface initializations. In addition, the effect of the presence of particles on re-shock RMI is also investigated. Single-phase numerical predictions of the mixing layer growth-rate are shown to compare well to both experimental and theoretical results. In a dilute gas-particle mixture, the initial growth-rate of RMI shows similar trends compared to previous work; however, the current numerical predictions show that there is an observable increase, not previously predicted, in the growth of the mixing layer at higher mass loadings. For the range of cases considered, an increase as much as 56% is observed. This increase is attributed to additional vorticity production in the mixing layer resulting from inter-phase momentum coupling. Moreover, the presence of particles introduces a continuous drag on the gas-phase resulting in a delay in the time at which re-shock occurs. This delay, which is observed to be as much as 6%, is largest for higher initial mass loadings and smaller particle radii and has a corresponding effect on both the growth-rate of the mixing-layer after re-shock and the final width of the mixing layer. A new semi-analytical correlation is developed and verified against the numerical data to predict the re-shocked RMI growth-rate in dilute gas-particle flows. The correlation shows that the re-shock RMI growth-rate is linearly proportional to the velocity jump at re-shock, the molecular mixing fraction, and the multi-phase Atwood number. Depending on the initial mass loading and particle radii, the re-shock RMI growth-rates were observed to be reduced by as much as 48% in some cases with variations of around 26% in the width of the mixing layer after re-shock.
© *2013 AIP Publishing LLC*. [http://dx.doi.org/10.1063/1.4829761]

I. INTRODUCTION

The Richtmyer-Meshkov instability (RMI) develops when a shock wave accelerates an initially perturbed interface between two fluids of different properties. During shock refraction, a misalignment between the density and pressure gradients causes vorticity generation by baroclinic torque along the interface. This unstable vortex sheet drives the amplification of the initial perturbations which can be characterized either by a sinusoidal function of a given wavelength and amplitude (i.e., single-mode RMI) or a superposition of these perturbations (i.e., multi-mode RMI).[1] Additional instabilities, such as the Kelvin-Helmholtz instability, result in vortex roll-up and an increase in the growth of the mixing layer. Furthermore, possible secondary shocks impacting the evolving mixing layer can substantially amplify the mixing processes[2] and quicken the transition of the layer to a fully turbulent mixing zone.

RMI is a fundamental fluid instability ubiquitous in both nature and engineering. Thus it is the topic of much experimental, analytical, and computational study.[1] The first of such analysis

This article is copyrighted as indicated in the article. Reuse of AIP content is subject to the terms at: http://scitation.aip.org/termsconditions. Downloaded to IP: 143.215.48.65 On: Tue, 31 Dec 2013 19:32:03

was by Richtmyer,[3] who treated the RMI as the impulsive limit of the Rayleigh-Taylor instability and was able to show that the interface amplitude grows linearly in time. Experiments[4–6] show good agreement with the impulsive formulation; however, as the interface amplitude increases to roughly a tenth of the perturbation wavelength,[1] the RMI transitions to nonlinear growth, and the linear theory is no longer valid. This phase of the instability is often described as having "bubbles" rising into the heavier fluid and "spikes" falling into the lighter fluid. Several nonlinear models have been developed to predict the bubble/spike velocities and the subsequent reduction in growth of the interface width from mode saturation.[7–9] Such models show good agreement to two- and three-dimensional numerical simulations.[2]

In realistic applications, however, the initial interface is more accurately quantified as a superposition of perturbations spanning a large range of amplitudes and wavelengths. In this case, the RMI quickly transitions to nonlinear growth following a self-similar power-law dependence with time, $h \approx t^{\theta}$, where h is the peak-to-valley amplitude with values of θ ranging from 0.2 to 1.0. The exact value of θ is an on-going topic of discussion.[1,10,11] Assuming that the just-saturated mode dominates the mixing dynamics, Dimonte *et al.*[12] determine the overall growth of the mixing layer to have a growth exponential of $\theta \approx 0.5$. Modifications to include the effects of initial conditions, however, show that the growth from mode-coupling alone results in $\theta = 0.24$, concluding that any measured growth-rate larger than that must be dependent on the initial conditions.[13] Recent experiments[14–16] and other analytical models[17–19] show similar discrepancies complicating the understanding of the driving factors in the RMI growth-rate. In addition, several computational studies have attempted to better understand how the RMI growth-rate depends on a number of factors including the initial multi-mode perturbations,[13] the impulse strength,[5,20,21] and the fluid composition.[22]

Re-shock RMI occurs when a second shock perturbs the already evolving interface. All experiments indicate that this second impulse results in a significant increase in the mixing layer growth-rate.[11,23–25] Yet, once again there is some discrepancy in determining functional relationship of the re-shocked RMI growth-rate. In the experiments by Leinov *et al.*[24] and Vetter and Sturtevant,[25] the re-shock growth is observed to be linear in time ($\theta = 1$) and is proportional to the velocity jump at the re-shock interface. This is consistent with theoretical predictions,[11,26,27] numerical parametric studies,[2] and several computational studies[28–30] of the experiments by Vetter and Sturtevant,[25] all of which show a linear growth-rate after re-shock. Only at very late times is there an indication of mode saturation and nonlinear growth. Yet, experiments by Houas and Chemouni[31] show a growth exponential somewhere between $\theta = 2/3$ and $\theta = 1.0$, and in the gas-curtain experiments of Balakumar *et al.*[23] and the corresponding computational simulations of Gowardhan and Grinstein,[32] the re-shock growth is much more nonlinear. Thornber *et al.*[33] have proposed to reconcile these differences by modifying the linear model of Mikaelian[34] to depend on the molecular mixing fraction. An extension of this model to two-phase flows is discussed in this work.

As summarized above, much of the focus on RMI has been on the development of the instability in single-phase media within the parameter space encompassing three parameters: the scales and type of initial perturbations, the impulse strength, and the fluid composition. In many applications, such as in chemical explosions with burning metal particles[35] or in astrophysical dusty plasmas,[36] the instability develops in a highly complex multi-phase environment. Earlier studies[37,38] have addressed some of these aspects using numerical simulations. For example, Balakrishnan and Menon[38] have proposed a multi-phase buoyancy-drag model for both the RMI and the Rayleigh-Taylor instability by extending the work of Srebro[39] to dilute gas-particle mixtures. Using this model, the authors calculate the RMI growth-rate for both single-mode (SM) and multi-mode (MM) initial perturbations and show a reduction in the RMI growth for increases in the mass loading. The model has certain limitations, however, such as the assumption that the particles are always in equilibrium with the gas. Thus, the momentum and energy coupling between the two phases is neglected. This assumption is relaxed in this study.

Also in a previous study, Ukai *et al.*[37] derive a linear impulsive model for the growth-rate of the single-mode RMI in a dilute gas under the assumption of small Stokes number, St, which is defined as the ratio of the time scale of the flow (τ) to that of the particle field (τ_p). In the range of the model's validity, the model compares reasonably well to two-dimensional numerical simulations showing a similar dependence on mass loading as predicted by the buoyancy-drag model of Balakrishnan

This article is copyrighted as indicated in the article. Reuse of AIP content is subject to the terms at: http://scitation.aip.org/termsconditions. Downloaded to IP: 143.215.48.65 On: Tue, 31 Dec 2013 19:32:03

and Menon.[38] For St > 0.01, however, the model is less accurate in comparison with the numerical simulations where the simulation results seem to indicate a reversal in trend, i.e., high mass loadings resulting in larger growth-rates. A possible reason for this reversal in trend is explained in this work. Moreover, since impulsive models are only valid within the linear growth regime of the RMI and thus only applicable to small amplitude single-mode perturbations during early times, prior work leaves it unclear how the presence of particles might affect the nonlinear processes of the RMI, particularly since after re-shock such processes accelerate mixing. More importantly, both the linear impulsive model and the buoyancy-drag model implicitly assume that the gas-particle mixture is in equilibrium, and thus they cannot account for any coupling between the phases. The three-dimensional numerical simulations discussed in the current work seek to explain in a more rigorous manner how the RMI evolves in a two-phase flow before and after re-shock. To do this, studies based on prior single-phase re-shock RMI simulations[2,28–30] are used to extend the previous analysis of two-dimensional single-mode RMI in dilute-gas mixtures.[37,38] By analyzing a wide range of initial Stokes numbers and particle number densities, a previously unobserved increase in the initial two-phase RMI growth-rate is explained. Additionally, a new model for the re-shock RMI growth-rate in a dilute gas-particle mixture is introduced that correlates well with the numerical predictions.

This paper is organized as follows. Section II presents an overview of the numerical formulation for the gas and particle phases. Section III introduces the simulation methodology, presents a brief validation of gas-phase re-shock simulations, and introduces the multi-phase setup and initialization. The results of the multi-phase numerical simulations are discussed in Sec. IV. Finally, this study concludes with a summary of the key observations and a discussion of future work.

II. NUMERICAL FORMULATION

A. Gas phase

The compressible Navier-Stokes equations for multi-species and multi-phase flow in the limit of negligible volume fraction (i.e., a dilute gas-particle mixture) are

$$\frac{\partial \rho}{\partial t} + \frac{\partial \rho u_i}{\partial x_i} = 0, \tag{1}$$

$$\frac{\partial \rho u_i}{\partial t} + \frac{\partial}{\partial x_j}\left(\rho u_i u_j + p\delta_{ij} - \tau_{ij}\right) = \dot{F}_{p,i}, \tag{2}$$

$$\frac{\partial \rho E}{\partial t} + \frac{\partial}{\partial x_i}\left[(\rho E + p)u_i + q_i - u_j\tau_{ij}\right] = \dot{Q}_p + \dot{W}_p, \tag{3}$$

$$\frac{\partial \rho Y_k}{\partial t} + \frac{\partial}{\partial x_i}\left[\rho Y_k\left(u_i + V_{i,k}\right)\right] = 0. \tag{4}$$

In the above equations, ρ is the gas density, u_i is the velocity vector, E is the total specify energy, and Y_k is the kth species mass fractions. In the current RMI simulations, only two species are considered, one with a small molecular weight, W_1, referred to as the light species, and one with a larger molecular weight, W_2, referred to as the heavy species. The thermodynamic pressure, p, is computed using the perfect gas equation of state, $p = \rho R T$, where T is the temperature of the gas phase and R is the mixture-averaged gas constant. The viscous terms, τ_{ij}, q_i, and $V_{i,k}$, are the shear-stress tensor, the rate of heat transfer, and the kth species diffusion flux, respectively. They are given as

$$\tau_{ij} = \mu\left(\frac{\partial u_i}{\partial x_j} + \frac{\partial u_j}{\partial x_i}\right) + \delta_{ij}\lambda\frac{\partial u_m}{\partial x_m}, \tag{5}$$

$$q_i = -\kappa\frac{\partial T}{\partial x_i} + \rho\sum_{k=1}^{2} h_k Y_k V_{i,k}, \tag{6}$$

$$V_{i,k} = -\frac{D_k}{Y_k}\frac{W_k}{\overline{W}}\left(\frac{\partial X_k}{\partial x_i}\right), \tag{7}$$

This article is copyrighted as indicated in the article. Reuse of AIP content is subject to the terms at: http://scitation.aip.org/termsconditions. Downloaded to IP: 143.215.48.65 On: Tue, 31 Dec 2013 19:32:03

where μ is the mixture-averaged viscosity, δ_{ij} is the Kronecker delta function, λ $(= -2/3\mu)$ is the bulk viscosity, κ is the mixture-averaged thermal conductivity of the gas phase, $\overline{W}$ is the mixture-average molecular weight, and h_k, X_k, and D_k are, respectively, the specific enthalpy, the mole fraction, and the mixture-averaged diffusion coefficient of the kth species. The transport properties for each species are computed using curve-fits as a function of the gas temperature.[40,41] The interphase coupling terms, $\dot{F}_{p,i}$, $\dot{W}_p$, and $\dot{Q}_p$, in the conservation equations are the rates of momentum, work, and heat transfers resulting from the presence of particles in the two-phase mixture. These terms are discussed further in Sec. II B.

The governing equations are solved numerically using a second-order predictor-corrector finite-volume scheme where the cell-surface fluxes are computed using a hybrid upwind-central scheme. In the vicinity of flow discontinuities, shocks or density gradients, the fluxes are computed using a Harten-Lax-Van Leer (HLL) type approximate Riemann solver with Monotone Upstream-Center Schemes for Conservation Laws (MUSCL) reconstruction. A second-order central scheme is used elsewhere. The hybrid switch is based on a sensor that detects the curvature of the pressure and density fields. More information about the numerical scheme can be found in previous work.[40,41]

B. Particle phase

Lagrangian tracking is used to compute the particle position, $x_{p,i}$, the particle velocity, $u_{p,i}$, and the particle temperature, T_p. In scenarios where the number of particles is too large for Lagrangian tracking to be computationally feasible, the parcel method[42,43] can be used. A parcel is a group of one or more particles that all have the same position, velocity, and temperature. The approach reduces the computational cost since only the parcel is tracked. The number of particles per parcel needs to be judiciously chosen to ensure accuracy.[44] If there is no inter-phase mass transfer (inert particles), the solid-phase governing equations are given as

$$\frac{dx_{p,i}}{dt} = u_{p,i}, \tag{8}$$

$$m\frac{du_{p,i}}{dt} = \frac{\pi}{2} r_p^2 C_D \rho |\bar{u}_i - u_{p,i}|(\bar{u}_i - u_{p,i}), \tag{9}$$

$$mC_p\frac{dT_p}{dt} = 2\pi r_p \kappa_g \mathrm{Nu}(T - T_p), \tag{10}$$

where $\bar{u}_i$ is the local velocity of the gas, Nu is the gas-phase Nusselt number, r_p is the particle radius, and m is the particle mass, which is obtained as $(4/3)\pi r_p^3 \rho_p$ where ρ_p is the particle density. For this study, the model assumes that the pressure gradient term, the Basset term, the Saffman lift, the Magnus lift, and the inter-particle interaction term are all second-order effects.[37,43] They are neglected in this study. The drag coefficient, C_D, is based on the following empirical relationship validated for shock-particle interactions:[45]

$$C_D = \left[0.38 + \frac{24}{\mathrm{Re}_p} + \frac{4}{\mathrm{Re}_p^{0.5}}\right]\left[1 + \exp\left(-\frac{0.43}{\mathrm{M}_p^{4.467}}\right)\right]. \tag{11}$$

In this expression, the drag is a function of the particle Reynolds number, $\mathrm{Re}_p = 2r_p|u_{p,i} - u_i|\rho/\mu$, and the particle Mach number, $\mathrm{M}_p = |u_{p,i} - \bar{u}_i|/a_s$, where a_s is the speed of sound in the gas. Following previous studies,[43] convection is assumed to be the dominant heat transfer mechanism between the two phases. The Nusselt number, Nu, used in Eq. (10), is computed as a function of Re_p and the Prandtl number, Pr, from the following relationship:[46] $\mathrm{Nu} = 2.0 + 0.459\mathrm{Pr}^{0.33}\mathrm{Re}_p^{0.55}$.

The governing equations for the solid-phase are integrated in time using a fourth-order Runge-Kutta scheme, and the inter-phase coupling terms in Eqs. (2) and (3) are the volumetrically averaged

This article is copyrighted as indicated in the article. Reuse of AIP content is subject to the terms at: http://scitation.aip.org/termsconditions. Downloaded to IP: 143.215.48.65 On: Tue, 31 Dec 2013 19:32:03

quantities given as

$$\dot{F}_{p,i} = \frac{1}{\mathcal{V}}\sum_{n=1}^{N_p}\left[\frac{\pi}{2} r_{p,n}^2 C_{D,n}\rho_n |u_{p,i,n} - u_{i,n}|(u_{p,i,n} - u_{i,n})\right], \tag{12}$$

$$\dot{Q}_p = \frac{1}{\mathcal{V}}\sum_{n=1}^{N_p}[2\pi r_{p,n}\kappa_g \mathrm{Nu}_n(T_n - T_{p,n})], \tag{13}$$

$$\dot{W}_p = \frac{1}{\mathcal{V}}\sum_{n=1}^{N_p}\left[\frac{\pi}{2} r_{p,n}^2 C_{D,n}\rho_n |u_{p,i,n} - \bar{u}_{i,n}|(u_{p,i,n} - \bar{u}_{i,n})u_{p,i,n}\right], \tag{14}$$

where $\mathcal{V}$ is the volume of the computational cell, and the subscript n indicates a quantity of the nth parcel in the summation over the total number of particles in $\mathcal{V}$. More information regarding the implementation, validation, and application of the current multi-phase solver can be found in previous work.[35,37,43]

III. SIMULATION METHODOLOGY

A. Single-phase simulations

Since many past numerical simulations[28–30] show a reasonably good comparison to data measured in the air/SF$_6$ (single-phase) re-shock RMI experiments of Vetter and Sturtevant,[25] a similar configuration is adopted here to act as a reference point for the two-phase studies. Yet, it is important to note that recent experiments[23] have used particle image velocimetry (PIV) and planar laser-induced fluorescence (PLIF) techniques to obtain more detailed measurements of the RMI before and after re-shock. Particularly, these experiments have avoided introducing errors through the use of a cellulose membrane to initially separate the light and heavy gas mixtures. For computational studies, however, the correct initialization of such experimental configurations, while not impossible,[32] is more difficult to obtain. Thus, in the current work, previous computational studies of the Vetter and Sturtevant[25] are leveraged as a basis for the two-phase studies.

The Vetter and Sturtevant[25] experiments were conducted in a shock-tube with cross-sectional dimensions of $L_y \times L_z$, and a variable longitudinal length of L_x. The air/SF$_6$ mixture is initially separated by a thin membrane supported by a wire mesh of 1 cm spacing. As the initial shock speed is varied from Mach 1.18 to 1.98, the length of the test section is adjusted from 61 cm to 122 cm to ensure that the re-shocked mixing zone is within the observational test-section. High resolution spark-Schlieren images and high-speed cameras were used to obtain data about the mixing zone flow features and growth-rates. For the validation study, two experimental configurations are simulated, denoted as VS0-VI and VS0-VII, which correspond to case VI^b and case VII^b of Vetter and Sturtevant.[25] Only the gas-phase initialization of case VS0-VI is used for the multi-phase studies presented later. The reference conditions for these cases are summarized in Table I, and a schematic of the simulation domain is given in Fig. 1.

TABLE I. Test conditions and measurements of the re-shocked RMI experiments of Vetter and Sturtevant[25] where VS0-VI and VS0-VII correspond to experiments VI^b and VII^b.

	VS0-VI	VS0-VII
Incident Mach number	1.5	1.98
Pressure (kPa)	23.0	8.0
Distance from interface to wall, L$_x$ (m)	0.62	0.49
Instantaneous velocity, ΔV (m/s)	150.0	287.0
Shocked growth-rate (m/s)	4.2	7.5
Re-shocked observation time (m/s)	37.2	74.4
Shocked observation time (ms)	2.2–3.2	1.7–2.5
Re-shocked observation time (ms)	4.0–5.5	1.7–2.5

This article is copyrighted as indicated in the article. Reuse of AIP content is subject to the terms at: http://scitation.aip.org/termsconditions. Downloaded to IP: 143.215.48.65 On: Tue, 31 Dec 2013 19:32:03

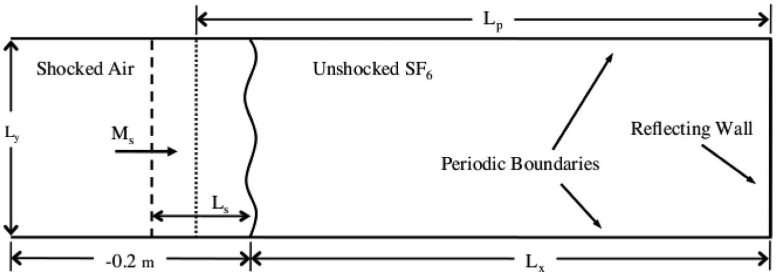

FIG. 1. Schematic of the simulation domain where M_s is the Mach number of the shock, L_x is the distance from the end wall to the contact, and L_s is the distance from the contact to the initial shock position. For the multi-phase simulations, L_p is the length of the initial particle cloud.

The experiments were designed to avoid boundary layer interaction with the mixing layer. Thus, the side-walls of the shock tube (in y- and z-directions) can safely be treated numerically as periodic boundaries, an assumption also made in prior numerical studies.[28–30] The end wall ($x = L_x$) is modeled as a no-slip boundary, and the inflow boundary at $x = -0.2$ m is initially modeled as a supersonic inflow boundary, but to allow the exit of the reflected and transmitted waves later in the simulation, the boundary is changed to a non-reflecting characteristic outflow boundary later in the simulation. This prohibits the non-physical reflection of waves from the boundary, which could corrupt the mixing-layer growth at late times.

The development of the RMI is highly sensitive to the initial structure of the interface separating the light (air) and heavy (SF_6) species.[30] In the current study, the interface is formed by specifying the SF_6 mass fraction, Y_{SF_6}, with an initial hyperbolic tangent profile[22] centered at $x = 0.0$ m and a characteristic thickness of δ given by

$$Y_{SF_6}(x, y, z; 0) = \frac{1}{2} - \frac{1}{2}\tanh\left(\frac{x - \eta_I(y, z)}{\delta}\right), \tag{15}$$

where $\eta_I(y, z)$ is the interface perturbation. Following previous numerical simulations,[28–30] an "egg-carton" sinusoidal perturbation for $\eta_I(y, z)$ is used to model the wire-meshed membrane separating the air and SF_6 gases in the experiments and is described by the expression

$$\eta_I(y, z) = a_0|\sin(k_0 y)\sin(k_0 z)| + a_1\cos(k_1 y)\cos(k_1 z) + a_2\Psi(y, z), \tag{16}$$

where the first term represents the small-scale perturbations resulting from the wire-mesh, and the second term represents the scales associated with the transverse dimensions of the shock tube. The last term includes random perturbations, which are used to account for small-scale irregularities and to break the symmetry of the initial conditions and accelerate the transition of the RMI to nonlinear growth. The values of the coefficients used in the current study are $a_0 = a_1 = 1.25 \times 10^{-3}$ m and $a_2 = 2.5 \times 10^{-4}$ m with the random initial small-scale perturbations, $\Psi(y, z)$, prescribed by an adapted von Karman power spectrum,[30]

$$E_\Psi(k) = k^{-2}\left[\frac{kL}{\sqrt{(kL)^2 + B}}\right]^4, \tag{17}$$

where $L = 0.95$ cm, $B = 5\sqrt{2}$, and $k = \sqrt{k_y^2 + k_z^2}$, where $k_y = 2\pi/L_y$ and $k_z = 2\pi/L_z$. The random fluctuations, $\Psi(y, z)$, were normalized such that they have a root-mean-square amplitude of one with the amplitude is set by a_2. These values as well as the simulation configuration parameters are summarized in Table II.

Figure 2(a) shows the time evolution of the mixing length, $\eta(t)$, compared to the experimental growth-rate data for the two re-shock configurations defined in Table I. In practice, there are many ways to define the width of the mixing zone. In this study, an integral definition is adopted where

This article is copyrighted as indicated in the article. Reuse of AIP content is subject to the terms at: http://scitation.aip.org/termsconditions. Downloaded to IP: 143.215.48.65 On: Tue, 31 Dec 2013 19:32:03

TABLE II. Summary of the simulation configurations used in the re-shock validation experiment (VS) and the multi-mode (MM) and single-mode (SM) numerical simulations. The function $\mathcal{U}_r$ represents a uniform random variable chosen on the interval [0,1], $k_0 = 2\pi/L_y$, and Δx is the grid resolution used for each case. All dimensional values are given in units of centimeters.

Case name	$\eta_I(y, z)$	$\Psi(y, z)$	a_0	a_1	a_2	$k_0\eta_0$	L_y, L_z	L_p	L_s	Δx
VS	Eq. (16)	Eq. (17)	0.25	0.125	0.125	0.00926	27.0	...	5.0	0.105
MM	Eq. (16)	Eq. (17)	0.25	0.125	0.125	0.0185	13.5	65.0	5.0	0.105
SM	Eq. (19)	...	0.25	0.0	0.0	0.0185	13.5	65.0	5.0	0.105
SMR	Eq. (19)	$\mathcal{U}_r$	0.25	0.0	0.2	0.0185	13.5	65.0	5.0	0.105
SMN	Eq. (19)	...	2.5	0.0	0.0	0.185	13.5	65.0	5.0	0.105

the mixing length is given by

$$\eta(t) = 4\int_{-0.2}^{L_x} \langle Y_{\mathrm{SF}_6}\rangle \left(1.0 - \langle Y_{\mathrm{SF}_6}\rangle\right) \mathrm{d}x. \tag{18}$$

The quantity $\langle \cdot \rangle$ represents a volumetric average in the transverse directions over the distances L_y and L_z, and is a function of only the time, t, and x, the longitudinal direction.

For a single-mode initial perturbation, the mixing length growth is approximately linear following the theoretical estimation given by Richtmyer's impulsive model,[3] $\dot{\eta} = v_0 = k_0\eta_0 A^+ \Delta V$. In this equation, η_0 is the initial amplitude [$= a_0$], A^+ is the post-shock Atwood number [$= (\rho_{\mathrm{SF}_6} - \rho_{\mathrm{Air}})/(\rho_{\mathrm{SF}_6} + \rho_{\mathrm{Air}})$], and ΔV is the velocity jump at the contact discontinuity. The initial perturbation is given by

$$\eta_I(y, z) = \frac{a_0}{2}\Big(\sin(k_0 y) + \sin(k_0 z)\Big) + a_2\Psi(y, z), \tag{19}$$

with the values of a_0 and a_2 given in Table II and the configuration summarized in Table III. The evolution of the normalized mixing length for the single-mode RMI is shown in Fig. 2(b). Even under these conditions, however, the RMI transitions to nonlinearity and is more appropriately described by the model of Sadot *et al.*[8] also shown in Fig. 2(b).

For case VS0-VI at $t = 3.46$ ms, re-shock occurs. This results in a compression of the mixing zone, noticeable by the reduction in the mixing length, followed by a subsequent increase in the

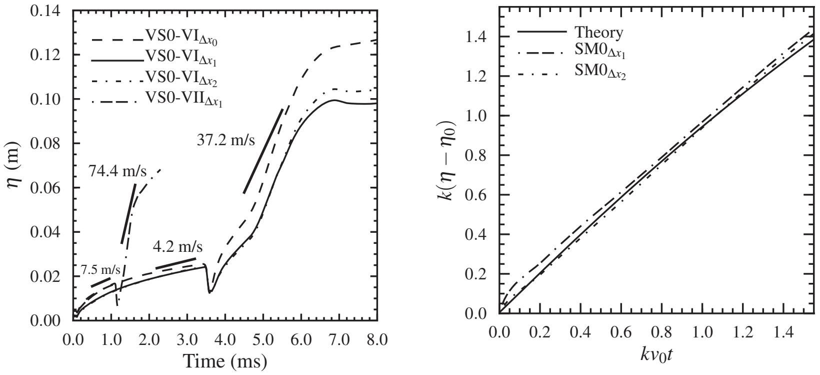

(a) (b)

FIG. 2. (a) Evolution of the mixing layer $\eta(t)$ at three different grid resolutions ($\Delta x_0 = 0.21$ cm, $\Delta x_1 = 0.105$ cm, $\Delta x_2 = 0.07$ cm) with comparison to the experimental measurements summarized in Table I. (b) Time history of the normalized mixing length in single-mode RMI at the same grid resolutions (Δx_1, Δx_2) with a comparison to the nonlinear theory of Sadot *et al.*[8]

This article is copyrighted as indicated in the article. Reuse of AIP content is subject to the terms at: http://scitation.aip.org/termsconditions. Downloaded to IP: 143.215.48.65 On: Tue, 31 Dec 2013 19:32:03

TABLE III. Summary of the multi-phase initial conditions used in the numerical simulations. Simulations are referred to by the case name (i.e., SM, MM, etc.) defined in Table II and the case number defined below. For reference, this table additionally provides the RMI growth-rate data for the SM cases.

					SM			
Case no.	α_0	r_p (μm)	N_0	$\mathcal{P}$	St	ΔV (m/s)	A$^+$	A$_m^+$
0	0.0	...	...	...	...	147.9	0.781	...
1	2.0×10^{-5}	30	2 094 876	3	1.11	146.4	0.725	0.689
2	2.0×10^{-5}	60	261 859	1	3.21	146.5	0.725	0.689
3	2.0×10^{-5}	120	32 732	1	9.98	146.3	0.725	0.689
4	4.0×10^{-5}	5	904 986 837	1300	0.09	135.7	0.709	0.641
5	4.0×10^{-5}	10	113 123 354	170	0.23	137.6	0.717	0.649
6	4.0×10^{-5}	30	4 189 753	6	1.11	142.7	0.724	0.656
7	4.0×10^{-5}	60	523 719	1	3.22	145.5	0.725	0.657
8	4.0×10^{-5}	120	65 464	1	9.98	146.2	0.725	0.657
9	1.0×10^{-4}	30	10 474 384	15	1.11	142.2	0.719	0.572
10	1.0×10^{-4}	60	1 309 298	2	3.21	142.7	0.724	0.576
11	1.0×10^{-4}	120	163 662	1	9.98	143.7	0.724	0.576
12	2.0×10^{-4}	30	20 948 769	30	1.11	141.6	0.716	0.470
13	2.0×10^{-4}	60	2 618 596	4	3.21	142.5	0.720	0.475
14	2.0×10^{-4}	120	327 324	1	9.98	142.9	0.724	0.478

mixing length as the reflected shock further amplifies the perturbations in developing mixing zone. This tends to hasten the production of small-scale structures prompting the development of an inertial sub-range.[20,23]

The results in Fig. 2 are given for three different grid resolutions: $\Delta x_0 = 0.21$ cm, $\Delta x_1 = 0.105$ cm, and $\Delta x_2 = 0.07$ cm. For the two highest resolutions, the RMI growth-rates are indistinguishable with only small differences in the final saturated mixing length and thus serving as a reasonable demonstration of grid convergence. A grid resolution of $\Delta x = \Delta x_1 = 0.105$ cm, which was used in previous studies,[29] is chosen for the rest of the studies resulting in a computational grid of 780 × 256 × 256. The numerical results show good agreement to the experimental measurements of the RMI growth-rates before and after re-shock, and in the case of the single-mode simulations, to the analytical models of the RMI growth-rate prior to re-shock. These results lend confidence to the numerical methodology, simulation configuration, and initialization used in this study. As a final note, it is emphasized that the comparison between the experimental data and the computational predictions are of the RMI growth-rates only. In the experiments, the initial perturbation amplitudes develop at a much smaller scale. After re-shock, the mixing lengths are more comparable. The experimental mixing length at 6.25 ms is 10.2 cm (as taken from Hill *et al.*[29]), whereas the numerical prediction is approximately 9.7 cm at that time.

B. Multi-phase simulations

For the two-phase simulations, a uniform region of spherical particles with a radius of r_p spanning the cross-sectional area of $L_y \times L_z$ and the length L_p is superimposed onto the single-mode and multi-mode configurations discussed in Sec. III A and shown schematically in Fig. 1. From theoretical analysis,[37,38] two parameters are used to characterize the dynamics of the RMI in a dilute gas-particle mixture: the mass loading (f) and the Stokes number (St). The mass loading is defined as the ratio of the particle mass per unit volume to the gas density ($f = mn_0/\rho$, where n_0 is the number of particles per unit volume, m is the particle mass, and ρ is the fluid density). From this, a multi-phase Atwood number can be defined as[37]

$$A_m = \frac{\rho_2\,(1 + f_2) - \rho_1\,(1 + f_1)}{\rho_2\,(1 + f_2) + \rho_1\,(1 + f_1)}, \tag{20}$$

This article is copyrighted as indicated in the article. Reuse of AIP content is subject to the terms at: http://scitation.aip.org/termsconditions. Downloaded to IP: 143.215.48.65 On: Tue, 31 Dec 2013 19:32:03

where the subscripts 1 and 2 refer, respectively, to the light (air) and the heavy (SF_6) gases separated by the contact discontinuity. If no particles are present ($f_1 = f_2 = 0$), as in case SM0, then A_m reduces to A. Also, note that for $A > 0$ and uniform particle loading across the contact discontinuity, A_m is always less than A. By linearizing the dilute gas-particle equations, it is possible to derive a multi-phase impulsive theory,[37] which results in the following linear equation for the mixing length as a function of time:

$$\eta(t) = \eta_0(1.0 + k_0 A_m \Delta V t) = \eta_0 + v_{0,m} t. \tag{21}$$

The result is that A_m simply replaces A where the use of A_m accounts for the reduction in the effective impulse strength resulting from the particle mass loading of the flow. This theory, however, is derived in the limit of vanishing Stokes number, and thus is only applicable for St $\ll$ 1.0 flows. The Stokes number is computed as $\tau_p/\tau_{RMI} = kA\Delta V \tau_p$, where the time-scale of the particles is $\tau_p = (1/4)\pi r_p \rho_p C_D \mu$. For the SM cases, τ_{RMI} is approximately 2.4 ms. In this study, the particles are chosen to have the properties of steel, such that $\rho_p = 7800$ kg/m^3. Therefore, given the same gas-phase conditions, St is a strong function of the particle radius.

Using these multi-phase parameters, A_m and St, a parameter study is conducted to study the RMI in a dilute gas-particle mixture. The gas-phase reference conditions ($M_s = 1.5$, $p_0 = 23$ kPa, $T_0 = 298.15$ K) of case VS0-VI from Table I are kept constant (for reasons explained in Sec. III A), while the size (r_p) and the number of particles (N_0) within the domain are varied independently. The multi-phase conditions discussed in this study are summarized in Table III. The values of r_p and N_0 considered in this study are limited by the dilute assumption, i.e., dispersed-phase volume fractions, α, less than 1%. While the simulations presented here are only a portion of the possible conditions, additional simulations indicate that the conclusions drawn from the data reported here apply over a much larger range within the limits of the numerical formulation. Furthermore, as will be discussed in more detail later, the particle cloud compresses throughout the simulation which limits the initial value of α_0. Henceforth, these numerical experiments are referred to by the case name (i.e., SM, MM, etc.) defined in Table II and the case number (i.e., 0, 1, 2, etc.) defined in Table III. The former defines the initial configuration and perturbation interface, while the latter defines multi-phase parameters. For example, case MM0 refers to a multi-mode, single-phase simulation.

Also given in Table III is the number of particles per parcel, $\mathcal{P}$, used in each case as well as the initial volume fraction α_0, which is defined as the ratio of the total volume occupied by the particles, $V_p = N_0(4/3)\pi r_p^3$, to the volume $V = L_y L_z L_p$, where L_p is the distance from the end-wall in the x-direction occupied by the particles (see Fig. 1). In this study, $L_p = 65.0$ cm is kept constant.

IV. RESULTS AND DISCUSSION

There are noticeable differences in the time evolution of the RMI in multi-phase flows. Figure 3 shows the time history of the mixing length, $\eta(t)$, and mixing fraction, $\Theta(t)$, of two representative multi-phase cases, MM12 and MM14, compared to results from the single-phase simulation MM0. The molecular mixing fraction, Θ, is defined as

$$\Theta(t) = \frac{\int \langle Y_{SF_6} Y_{air} \rangle \mathrm{d}x}{\int \langle Y_{SF_6} \rangle \langle Y_{air} \rangle \mathrm{d}x}. \tag{22}$$

It is a more useful description of how well-mixed the two species are in the mixing zone since the span-wise averaged mass fraction carries no distinction between regions that are completely mixed and those regions that are unmixed, but contain equal portions of species. Thus, Θ quantifies the relative amount of molecularly mixed fluid within the mixing layer, such that $\Theta = 1.0$ would mean that the entrained fluids were completely mixed within each transverse plane.

For $\alpha_0 > 1.0 \times 10^{-4}$, there is a noticeable increase in the growth-rate of the multi-phase RMI before re-shock as well as a corresponding decrease in the molecular mixing fraction meaning that the rate of entrainment is increased. A comparison of the mass fraction contours colored by the x-velocity at $t = 3.0$ ms in Fig. 4 shows that the presence of particles in flow effectively increases the size and distortion of the mixing interface, while decreasing its convective velocity. The location

This article is copyrighted as indicated in the article. Reuse of AIP content is subject to the terms at: http://scitation.aip.org/termsconditions. Downloaded to IP: 143.215.48.65 On: Tue, 31 Dec 2013 19:32:03

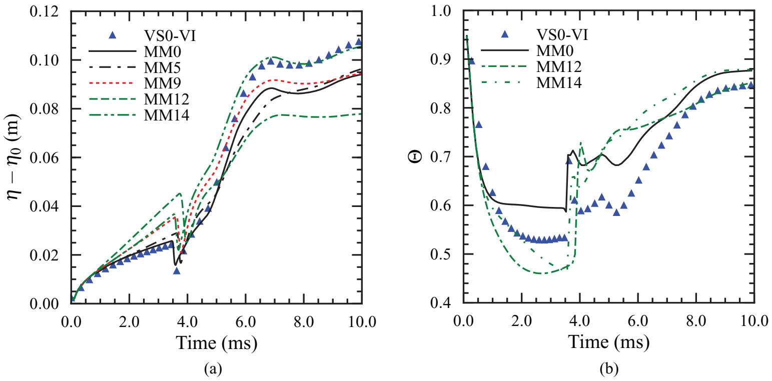

(a) (b)

FIG. 3. Time evolution of (a) the mixing layer width, $\eta(t)$, and (b) the mixing fraction, $\Theta(t)$, for the multi-mode RMI in a dilute gas-particle mixture compared to the single-phase results of VS0-VI and MM0.

of the mixing zone can be identified by using a threshold value of the species mass fraction. Thus, the left (spike) and right (bubble) interfaces are defined by $x_{\eta,L} = x|_{Y_{\mathrm{SF}_6}=0.01}$ and $x_{\eta,R} = x|_{Y_{\mathrm{SF}_6}=0.99}$. Further, the particle cloud is defined between x_p, the position of the leftmost particle, and the end-wall at 0.62 m.

The *x*-*t* diagram, shown in Fig. 5(a), shows the location of the shock in relation to the mixing zone and the particle cloud. For small St, the particle cloud is significantly compressed and interacts with the mixing zone after re-shock. The compression of the particle cloud is further indicated by the ratio of the volume fraction to the initial volume fraction, α/α_0. Thus for low St, the mass loading increases throughout the simulation. Note that the volume fraction still remains within dilute limit. This results in a reduction in the mixing zone length at late-times; however, the molecular mixing fraction for all cases asymptote to values between 0.84 and 0.88.

A. Initial growth-rate

RMI develops as a result of vorticity deposited along the interface by the production of baroclinic torque. This process can be investigated using the compressible vorticity transport equation, given by Eq. (23), which is derived by taking the curl of the momentum conservation equation. The tensor form of this equation is given as

$$\begin{aligned}\frac{D\omega_i}{Dt} &= \omega_j \frac{\partial u_i}{\partial x_j} - \omega_i \frac{\partial u_j}{\partial x_j} + \epsilon_{ijk} \frac{\partial}{\partial x_j}\left(\frac{1}{\rho}\frac{\partial \tau_{km}}{\partial x_m}\right) + \frac{1}{\rho^2}\epsilon_{ijk}\frac{\partial \rho}{\partial x_j}\frac{\partial p}{\partial x_k} + \epsilon_{ijk}\frac{\partial}{\partial x_j}\left(\frac{\dot{F}_{p,k}}{\rho}\right) \\ &= \Omega_i^s + \Omega_i^d + \Gamma_i + \beta_i + \Pi_i. \end{aligned} \quad (23)$$

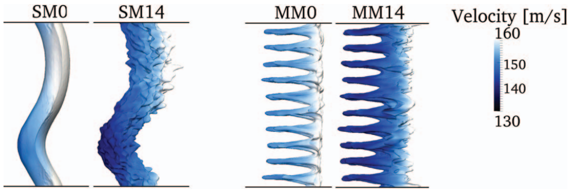

FIG. 4. Contours of the species mass fraction, $Y_{\mathrm{SF}_6} = Y_{\mathrm{Air}} = 0.5$ for the single-phase cases SM0 and MM0 compared to representative multi-phase cases SM14 and MM14 colored by the velocity in the *x*-direction.

This article is copyrighted as indicated in the article. Reuse of AIP content is subject to the terms at: http://scitation.aip.org/termsconditions. Downloaded to IP: 143.215.48.65 On: Tue, 31 Dec 2013 19:32:03

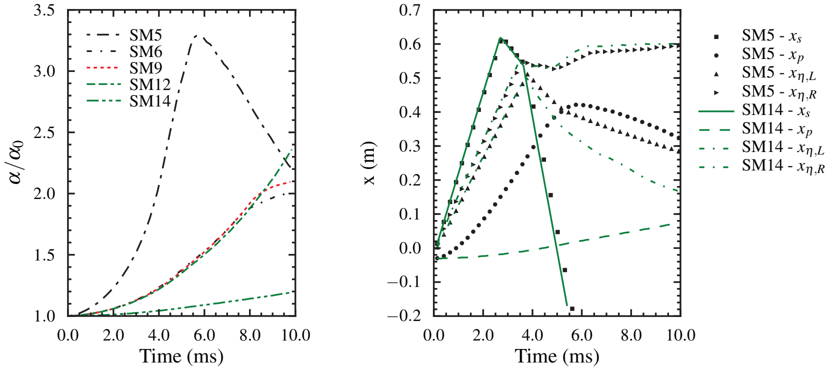

(a) (b)

FIG. 5. (a) Time evolution of the ratio of the particle cloud volume fraction, α, to the initial volume fraction, α_0. (b) *x-t* diagram of the time history of the shock location, x_s, the left interface of the particle cloud, x_p, and the left (spike) and right (bubble) interfaces of the mixing zone, $x_{\eta,\,L}$ and $x_{\eta,\,R}$, respectively.

The first two terms in this equation, Ω_i^s and Ω_i^d, represent the transport of vorticity through vortex stretching and dilatation. The third term, Γ_i, represents the production of vorticity by viscous stresses, while the fourth term, β_i, represents the production/destruction of vorticity by baroclinic torque. In addition to these terms, an additional vorticity production occurs in multi-phase flows resulting from the inter-phase momentum coupling term, $\dot{F}_{p,k}$, which is represented by the term, Π_i. The viscous contribution to vorticity dissipation is ignored here.

For St $<$ 1, cases SM4 and SM5, Fig. 6(a) shows that the width of the mixing-layer is reduced by approximately 11%. This reduction is predicted by the linear impulsive model of Ukai *et al.*,[37] given by Eq. (21), where $\dot{\eta}_{\rm num}/\dot{\eta}_{\rm model} = 0.96$. For the cases where St $>$ 1, however, the mixing-layer growth rate increases with the increase proportional to the mass loading (larger r_p and larger α_0). For cases SM12 and SM14, there is a 7.3% and 10.8% increase, respectively, while for cases SM9 and SM11, there is only a 3.0% and 5.7% increase, respectively. To ensure that this observation is a direct result of the gas-particle interaction, a case without particles, but with a random multi-mode initialization, case SMR0 (not shown), is also simulated and shows no observable change in the mixing layer from case SM0. Therefore, the increase in the multi-phase RMI mixing length is a result of the continued presence of the particles within the flow. A possible explanation for this is the presence of an additional vorticity production term in Eq. (23), which is non-zero as a result of the differential gas-particle velocities. Figure 6(b) shows the time evolution of the magnitude of the vorticity production contributions from the baroclinic torque, $|\beta_i(t)|$, and the interphase particle term, $|\Pi_i(t)|$, volume averaged over the mixing layer, defined as extending between $x_{\eta,\,L}$ and $x_{\eta,\,R}$ in the longitudinal direction and L_y and L_z in the transverse directions. For simulations where the particle vorticity production is much less than the vorticity production by baroclinic torque ($|\beta_i(t)| \gg |\Pi_i(t)|$), there is a correspondingly little or no increase in the mixing-layer growth rate. However, when the two terms are of similar magnitude, the mixing-layer growth-rate increases as a result of this additional vorticity production. For example, the magnitude of the span-wise volume averaged vorticity, $|\omega_i(t)|$, at $t = 2.5$ ms for case SM14 is 38.7 s^{-2} compared to 20.6 s^{-2} for case SM0.

By increasing $k_0\eta_0$, the initial misalignment of the pressure and the density at the interface increases the baroclinic torque production and therefore, the relative difference between $|\Pi_i(t)|$ and $|\beta_i(t)|$, is altered. Though not shown here, this trend is observed by comparing the deviations of cases SMN12-14 and SM12-14 from the single-phase cases SMN0 and SM0, respectively. The mixing zone width at $t = 3.0$ ms for case SMN12 is slightly reduced by 1.78% compared to case SMN0 ($\eta_{\rm SMN12} = 0.143$, $\eta_{\rm SMN0} = 0.145$), and for case SMN14, a small increase of 2.2% is observed. These

This article is copyrighted as indicated in the article. Reuse of AIP content is subject to the terms at: http://scitation.aip.org/termsconditions. Downloaded to IP: 143.215.48.65 On: Tue, 31 Dec 2013 19:32:03

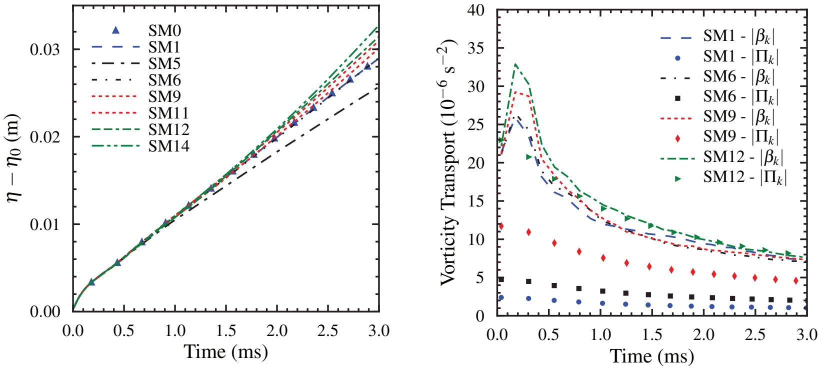

(a)

(b)

FIG. 6. (a) Evolution of the mixing layer width, $\eta(t)$, at different α_0 and St. (b) The vorticity transport budget during the initial growth of the RMI for cases with the same r_p where $|\Pi_k(t)|$ and $|\beta_k(t)|$ are the magnitude of the vorticity production due to the particle acceleration term and the baroclinic torque volume-averaged over the mixing zone.

deviations from the single-phase results are much less than those observed for SM12 and SM14 shown in Fig. 6(a), with case SMN12 actually showing reduction in η instead of an increase.

Also, it is interesting to note that from comparison of cases MM12-14 and SM12-14 between Figs. 3(a) and 6(a), the increase in the width of the mixing layer is much larger for the multi-mode initializations than the single-mode initializations. Physically, this results from an increase in the inter-phase coupling within the mixing layer for the multi-mode initializations, and is ultimately observed in the vorticity transport budget. It should be further noted that in the multi-mode RMI, the width of the mixing layer is larger for case MM12 than case MM14. This is a reversal in the trend observed in single-mode RMI, which can be explained by the differences in time-history of vorticity magnitude. For case MM12, at $t = 2.5$ ms, $|\omega_i|$ is 35.5 s^{-2} compared to a value of 25.5 s^{-2} for case MM14, where for the single-mode cases SM12 and SM14 at $t = 2.5$ ms, $|\omega_i|$ is 38.9 s^{-2} and 42.1 s^{-2}, respectively.

In summary, for St $\ll 1$, the assumption of gas-particle equilibrium is more accurate, and the two-phase linear impulse model[2] and multi-phase buoyancy-drag model[38] match the trends observed in the current three-dimensional numerical simulations. For St > 1, however, the assumptions made in these models are less accurate since the nonlinear two-phase coupling terms are significant.

B. Re-shock

After the initial shock refraction, the transmitted wave continues to propagate through the two-phase medium. The presence of the particles reduces the speed of the shock wave, thus the time for the wave to reach the end wall and reflect is increased. For instance, the shock wave takes 2.64 ms to travel the length of the domain in case SM0, while it takes 2.81 ms in case SM5. In general, the dynamics of the shock, particle cloud and mixing zone is summarized in *x*-*t* diagram in Fig. 5(a). At re-shock the reflected wave compresses the flow further and refracts through the developing mixing-zone. As a result of the particle drag, the time at which re-shock is delayed as observed in Fig. 7(a). This analysis, however, is complicated by the time-dependence of the mass loading. For a given initial volume fraction, simulations with a smaller St (smaller r_p) show that the effective volume fraction increases in the domain (see Fig. 5(b)) as the particle cloud compresses due to the presence of the end-wall. Thus, the total drag is more significant for flows of the same α_0 but smaller St. For example, the mixing layer width just begins to compress at $t_r = 3.73$ ms for case SM12 and at $t_r = 3.51$ ms for case SM14, a 6% change, while between cases SM5 and SM8 there is only a 4.5% change ($t_r = 3.61$ ms and $t_r = 3.45$ ms, respectively).

This article is copyrighted as indicated in the article. Reuse of AIP content is subject to the terms at: http://scitation.aip.org/termsconditions. Downloaded to IP: 143.215.48.65 On: Tue, 31 Dec 2013 19:32:03

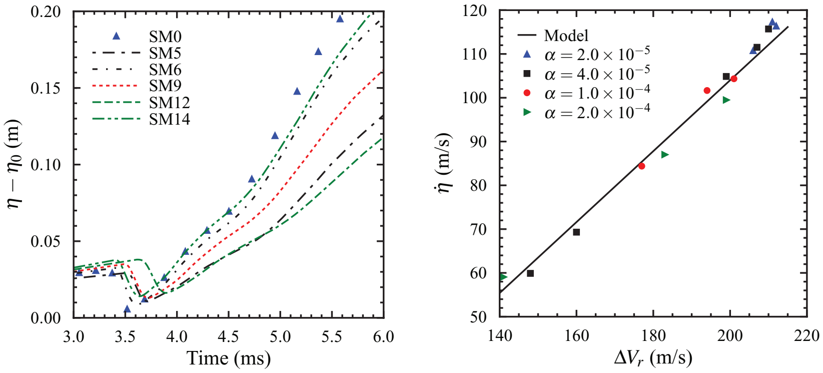

(a) (b)

FIG. 7. (a) Time evolution of the mixing-layer growth, $\eta(t)$, after re-shock. (b) Relationship between the velocity jump, ΔV_r, at re-shock and the re-shocked RMI growth-rate, $\dot{\eta}$, compared to the model given by Eq. (25).

The correlation between the velocity jump across the contact at re-shock and the re-shocked RMI growth-rate is shown in Fig. 7(b) with the data summarized in Table IV. As observed in Fig. 7(b), there is a clear linear relationship between ΔV_r and $\dot{\eta}_r$. This follows the trends observed in the single-phase re-shock experiments[25] and corresponds to the analytical model derived by Mikaelian[26] given by the correlation

$$\dot{\eta}_r = C A_r^+ \Delta V_r, \tag{24}$$

where C is an empirical constant determined by Mikaelian[26] to be 0.28, ΔV_r is the jump in velocity across the contact at re-shock, and A_r^+ is the post re-shock Atwood number. Thornber *et al.*[33] have modified this relationship to account for differences in the initial conditions which are manifested through the changes in the molecular mixing fraction at the time of re-shock. The time evolution of $\Theta(t)$ shown in Fig. 9 indicates that the molecular mixing fraction prior to re-shock is a function of the initial St, where the molecular mixing fraction at re-shock, Θ_r, is larger for smaller St. Given this dependence, a semi-analytical model for the re-shocked RMI growth rate can be adapted for dilute

TABLE IV. Summary of the re-shocked RMI growth-rate data with the numerically computed value of the linear coefficient, $C_{r,\,\mathrm{num}}$.

Case	A_r^+	$A_{m,r}^+$	Θ_r	ΔV_r (m/s)	$\dot{\eta}_r$ (m/s)	$C_{r,\,num}$
SM1	0.779	0.739	0.304	206.0	110.8	0.872
SM2	0.771	0.741	0.288	211.0	117.3	0.889
SM3	0.771	0.741	0.297	212.0	116.4	0.883
SM4	0.739	0.610	0.439	148.0	59.9	0.886
SM5	0.743	0.640	0.408	160.0	69.3	0.880
SM6	0.768	0.704	0.283	199.0	104.9	0.884
SM7	0.769	0.711	0.286	207.0	111.5	0.896
SM8	0.770	0.712	0.292	210.0	115.7	0.920
SM9	0.755	0.614	0.350	177.0	84.4	0.963
SM10	0.761	0.631	0.293	194.0	101.7	0.987
SM11	0.770	0.643	0.280	201.0	104.3	0.952
SM12	0.754	0.556	0.416	141.0	59.1	0.986
SM13	0.756	0.581	0.322	183.0	87.0	0.994
SM14	0.766	0.599	0.294	199.0	99.5	0.993

This article is copyrighted as indicated in the article. Reuse of AIP content is subject to the terms at: http://scitation.aip.org/termsconditions. Downloaded to IP: 143.215.48.65 On: Tue, 31 Dec 2013 19:32:03

gas-particle mixtures and is given by

$$\dot{\eta}_r = C_r\sqrt{1-\Theta_r}A^{+}_{m,r}\Delta V_r, \tag{25}$$

where similar to the multi-phase impulsive model, Eq. (21), the post re-shock multi-phase Atwood number, $A^{+}_{m,r}$, replaces A^{+}_{r}. The value of C_r is determined to be approximately 0.895. Table IV gives the numerically calculated values of the constant C_r. This model is then used to predict the re-shocked RMI growth rate of the multi-mode cases MM12-14. The agreement is within 10% of the numerically predicted values further indicating that both $A^{+}_{m,r}$ and Θ_r are able to capture the dependence of the re-shocked growth-rate on the initial mass loading and the particle radius. The constant, however, seems to be weakly dependent on the initial volume fraction.

C. Late-time mixing

After re-shock, the growth of the mixing zone further accelerates, and as the bubble structures merge and the anisotropy decreases, the dominate wave number shifts to lower wavelengths while increasingly smaller scales are created through vortex stretching. Previous experimental measurements and computational predictions[29] show that at late times the re-shocked mixing zone closely approximates decaying isotropic inertial range turbulence. In the multi-mode simulations conducted here, a similar trend is observed; the fluctuating energy spectrum at $t = 8.0$ ms is shown in Fig. 8 for cases MM0, MM12, and MM14. For the same volume fraction, higher mass loadings result in more energetic large-scale fluctuations. The total turbulent kinetic energy, TKE $= \int E(k)dk$ is approximately 51 m/s for MM14 and only 18.25 m/s at $t = 8$ ms, where $E(k)$ is the fluctuating specific kinetic energy. At $t = 10$ ms, the TKE decays to 21 m/s and 7.5 m/s, respectively. Likewise the turbulent energy dissipation rate, $\epsilon = \int 2\nu k^2 E(k)dk$, is much larger for case MM14 than MM12. These conditions are borne out of the differences in the asymptotic widths of the mixing zone ($\eta_{\mathrm{MM0}} \approx 9.5$ cm, $\eta_{\mathrm{MM12}} = 7.9$ cm and $\eta_{\mathrm{MM14}} = 10.5$ cm), which were a result of the variance in the re-shock time and growth-rate. The late-time mixing fraction (see Fig. 3(b)), however, is roughly equivalent for all cases simulated in this study, and varies only between 0.84 and 0.88, a further indication that mixing zone has reached a state of decaying self-similar turbulence.

For the single-mode initializations, the width of the mixing zone does not saturate, which is evident by Fig. 9(a), during the time period simulated in this study. As a result, the scales of the flow at the same time ($t = 8$ ms) are much larger and more anisotropic as compared to the multi-mode cases. This results in a wide-range of molecular mixing fractions as observed in Fig. 9(b) compared to those in Fig. 3(b). Initially, Θ is close to one since the mixing layer is only a small diffuse layer and decreases as the instability develops, and the "bubble" and "spike" structures entrain the two pure fluids. At higher volume fractions and for cases with smaller particle radius, the pre re-shock mixing

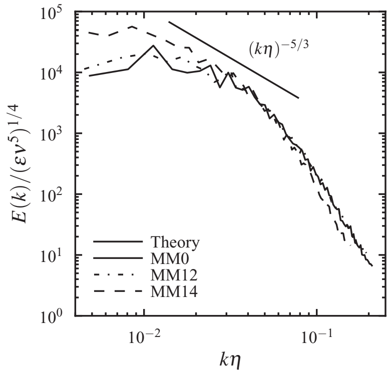

FIG. 8. Normalized spectra of the turbulent kinetic energy (TKE) for the multi-mode cases MM0, MM12, and MM14 at time $t = 8$ ms.

This article is copyrighted as indicated in the article. Reuse of AIP content is subject to the terms at: http://scitation.aip.org/termsconditions. Downloaded to IP: 143.215.48.65 On: Tue, 31 Dec 2013 19:32:03

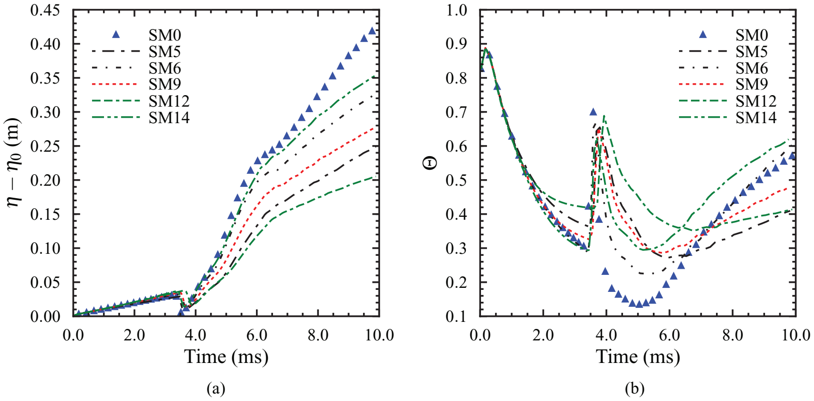

FIG. 9. Time evolution of (a) the mixing length, $\eta(t)$, and (b) the molecular mixing fraction, $\Theta(t)$ for the dilute gas-particle single-mode cases compared to the single-phase results, SM0.

layer is more well-mixed. This is a result of the increased vorticity production by the presence of the particles (see Fig. 6(b)). The re-shock then compresses the mixing layer and enhances the level of mixing such that after re-shock, the molecular mixing fraction first reaches a minimum and then increases indicating that mixing within the layer is occurring at a faster rate than the entrainment of the pure fluids. This minimum is larger for higher mass loadings. Interestingly, the initial mixing enhancement of case SM14 does not result in higher levels of mixing at late-times. Figure 10 shows contours of the species mass fraction at $Y_{\mathrm{SF}_6} = Y_{\mathrm{Air}} = 0.5$ and the particle cloud colored by the magnitude of the particle velocity for cases SM0, SM5, SM9, and SM14. There is a noticeable difference in the structure of the mixing zones between cases SM0 and SM14. For cases SM5 and SM9, which have intermediate Stokes numbers, the mixing zone is moving in the opposite direction of the particle cloud. This motion is apparent from the *x*-*t* diagram in Fig. 5(a), which shows that even for St < 1.0 the trailing edge of the particle cloud lags the mixing zone. This opposed fluid-particle motion when combined with an increase in the volume fraction from the compression of the particle cloud results in an increase in the drag on the flow and causes a reduction in the mixing length. This suggests that in certain two-phase flows the mixing efficiency of the RMI-induced mixing zone at late times can either be enhanced or inhibited with the determination largely dependent on the

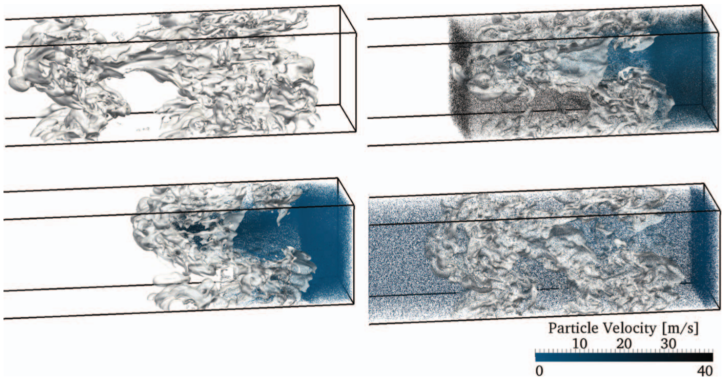

FIG. 10. Contours of the species mass fraction at $Y_{\mathrm{SF}_6} = Y_{\mathrm{Air}} = 0.5$ and particle locations colored by the magnitude of the particle velocity for cases SM0 (top left), SM5 (bottom left), SM9 (top right), and SM14 (bottom right).

This article is copyrighted as indicated in the article. Reuse of AIP content is subject to the terms at: http://scitation.aip.org/termsconditions. Downloaded to IP: 143.215.48.65 On: Tue, 31 Dec 2013 19:32:03

impulse of the re-shock event and the Stokes number. In the case of no re-shock, however, higher mass loadings seem to indicate an enhancement in the mixing.

V. CONCLUSIONS

Using detailed three-dimensional numerical simulations, RMI in dilute gas-particle mixtures is investigated both before and after re-shock for a variety of initialization conditions. Single-phase simulations of re-shocked RMI show good agreement to experimental and theoretical results giving confidence to the numerical methodology and serving as a baseline for comparison to the multi-phase results. Two parameters are used to characterize the dynamics of the two-phase RMI, the mass loading and the Stokes number, which are varied by changing the initial particle volume fraction and the particle radius for both single-mode and multi-mode initializations. At $\mathrm{St} < 1$, there is a reduction in the initial growth-rate of the RMI, but with increases in St and mass loading, there is an observable increase in the width of the mixing layer, as much as 43% in the range of conditions investigated. This increase is attributed to the additional vorticity production due to the presence of particles and inter-phase momentum coupling—a nonlinear effect not observable in the prior simplified analytical models of two-phase RMI. In addition, re-shock RMI is investigated, and it is observed that the growth-rate of the RMI after re-shock is impeded by the presence of a denser particle cloud in the case of lower Stokes number subsequently affecting the width of the mixing zone at late-times. For the multi-mode initializations, the mixing-zone saturates and closely approximates a decaying self-similar turbulent mixing layer. The particle cloud, however, only weakly affects the decay rate of the turbulent mixing layer. Most importantly, the re-shocked RMI growth rate is shown to be linearly correlated to the velocity jump at re-shock, which is reduced for smaller Stokes numbers. A new growth-rate correlation for the re-shocked RMI growth rate is introduced that is dependent on the molecular mixing fraction and the multi-phase Atwood number at re-shock resulting in a growth-rate constant of approximately 0.895. This constant, however, is a weak function of the initial volume fraction. In the future, the effect of the location particle cloud relative to the initial contact discontinuity and the re-shock distance should be investigated.

ACKNOWLEDGMENTS

This work is supported by the Defense Threat Reduction Agency (Dr. S. Peiris, Program Manager). The computational resources were provided by DoD HPC Centers at the Air Force Research Laboratory, the Engineer Research and Development Center, and the Navy DoD Supercomputing Resource Center.

[1] M. Brouillette, "The Richtmyer-Meshkov instability," Annu. Rev. Fluid Mech. **34**, 445 (2002).

[2] S. Ukai, K. Balakrishnan, and S. Menon, "Growth rate predictions of single- and multi-mode Richtmyer-Meshkov instability with reshock," Shock Waves **21**, 533 (2011).

[3] R. D. Richtmyer, "Taylor instability in shock acceleration of compressible fluids," Commun. Pure Appl. Math. **13**, 297 (1960).

[4] M. Jones and J. Jacobs, "A membraneless experiment for the study of Richtmyer-Meshkov instability of a shock-accelerated gas interface," Phys. Fluids **9**, 3078 (1997).

[5] R. L. Holmes, G. Dimonte, B. Fryxell, M. L. Gittings, J. W. Grove, M. Schneider, D. H. Sharp, A. L. Velikovich, R. P. Weaver, and Q. Zhang, "Richtmyer-Meshkov instability growth: experiment, simulation and theory," J. Fluid Mech. **389**, 55 (1999).

[6] P. R. Chapman and J. W. Jacobs, "Experiments on the three-dimensional incompressible Richtmyer-Meshkov instability," Phys. Fluids **18**, 074101 (2006).

[7] H. Hecht, U. Alon, and D. Shvarts, "Potential flow models of Rayleigh-Taylor and Richtmyer-Meshkov bubble fronts," Phys. Fluids **6**, 4019 (1994).

[8] O. Sadot, L. Erez, U. Alon, D. Oron, and L. Levin, "Study of nonlinear evolution of single-mode and two-bubble interaction under Richtmyer-Meshkov instability," Phys. Rev. Lett. **80**, 1654 (1998).

[9] Q. Zhang and S.-I. Sohn, "Nonlinear theory of unstable fluid mixing drive by shock wave," Phys. Fluids **9**, 1106 (1997).

[10] P. G. Saffman and D. I. Meiron, "Kinetic energy generated by the incompressible Richtmyer-Meshkov instability in a continuous stratified fluid," Phys. Fluids A **1**, 1767 (1989).

[11] M. Brouillette and B. Sturtevant, "Experiments on the Richtmyer-Meshkov instability: single-scale perturbations on a continuous interface," J. Fluid Mech. **263**, 271 (1994).

[12] G. Dimonte, C. E. Frerking, and M. Schneider, "Richtmyer-Meshkov instability in the turbulent regime," Phys. Rev. Lett. **74**, 4855 (1995).

This article is copyrighted as indicated in the article. Reuse of AIP content is subject to the terms at: http://scitation.aip.org/termsconditions. Downloaded to IP: 143.215.48.65 On: Tue, 31 Dec 2013 19:32:03

[13] B. Thornber, D. Drikakis, D. L. Youngs, and R. J. R. Williams, "The influence of initial conditions on turbulent mixing due to Richtmyer-Meshkov instability," J. Fluid Mech. **654**, 99 (2010).
[14] G. Dimonte and M. Schneider, "Turbulent Richtmyer-Meshkov instability experiments with strong radiatively driven shocks," Phys. Plasmas **4**, 4347 (1997).
[15] G. Dimonte and M. Schneider, "Density ratio dependence of Rayleigh-Taylor mixing for sustained and impulsive acceleration histories," Phys. Fluids **12**, 304 (2000).
[16] J. K. Prasad, A. Rasheed, S. Kumar, and B. Sturtevant, "The late-time development of the Richtmyer-Meshkov instability," Phys. Fluids **12**, 2108 (2000).
[17] D. Oron, L. Arazl, D. Kartoon, A. Rikanati, U. Alon, and D. Shvarts, "Dimensionality dependence of the Rayleigh-Taylor and Richtmyer-Meshkov instability late-time scaling laws," Phys. Plasmas **8**, 2883 (2001).
[18] O. Sadot, L. Erez, D. Oron, G. Erez, G. Ben-Dor, U. Alon, L. A. Levin, and D. Shvarts, "Studies on the nonlinear evolution of the Richtmyer-Meshkov instability," Astrophys. J., Suppl. Ser. **127**, 469 (2000).
[19] J. Ramshaw, "Simple model for linear and nonlinear mixing at unstable fluid interfaces with variable accelerations," Phys. Rev. E **58**, 5834 (1998).
[20] M. Lombardini, D. I. Pullin, and D. I. Meiron, "Transition to turbulence in shock-driven mixing: a Mach number study," J. Fluid Mech. **690**, 203 (2012).
[21] G. C. Orlicz, B. J. Balakumar, C. D. Tomkins, and K. P. Prestridge, "A Mach number study of the Richtmyer-Meshkov instability in a varicose, heavy-gas curtain," Phys. Fluids **21**, 064102 (2009).
[22] M. Lombardini, D. J. Hill, D. I. Pullin, and D. I. Meiron, "Atwood ratio dependence of Richtmyer-Meshkov flows under reshock conditions using large-eddy simulations," J. Fluid Mech. **670**, 439 (2011).
[23] B. J. Balakumar, G. C. Orlicz, J. R. Ristorcelli, S. Balasubramanian, K. P. Prestridge, and C. D. Tomkins, "Turbulent mixing in a Richtmyer-Meshkov fluid layer after reshock: velocity and density statistics," J. Fluid Mech. **696**, 67 (2012).
[24] E. Leinov, G. Malamud, Y. Elbaz, L. A. Levin, G. Ben-Dor, D. Shvarts, and O. Sadot, "Experimental and numerical investigation of the Richtmyer-Meshkov instability under re-shock conditions," J. Fluid Mech. **626**, 449 (2009).
[25] M. Vetter and B. Sturtevant, "Experiments on the Richtmyer-Meshkov instability of an air/SF_6 interface," Shock Waves **4**, 247 (1995).
[26] K. O. Mikaelian, "Turbulent mixing generated by Rayleigh-Taylor and Richtmyer-Meshkov instabilities," Physica D **36**, 343 (1989).
[27] A. A. Charakhch'yan, "Reshocking at the non-linear stage of Richtmyer-Meshkov instability," Plasma Phys. Control. Fusion **43**, 1169 (2001).
[28] R. H. Cohen, W. P. Dannevik, A. M. Dimits, D. E. Eliason, A. A. Mirin, and Y. Zhou, "Three-dimensional simulation of a Richtmyer-Meshkov instability with a two-scale initial perturbation," Phys. Fluids **14**, 3692 (2002).
[29] D. J. Hill, C. Pantano, and D. I. Pullin, "Large-eddy simulation and multiscale modelling of a Richtmyer-Meshkov instability with reshock," J. Fluid Mech. **557**, 29 (2006).
[30] O. Schilling and M. Latini, "High-order WENO simulations of three-dimensional reshocked Richtmyer-Meshkov instability to late times: dynamics, dependence of initial conditions, and comparisons to experimental data," Acta Math. Sci. **30**, 595 (2010).
[31] L. Houas and I. Chemouni, "Experimental investigation of the Richtmyer-Meshkov instability in shock tube," Phys. Fluids **8**, 614 (1996).
[32] A. A. Gowardhan and F. F. Grinstein, "Numerical simulation of Richtmyer-Meshkov instabilities in shocked gas curtains," J. Turbul. **12**, N43 (2011).
[33] B. Thornber, D. Drikakis, D. L. Youngs, and R. J. R. Williams, "Growth of a Richtmyer-Meshkov turbulent layer after reshock," Phys. Fluids **23**, 095107 (2011).
[34] K. O. Mikaelian, "Analytic approach to nonlinear Rayleigh-Taylor and Richtmyer-Meshkov instabilities," Phys. Rev. Lett. **80**, 508 (1998).
[35] K. Balakrishnan and S. Menon, "On turbulent chemical explosions into dilute aluminum particle clouds," Combust. Theory Modell. **14**, 583 (2010).
[36] P. K. Shukla, "A survey of dusty plasma physics," Phys. Plasmas **8**, 1791 (2001).
[37] S. Ukai, K. Balakrishnan, and S. Menon, "On Richtmyer-Meshkov instability in dilute gas-particle mixtures," Phys. Fluids **22**, 104103 (2010).
[38] K. Balakrishnan and S. Menon, "A multi-phase buoyancy-drag model for the study of Rayleigh-Taylor and Richtmyer-Meshkov instabilities in dusty gases," Laser Part. Beams **29**, 201 (2011).
[39] Y. Srebro, Y. Elbaz, O. Sadot, L. Arazi, and D. Shvarts, "A general buoyancy-drag model for the evolution of the Rayleigh-Taylor and Richtmyer-Meshkov instabilities," Laser Part. Beams **21**, 347 (2003).
[40] F. Genin and S. Menon, "Studies of shock/turbulence shear layer interaction using large-eddy simulation," Comput. Fluids **39**, 800 (2010).
[41] J. C. Schulz, K. C. Gottiparthi, and S. Menon, "Ionization in gaseous detonation waves," Shock Waves **22**, 579 (2012).
[42] D. M. Snider, "An incompressible three-dimensional multiphase particle-in-cell model for dense particle flows," J. Comput. Phys. **170**, 523 (2001).
[43] K. C. Gottiparthi and S. Menon, "A study of interaction of clouds of inert particles with detonation in gases," Combust. Sci. Technol. **184**, 406 (2012).
[44] S. Srinivasan, A. Smith, and S. Menon, "Accuracy, reliability and performance of spray combustion models in large-eddy simulations," in *Quality and Reliability of Large-Eddy Simulations II* (Springer, 2011), pp. 211–220.
[45] V. Boiko, V. Kiselev, S. Keselev, A. Papyrin, S. Poplavsky, and V. Fomin, "Shock wave interaction with a cloud of particles," Shock Waves **7**, 275 (1997).
[46] R. Drake, "Discussion on the paper entitled 'Forced convection heat transfer from an isothermal sphere to water' by G. C. Violet and G. Leppert," ASME J. Heat Transfer **83**, 170 (1961).

This article is copyrighted as indicated in the article. Reuse of AIP content is subject to the terms at: http://scitation.aip.org/termsconditions. Downloaded to IP: 143.215.48.65 On: Tue, 31 Dec 2013 19:32:03

On the effects of an external magnetic field on the propagation of detonations in gases

J.C. Schulz, K.C. Gottiparthi, S. Menon

School of Aerospace Engineering, Georgia Institute of Technology, Atlanta, GA, 30332, USA

Abstract

The propagation of a detonation wave in the presence of an applied magnetic field is investigated numerically in the limit of small magnetic Reynolds numbers using two-dimensional numerical simulations. Within this constraint, the governing equations for a magnetohydrodynamic (MHD) flow are solved using the quasi-static assumption, which treats the induced magnetic field as negligible in comparison to the applied field. Previous numerical studies of plasma generation in detonation waves are leveraged to estimate the electrical conductivity. These values of electrical conductivity are used under the assumption that they are constant and uniform in the post-detonation flow. A finite-rate chemical mechanism for a stoichiometric hydrogen-air mixture is employed to model the detonation physics. After the detonation propagation reaches a quasi-steady state, a magnetic field is imposed either in the direction parallel or transverse to the detonation propagation. Magnetic Reynolds number and the interaction parameter, or Stuart number are varied to characterize the stability and the propagation of the detonation. When the field is applied in the transverse direction, the energy added by the applied field results in increase in temperature by 16%. Thus, the half reaction zone distance is reduced and the transverse cell width is decreased by 50%. The transverse wave suppression along with the energy addition resulted in detonation fronts void of triple points when the magnetic field is applied in the direction parallel to the detonation front.

Keywords: gaseous detonation, stability, magnetohydrodynamics

Preprint submitted to Proceedings of the Combustion Institute *December 6, 2013*

1. Introduction

Experiments and simulations indicate that gaseous detonation waves generate a weakly ionized plasma in the post-detonation region [1, 2]. Depending on the composition of the mixture, the ionization processes can vary widely, but for stoichiometric hydrogen-air mixtures, computational simulations using detailed combustion and ionization kinetics seem to indicate that the production of NO ions is the most prominent pathway in the generation of a weakly-ionized plasma [2, 3]. Given such mixtures, the average electrical conductivity in the post-detonation is of the order of 10^{-3} S/m. Practical engineering applications involving the use of magneto-hydrodynamic (MHD) forces to manipulate the flow for generation of electrical power, propulsive thrust, etc., however, require higher levels of electrical conductivity, and thus the mixture must be seeded with particles of a low ionization potential to increase the flow's electrical conductivity [4]. Numerical studies of potassium-seeded detonations indicate that a substantial increase in the electrical conductivity is possible, but is limited since much of the available heat release from combustion is diverted to the ionization process rather than to sustaining the detonation wave [2]. Given these prior studies, a range of electrical conductivities can be identified as feasible in practical engineering applications involving gaseous detonations. The physics of how an electromagnetic field interacts with the conducting products of a detonation and how that interaction might affect the stability and the propagation of the detonation wave is now systematically addressed.

A distinctive feature of MHD flows is the generation of induced currents resulting from the relative motion of a conductive fluid in an external magnetic field not aligned with the flow velocity. These currents introduce an additional mechanism for the dissipation of energy within the flow, which is characterized by the magnetic diffusivity, $\eta = 1/\mu\sigma$, where μ is the permeability of free space, and σ is the electrical conductivity. Most importantly, however, is the ratio of the time scale of magnetic diffusion ($\tau_\eta = \eta^2/L$) to the flow time scale ($\tau_u = u/L$), where u and L are the characteristic velocity and length scales. This ratio is defined as the magnetic Reynolds number, $Re_m = \tau_\eta/\tau_u = u/L = \mu\sigma uL$. For a typical ionizing hydrogen-air detonation, Re_m is estimated to be of the order of 10^{-3}. For MHD flows, when $Re_m << 1$, the induced magnetic fields diffuse quickly and can be neglected relative to the imposed magnetic field, B_0. The induced currents, however, play a dominant role in the conversion of the Lorentz force into heat via the process of ohmic dissipation, which occurs at a time-scale of τ_η. This process is highly anisotropic. Fluids motions misaligned with the magnetic field are preferentially dissipated at a rate which is proportional to $\cos\theta^2$ where θ is the angle between B_0 and the wavenumber vector k. As a result, an elongation of vortical structures along the direction of B_0 is observed. These effects are counteracted, however, by the natural development of the non-linear flow. The magnetic interaction parameter or Stuart number, N, is a measure of the balance of the inertial and Lorentz forces and is given by $N = \sigma B_0^2 L/\rho u$, where ρ is the density of the gas. For example, in the simplistic scenario of a decaying isotropic turbulent flow, vortex flux tubes, aligned in direction of the magnetic field, begin to form with the complete transition to a two-dimensional turbulent state independent of B_0 at very large N [5]. For detonations, the dynamics of the flow are complicated by the persistent energy release and generation of large-scale fluid structures at the detonation front. The effect of the magnetic field on these structures is investigated here.

To investigate the effect of a magnetic field on the propagation of a detonation, numerical simulations are conducted for various magnetic Reynolds numbers and interaction parameters under the assumption of $Re_m << 1$. The external field is applied in either perpendicular or parallel to the direction of the propagation of the detonation. This study relies on previous numerical simulations [2] of stoichiometric hydrogen-air detonations for estimates of the electrical conductivity in the post-detonation flow. As such, only a finite-rate kinetic mechanism for the combustion process is included in the numerical simulation, and the electrical conductivity is assumed to be spatially uniform and constant in the post-detonation region. Flow parameters, along with the reaction zone widths, are analyzed to quantify the effect of the applied field on the detonation.

The structure of this paper is as follows. First, a brief discussion of the numerical formulation and simulation setup is given. Second, the simulation of a gaseous detonation without a magnetic field is presented. This is followed by a discussion of the effects on the detonation from to the inclusion of an external magnetic field. In particular, the role of the direction of the applied field on the detonation structure is addressed. Lastly, conclusions from the studies performed are summarized and proposals for future work are suggested.

2. Numerical Formulation

The governing equations for a reacting, MHD flow are obtained through the addition of source terms to the momentum and energy conservation equations, i.e., the Lorentz force ($\epsilon_{ijk} J_j B_{0,k}$) and an electrical power dissipation term ($J_i E_i$), where J_i is the current density vector, $B_{0,k}$ is the applied field, and E_i is the electric field vector [5]. The set of governing equations is:

$$\frac{\partial \rho}{\partial t} + \frac{\partial \rho u_i}{\partial x_i} = 0 \tag{1}$$

$$\frac{\partial \rho u_i}{\partial t} + \frac{\partial}{\partial x_j}\left(\rho u_i u_j + p\delta_{ij}\right) = \epsilon_{ijk} J_j B_{0,k} \tag{2}$$

$$\frac{\partial \rho \mathcal{E}}{\partial t} + \frac{\partial}{\partial x_i}\left[\,(\rho \mathcal{E} + p)\, u_i\right] = J_i E_i \tag{3}$$

$$\frac{\partial \rho Y_k}{\partial t} + \frac{\partial}{\partial x_i}\left[\rho Y_k u_i\right] = 0 \tag{4}$$

In the above equations, ρ is the gas density, u_i is the velocity vector, and Y_k is the kth species mass fractions, and $\mathcal{E}$ is the total specify energy, which is equal to the sum of the internal energy, e, the specific kinetic energy, $u_i u_i/2$, and the magnetic energy density, $B_i B_i/2\rho\mu_0$. The thermodynamic pressure, p, is computed using the perfect gas equation of state, $p = \rho RT$, where T is the temperature of the gas phase, and R is the mixture-averaged gas constant. A combustion model developed by Petersen and Hanson [6] is used to simulate detonation in H_2/O_2-N_2 mixtures. The full hydrogen-oxygen chemistry is reduced to 18 elementary reactions and 8 primary species (H_2, O_2, OH, H, O, H_2O, HO_2, H_2O_2) and an inert species such as N_2 or Ar. This mechanism predicts global detonation parameters accurately over a wide range of N_2 concentrations (see Fig. 1) and is frequently used in detonation simulations [7]. In particular, this mechanism has been used in previous numerical studies of ionizing detonations in a potassium-seeded hydrogen-air mixture where the mechanism was coupled with a 47-step, 17 species ionization chemistry [2].

The above equations are supplemented with an additional equation governing the evolution of the induced electromagnetic field. In the quasi-static assumption, this reduces to a single equation for the current density, $J_i = \sigma \epsilon_{ijk} u_j B_{0,k}$. Lastly, following Ohm's law, the current density is assumed to be linearly related to the electric field, E_i, through the scalar σ. In the current work, σ is assumed to be constant; however, it is important to mention that σ is typically a strong function of both temperature and the gas-composition.

The governing equations are solved numerically using a second-order predictor-corrector finite-volume scheme where the cell-surface fluxes are computed using a using a hybrid Harten-Lax-Van Leer approximate Riemann solver (HLLC/E) with a Monotone Upstream-Center Schemes for Conservation Laws (MUSCL) reconstruction. The HLLE flux solver is used in the directions transverse to the high pressure gradients while the HLLC flux solver is used elsewhere [8]. Lastly, the chemical source terms, $\dot{\omega}_k$, in Eq. 4 are obtained through time-accurate integration. This numerical approach has been used to study a variety of related applications, such as plasma-generation by gaseous detonation [2], compressible decaying MHD turbulence with large-eddy simulation [5], and plasma-assisted combustion by arc-discharge [3, 9].

Table 1: A summary of parameter set for the simulations used in this study. To compute the non-dimensional parameters the following reference values were used: L=6 mm, u = 1900 m/s, ρ_0=0.17 kg/m^3 where L is the transverse channel dimension, $u \approx D$, and ρ is the ambient density. The MHD cases are distinguished by a X indicating the magnetic field is in the direction of the detonation propagation (x-direction), and a Y indicating the magnetic field is perpendicular to the direction of the detonation propagation (y-direction). These cases are compared against the hydrodynamic simulations of case NF (No-Field).

Case	σ (S/m)	Re_m	N
NF	0.0	0.0	0.0
X1,Y1	0.001	1.43×10^{-8}	0.0186
X2	0.01	1.43×10^{-7}	0.186
X3	0.001	1.43×10^{-8}	1.86
X4,Y4	0.01	1.43×10^{-7}	18.6
X5	0.01	1.43×10^{-7}	74.3
X6	0.01	1.43×10^{-7}	186.0
X7	0.01	1.43×10^{-7}	464.0
X8	0.01	1.43×10^{-7}	1860.0

3. Simulation Setup

To initialize the detonation simulation, a direct initiation is first numerically modeled to obtain the correct detonation profiles with an overdrive factor close to unity. The overdrive factor, f, is defined as $(D/D_{CJ})^2$ where D is the velocity of the detonation wave and D_{CJ} is the Chapman-Jouget or CJ detonation speed. This detonation profile, shown in Fig. 2, is then used to initialize the two-dimensional simulations, which are performed in the frame of reference of the moving detonation. The boundary conditions in the direction of the detonation propagation are modeled as non-reflecting supersonic inflow and outflow boundaries. In the transverse directions, the boundaries are set to be periodic [10]. Although, the current formulation has been validated for a wide range of ambient pressures and diluent concentrations [2], for all cases here, the ambient pressure and temperature are 0.2 bar and 298 K, respectively.

Numerical simulations are conducted for different Re_m, N, and magnetic field orientations i.e., parallel ($B_{0,x}$) and transverse ($B_{0,y}$) to the detonation propagation. Table 1 summarizes the parameters studied in this work. Since $Re_m << 1$, the non-dimensional parameter Re_m, however, is of less importance, and N and the magnetic field orientation govern the dynamics of the detonation. The value of Re_m is recorded to ensure the validity of the quasi-static assumption. At $t_0 = 0.113$ ms of case NF (no-field), the magnetic field is switched on. The magnetic field is always taken as positive, since in two dimensions, the components of the Lorentz force do not change (only the orientation of the current density changes), and thus the detonation dynamics are unchanged.

The computational domain is discretized using an uniform resolution (Δx). The value of Δx is chosen in order to spatially resolve the half-reaction length ($L_{1/2}$) and the evolution of species mass fractions [10]. For the ambient conditions and the gaseous mixture considered here, $\Delta x = 10\ \mu$m is sufficient to resolve the detonation front (see Fig. 3) i.e. the interaction between the Mach stem (M), incident shock (I), and transverse wave (T). Also, as shown in Fig. 2, fully resolved species profiles are obtained. At this resolution, the grid resolution provides 80 points per theoretical $L_{1/2}$. Thus, for the current investigations, $\Delta x = 10\ \mu$m is considered adequate. Further details of resolution studies and quantification of numerical accuracy for detonation in H_2-O_2-N_2 mixtures using the formulation presented here is found elsewhere [2].

4. Results

A detonation propagating in a reactive gaseous mixture can be described as a shock wave sustained by the energy release from the shock-induced reaction. Thus, any mechanism affecting the shock strength and altering either the post-shock conditions and/or the chemical reaction rates can affect the propagation and stability characteristics of the detonation. For example, the inclusion of chemically inert particles in a gas mixture can been used to control the detonation propagation, and in some situations, such methods can be used to achieve detonation quenching [10]. Another possible method for detonation control could be achieved by application of an external magnetic field. This interaction is discussed in the following sections. Results are compared to simulations of no applied magnetic field, and for all cases simulated here, the transformed MHD detonation returns to the hydrodynamic detonation structure, i.e., detonation velocity, cell-width, etc., after some time of the field being switched off.

4.1. *Effect of $B_{y,0}$*

When the magnetic field is applied, the electromagnetic energy generated by action of the Lorentz force in the post-detonation flow is quickly converted into heat via joule dissipation. In particular, since the induced currents are largest at the detonation front, a significant amount of electromagnetic energy is deposited directly in the induction zone of the detonation. For case Y4, the post-detonation temperature increases by nearly 450 K after the magnetic field is turned on. Moreover, the Joule dissipation does not decrease in time as in decaying problems due to the continual formation of new scales from combustion at the detonation front. As the temperature gradually increases, see Fig. 4, the reaction zone length reduces, and the distance to the peak HO_2 mass fraction reduces to 0.2 mm from 0.7 mm as in the case NF (see Fig. 5). A characteristic of propagating detonations is the formation of cellular structures whose cell widths in transverse direction are dependent on $L_{1/2}$ [11]. These stuctures create characteristic large-scale structures in the post-detonation flow. In case Y4, smaller cellular structures are formed in comparison to NF. Interestingly, the cell width is reduced to nearly 3 mm at $t = 0.15$ ms as shown in Fig. 6. At lower N, such as in case Y1, this does not occur. Although joule dissipation continues to occur, the detonation front adjusts to a steady value as the kinetics become rate-limited by radical production. Thus, at $t = 0.16$ ms the cell width remains at approximately 3 mm. Since the magnetic field modifies the observed detonation cell-width, and this change is related through N, estimatation of the electrical conductivity of the gaseous mixture is possible from observations of the cellular structure in a give magnetic field.

The heat addition by the magnetic field also affects the detonation velocity. Since the Joule dissipation is proportional to B_0^2, and thus N, the effect of heating on detonation is more profound in case Y4 than in case Y1. Thus, the deviation in the detonation velocity (see Fig. 7) increases with N. Even in case Y1, the detonation velocity is marginally augmented in comparision to case NF. Note that,for both case Y1 and Y4, the Lorentz force is in the direction opposite of the detonation propagation. The momentum deficit, however, is negligible in comparison to the subsequent expansion occurring from heat addition. This is due to the application of the field in the direction perpendicular to the direction of the dominant velocity component (in x-direction).

4.2. *Effect of $B_{x,0}$*

When the magnetic field is applied in the x-direction, the detonation velocity increases slightly, but this increase is independent of N as shown in Fig. 7. The current density, and likewise the electromotive force, is proportional to the component of the velocity perpendicular to the magnetic field, in this case, the transverse velocity. Similar to case Y1 and Y4, Joule dissipation results in reduction of $L_{1/2}$ at lower N as shown in Fig. 8. For simulations with an applied $B_{x,0}$, however, the Lorentz force counters the movement of transverse waves in the post-detonation flow since their motion is perpendicular to $B_{x,0}$. This introduces new dynamics. At higher values of N, the transverse waves are actively suppressed. This suppresion reduces the strength of the transverse wave interaction with the Mach stem and incident shock at the detonation front, and over time the front becomes relatively flat. The formation of the characteristic cellular structures are thus eliminated (see Fig. 9). This results in a reduction in the $L_{1/2}$ in the cases Y4-Y8. The combined effect of heat addition via Joule dissipation and transverse wave suppression, which disables the high temperature triple point formation [10], results in only a marginal increase in the detonation velocity for any given N. For the times simulated here, and for the values of N investigated, the reaction front does not decouple from the shock wave. This was determined by switching off the magnetic field after some time. For any given N, the typical cellular structures are regenerated by turning off the applied field.

To summarize, the magnetic field applied in the direction of detonation propagation affects the detonation through a combined effect of Joule heating and Lorentz force. While the Lorentz force acts to eliminate transverse waves and cellular structure, the heating effect resulted in temperature increase and sustained coupling of reaction zone with the shock propagation. Thus, for any given N, the change in detonation velocity is marginal. Due to the difference in the magnitude of velocity components in x- and y -directions, $B_{0,x}$ affected the detonation both by momentum and energy coupling where as the dominant effect of $B_{0,y}$ is Joule dissipation.

5. Conclusions

Using numerical simulations, the propagation of a detonation wave in the presence of an applied magnetic field is investigated. From experimental measurements and previous numerical studies of ionizing detonations using detailed kinetics, a range of electrical conductivities are estimated and used in this study. These measurements indicate that the magnetic Reynolds number of a typical gaseous detonation are much less than one. Leveraging this knowledge, simulations are performed using the quasi-static assumption. In the limit of small magnetic Reynolds number, the interaction parameter becomes the governing non-dimensional number. In this study, the interaction parameter is varied as well as the magnetic field orientation in order to investigate how the field may affect the propagation and stability of the detonation. For transverse fields of large N, the cellular sturcture of the detonation is affected resulting in cell-widths half the size of those observed in detonations with no applied magnetic field. The reduction in the half-reaction distance consequently results in an increase in the detonation velocity. For magnetic fields in the direction of the detonation propagation, an increase in detonation velocity is also observed, but at high N, the transverse waves are adversely affected. The supression of the transverse waves results in the elimination of the detonation structure. Turning off the magnetic field results in the regeneration of cellular structures.

Acknowledgments

This work is supported by the Defense Threat Reduction Agency (Program Managers: Dr. S. Peiris and Dr. C. Shipbaugh). The computational resources are provided by DoD HPC Centers at the U.S. Air Force Research Laboratory DoD Supercomputing Resource Center and Engineer Research and Development Center.

References

[1] S. Basu, Phys. Fluids 3 (3) (1960) 456–463.
[2] J. Schulz, K. Gottiparthi, S. Menon, Shock Waves 22 (6) (2012) 579–590.
[3] K. Miki, J. Schulz, S. Menon, Proc. Combust. Inst. 32 (2008) 2413–2420.
[4] F. Lu, H.-C. Liu, D. Wilson, Meas. Sci. Tech. 16 (2005) 1730–1740.
[5] K. Miki, S. Menon, Phys. Plasmas 15 (2008) 072306.
[6] E. L. Petersen, R. K. Hanson, J. Propul. Power 15 (4) (1999) 591–600.
[7] N. Tsuboi, Y. Morii, A. K. Hayashi, Proc. Combust. Inst. 34 (2013) 1999–2007.
[8] F. Génin, S. Menon, Comp. Fluids 39 (2010) 800–819.
[9] K. Miki, J. Schulz, S. Menon, Plasma Chem. Plasma Process. 33 (2013) 959–978.
[10] K. C. Gottiparthi, S. Menon, Combust. Sci. Technol. 184 (3) (2012) 406–433.
[11] J. E. Shepherd, Proc. Combust. Inst. 32 (2009) 83–98.

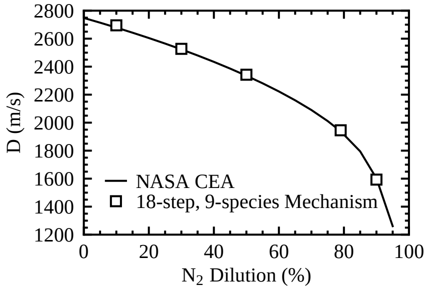

Figure 1: Comparison of the numerically computed detonation velocity for a H_2-air mixture at an ambient pressure and temperature of 0.2 bar and 298 K, respectively. The results are compared to theoretical computations of the detonation velocity obtained from NASA's CEA code.

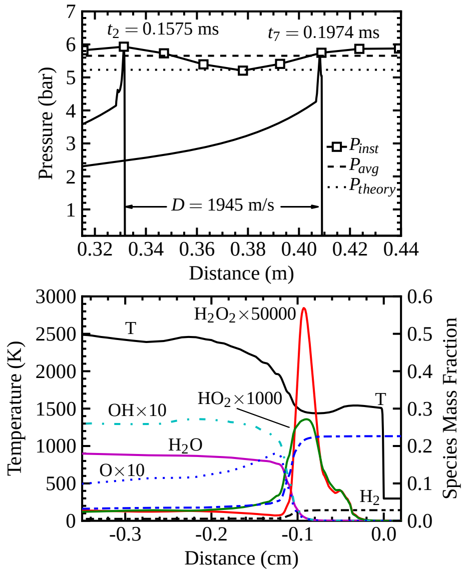

Figure 2: One-dimensional profiles of pressure shown at two instances in time as the detonation propagates through the domain. The average peak pressure is close to the theoretical value for a stoichiometric H_2-air detonation in an ambient pressure and temperature of 0.2 bar and 298 K. Profiles of temperature and mass fraction of species are also shown.

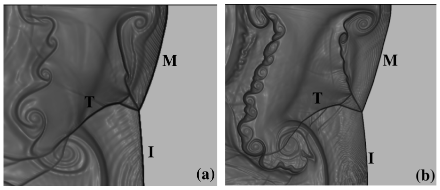

Figure 3: Plot of $\ln(|\nabla\rho| + 1)$ showing the Mach stem (M), the Incident shock (I) and the Transverse wave (T) at the detonation front for (a) $\Delta x = 10\ \mu$m and (b) $\Delta x = 5\ \mu$m.

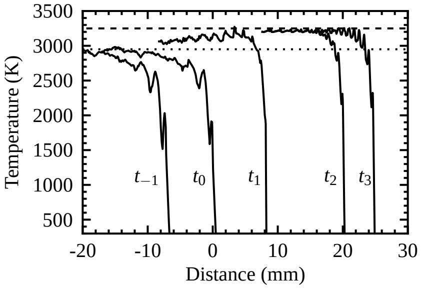

Figure 4: The averaged temperature profiles for case Y4 at different times: t_{-1} = 0.104 ms, t_0 = 0.113 ms, t_1 = 0.127 ms, t_2 = 0.149 ms and t_3 = 0.157 ms.

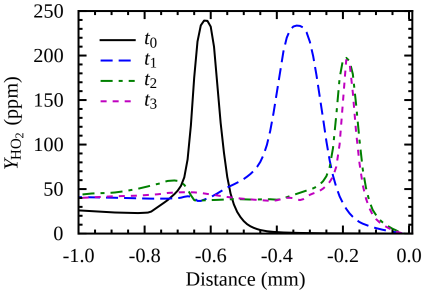

Figure 5: The profiles of mass fraction of HO_2 taken at the transverse location corresponding to the center of Mach stem for case Y4 at different times: t_0 = 0.113 ms, t_1 = 0.127 ms, t_2 = 0.149 ms and t_3 = 0.157 ms.

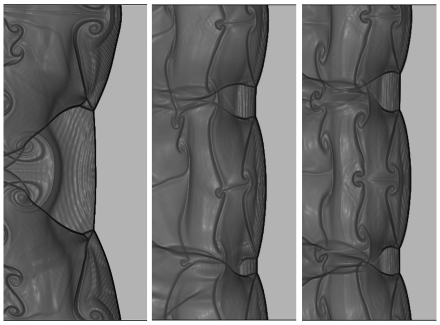

Figure 6: Plot of $\ln(|\nabla\rho| + 1)$ for case Y4 showing the structure of the detonation front at t_0 = 0.113 ms, t_2 = 0.149 ms and t_3 = 0.157 ms.

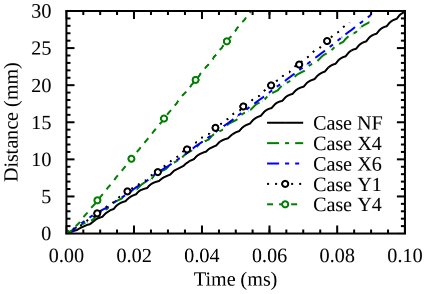

Figure 7: The average location of the detonation front as a function of time for the cases given in Table 1

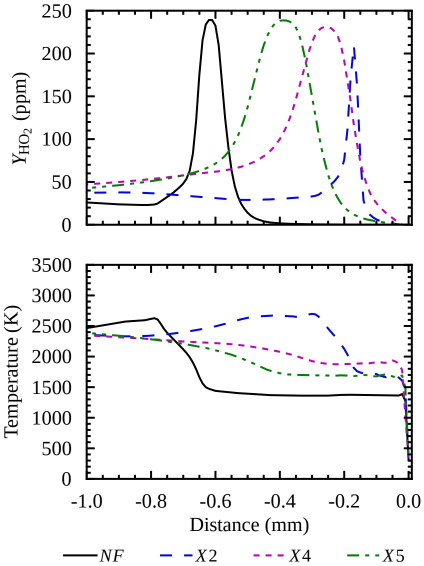

Figure 8: Profiles of the HO_2 mass fraction and temperature for cases NF, X2, X4, and X5 corresponding to the center of the Mach stem for each detonation front at approximately 0.175 ms.

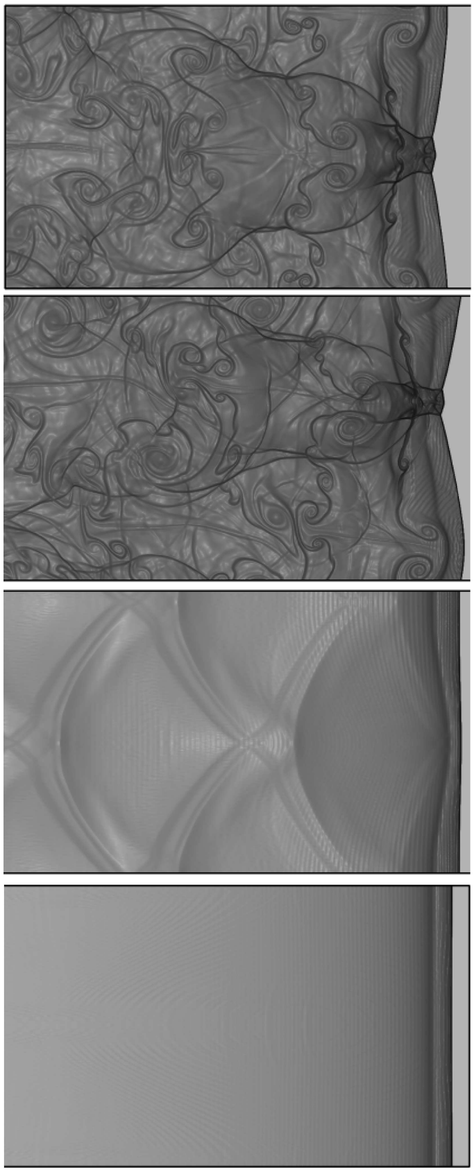

Figure 9: Plot of $\ln(|\nabla\rho| + 1)$ for cases NF, X2, X4, and X5 (top to bottom) shown in Table 1 showing the detonation front and the post-detonation flow structures at t = 0.175 ms.